1-1-2007

Mixing time in yield stress fluids

Ihuaku Ihejirika
Ryerson University

MIXING TIME IN YIELD STRESS FLUIDS

by

Ihuaku Ihejirika

Bachelor of Applied Science, Chemical Engineering, University of Toronto, 2004

A thesis presented to Ryerson University

in partial fulfillment of the

requirements for the degree of

Master of Applied Science

in the Program of

Chemical Engineering

Toronto, Ontario, Canada, 2007

Declaration

I hereby declare that I am the sole author of this thesis.

I authorize Ryerson University to lend this thesis to other institutions or individuals for the purpose of scholarly research.

* Signature

I further authorize Ryerson University to reproduce this thesis by photocopying or by other means, in total or in part, at the request of other institutions or individuals for the purpose of scholarly research.

* Signature

Acknowledgments

I wish to acknowledge the support provided by my supervisor, Dr. Farhad Ein-Mozaffari, in completing this thesis. Special thanks also go to Mr. Ali Hemmati and Mr. Peter Scharping who were always willing to assist me with equipment setup, troubleshooting and repair.

The financial support of the National Science and Engineering Research Council of Canada (NSERC) is gratefully acknowledged.

The love and support of my parents is deeply appreciated. Finally, I am immensely grateful to God for the strength He provided me in completing this work.

Mixing Time in Yield Stress Fluids
Ihuaku Ihejirika
Master of Applied Science, 2007
Department of Chemical Engineering
Ryerson University

Abstract

Yield stress fluids are commonly encountered in the pharmaceutical, wastewater and bioprocess industries. On agitation of these fluids with an impeller, a zone of significant motion (cavern) is formed surrounded by stagnant regions. These inhomogeneous conditions are undesirable from a product quality standpoint.

Therefore, to evolve a mixing system design that would eliminate these problems, experimental measurements of mixing time were obtained and combined with power consumption to provide a measure of mixing system efficiency. The effect of different parameters such as fluid rheology, impeller rotational speed, impeller type and impeller clearance on the mixing times was also investigated. In addition, using CFD, numerical mixing times were calculated and a comparison of the numerical and experimental mixing times were conducted to investigate the capability of the CFD tool to correctly predict the homogenization process in mixing tanks.

In general, it was observed that the power characteristics of the different agitators were well reproduced by the computational package. In addition, CFD was able to correctly predict the effect of impeller rotational speed and fluid yield stress on the mixing times. However, the effect of impeller clearance on the mixing time was not correctly predicted by the CFD package when compared with experimental results obtained in this work as

well as those obtained by other researchers. A comparison of the impellers used in this study (Pitched Blade Turbine (PBT), marine propeller and Lightnin A320) using the mixing time correlations available in the literature to fit the experimental data revealed that the PBT was superior to the other impellers in mixing yield stress fluids. In addition, the validated CFD model was used to measure the dimensions of the cavern formed around the impeller and it showed good agreement with the Elson's cavern model.

TABLE OF CONTENTS

List of Tables

List of Figures

1. Introduction

Mixing is a major component of operations in the chemical and process industries, and when Newtonian fluids are encountered, it is a fairly easy operation. However, the same cannot be said for highly viscous non-Newtonian fluids, particularly those exhibiting a yield stress. Yield stress fluids contain structured networks of molecules that depend on the shear rate of the fluid. Such fluids exhibit a high apparent viscosity at low shear rates, and since the shear rate decreases as the distance from the impeller increases, circulation problems can often be encountered when mixing such fluids (Hayes *et al.*, 1998). Close to the impeller, there is formation of a zone of significant motion called a cavern. Examples of materials exhibiting yield stress include particulate suspensions, emulsions, some foodstuffs, blood, paint, pastes and cosmetics (Curran *et al.*, 2000; Chhabra and Richardson, 1999; Zhu *et al.*, 2005).

Several approaches have been considered to improve the mixing of yield stress fluids. For instance, in the mixing of xanthan gum, a highly shear thinning fluid possessing a yield stress, a replacement of the "standard" Rushton turbine with other impeller geometries which might be expected to perform better (such as the Lightnin A315 impeller) has been proposed (Galindo and Nienow, 1992).

Mixing systems can be characterized in terms of a performance criterion called the mixing time. The mixing time is a key process parameter in many dispersion and homogenization applications in stirred tanks widely used to describe the quality and effectiveness of mixing of fluids in stirred tanks (Carreau *et al.*, 1976). Mixing time provides a measure of homogeneity of the mixing system (Hayes *et al.*, 2000) and is mainly useful for comparing different agitator systems; for the same power input, the most efficient mixer is the one with the shortest mixing time (Houcine *et al.*, 2000; Chavan *et al.*, 1975). However, for highly viscous fluids, both Newtonian and non-

Newtonian, determination of an absolute mixing time is a difficult task because of the difficulty in attaining a truly homogeneous mixture (Carreau *et al.*, 1976). Since collecting data under experimental conditions can be time consuming and expensive, computational fluid dynamics (CFD) is an option. CFD provides an efficient means to predict the mixing time in stirred tanks. If properly and correctly applied, CFD can provide a more rapid design of mixing tanks because it allows for the rapid evaluation of several different design scenarios compared to constructing experiments for each scenario under consideration. However, experiments are still needed to validate the mixing time results obtained from CFD (Hayes *et al.*, 1998; Harvey and Cassian, 1995).

Few publications have been devoted to the CFD modeling of the mixing of non Newtonian fluids (de la Villeon *et al.*, 1998; Shekhar and Jayanti, 2003; Bertrand *et al.*, 1996; Xu and McGrath, 1996). In some of cases, the mixing times have also been simulated in an attempt to predict the mixing performance of different impellers (Montante *et al.*, 2005; Thyn *et al.*, 2005). However, a thorough search of the current mixing literature suggests that CFD modeling of non Newtonian fluids is limited.

Therefore, the objectives of this work are to use CFD to characterize the performance of three axial flow impellers: the marine propeller, A320 impeller and pitched blade turbine (PBT) impeller in the mixing of a yield stress fluid, xanthan gum. This characterization will be done in terms of power consumption and mixing time. In addition, the effect of impeller rotational speed, fluid rheology, impeller type and impeller location from the tank bottom (clearance) on the observed mixing times will be investigated. An investigation into the size of the cavern generated by the marine propeller and the pitched blade turbine as a function of impeller

rotational speed will be conducted using the CFD tool from which conclusions on the mixing performance of these impellers in mixing yield stress fluids will be drawn.

2. Literature Review

Introduction

The proper design of mixing systems for non Newtonian fluids requires an understanding of the rheology of these fluids as this information has implications on the impeller geometry and system configuration that would be required to achieve the desired mixing performance. Therefore, the literature review section begins with an overview of non Newtonian fluids and the mathematical expressions that describe their behavior. Thereafter, an introduction to the impeller classification adopted in this work is presented. A review of two important parameters for describing mixing system performance namely power consumption and mixing time is also undertaken, and then a summary of the important research involving non-Newtonian fluids in stirred tanks is conducted, after which the concept of cavern formation is presented especially with regards to the important information it provides on the extent of mixing in the mixing tank.

2.1 *Mixing Theory*

2.1.1 Rheology of Non-Newtonian Fluids

A non-Newtonian fluid may be defined as a fluid whose flow curve (plot of shear stress versus shear rate) is non-linear. In other words, its apparent viscosity is not constant at a given temperature and pressure, but depends on flow conditions such as flow geometry, shear rate, etc. (Chhabra and Richardson, 1999).

Non-Newtonian fluids may be broadly classified into two categories:

Time-independent fluids: Shear stress is a unique function of the shear rate and is independent of the time of shearing. The apparent viscosity, μ_a, at a particular shear rate for time independent non-Newtonian fluid behavior is defined as (Holland and Chapman, 1966):

$$\mu_a = \frac{\tau}{\dot{\gamma}} \tag{2.1}$$

where τ and $\dot{\gamma}$ are the shear stress and shear rate respectively.

Time-dependent fluids: The relationship between shear stress and shear rate depends on the duration of shearing.

Since the focus of this study is on the mixing of xanthan gum, a pseudoplastic fluid possessing a yield stress, which falls under the category of time-independent fluids, the following paragraphs will address this class of fluids

Time independent non-Newtonian behavior may be further broken down into three types:

i) Shear thinning or pseudoplastic

ii.) Shear thickening or dilatant

iii.) Viscoplastic

Shear thinning or pseudoplastic: This is the most common type of time-dependent non-newtonian fluid behavior observed, and a fluid with this property has an apparent viscosity that decreases with increasing shear rate. The flow curves (shear stress vs. shear rate) of most shear thinning polymer solutions and melts become straight lines at very high and very low shear rates

which indicates newtonian behavior at these shear rate values. The apparent viscosity at the very high and very low shear rates is referred to as the zero shear viscosity (μ_0) and the infinite shear viscosity (μ_∞) respectively. Therefore, the apparent viscosity decreases from μ_0 to μ_∞ with increasing shear rate.

The values of the shear rates that give rise to the upper and lower limiting viscosities are dependent on a number of factors, such as the type and concentration of the polymer, polymer molecular weight distribution, nature of the solvent, etc.

Shear-thickening or dilatant: Dilatant fluids are characterized by an apparent viscosity that increases with increasing shear rate; hence they are also referred to as shear thickening fluids. Originally observed in some concentrated suspensions such as china clay and titanium dioxide, dilatant fluid behavior has not been studied in great detail.

Viscoplastic: This fluid behavior is characterized by the existence of a yield stress which must be exceeded before the fluid can flow. Once the magnitude of the external stress exceeds the yield stress, the flow curve may be linear or non-linear. The viscoplastic fluid behavior can be explained by postulating that the fluid at rest is made up of three-dimensional structures of sufficient rigidity to resist any stress less than the yield stress.

If the flow curve is linear for $\tau > \tau_y$, the fluid is a Bingham plastic fluid and is characterized by a constant plastic viscosity (slope of the linear flow curve) and a yield stress. A fluid possessing a non-linear flow curve (for $\tau > \tau_y$) beyond the yield stress value is called a 'yield-

pseudoplatic' material (Chhabra and Richardson, 1999). A viscoplastic material also possesses an apparent viscosity that decreases with increasing shear rate (Chhabra and Richardson, 1999).

As mentioned previously, since this focus of this study is on the mixing of pseudoplastic yield stress fluids, the mathematical models that describe the behavior of such fluids will be discussed.

Mathematical Models for time-independent fluid behavior

The power law or Ostwald de Waele model

A plot of shear stress vs. shear rate on log-log coordinates can be approximated to a straight line over a limited range of shear rates (or shear stress) (Chhabra and Richardson, 1999; Harnby *et al.*, 1997). This portion of the flow curve has the following equation:

$$\tau = K\left(\dot{\gamma}\right)^{n} \tag{2.2}$$

the apparent viscosity of a power law fluid is thus given by:

$$\mu_a = \frac{\tau}{\dot{\gamma}} = K\left(\dot{\gamma}\right)^{n-1} \tag{2.3}$$

where K and n are empirical curve-fitting parameters known as fluid consistency index and flow behavior index respectively (Chhabra and Richardson, 1999).

When $n < 1$, the fluid is pseudoplastic; when n = 1, the fluid is Newtonian and K becomes equal to μ , and when $n > 1$, the fluid exhibits shear thickening properties.

The power law model represents the most widely used model (Chhabra and Richardson, 1999; Harnby *et al.*, 1997).

The Ellis model

The apparent viscosity of shear thinning fluids can be modeled more appropriately at low shear rates where deviations from the power law model are significant using the Ellis model (Chhabra and Richardson, 1999) which has the following form:

$$\mu = \frac{\mu_0}{1 + \left(\tau / \tau_{1/2} \right)^{\alpha - 1}} \tag{2.4}$$

μ_0 is the zero shear viscosity, $\tau_{1/2}$ and α are model parameters with α representing the degree of shear thinning behavior, and $\tau_{1/2}$ representing the value of the shear stress at which the apparent viscosity has dropped to half of its zero shear value (Chhabra and Richardson, 1999)

The *Carreau viscosity model* is a viscosity model that takes into account the limiting viscosities, μ_0 and μ_∞ at very high and very low shear rates where there are significant deviations to the power law model:

$$\frac{\mu - \mu_\infty}{\mu_0 - \mu_\infty} = \left[1 + \left(\lambda \dot{\gamma} \right)^2 \right]^{(n-1)/2} \tag{2.5}$$

The Bingham plastic model

This is the simplest model describing the behavior of a fluid with a yield stress.

$$\tau = \tau_y + m\gamma \qquad \text{for } \tau > \tau_y \qquad (2.6)$$

$$\gamma = 0 \qquad \text{for } \tau < \tau_y$$

The Herschel Bulkley model

This model is used to describe the rheology of viscoplastic fluids with non-linear flow curves:

$$\tau = \tau_y + m\left(\dot{\gamma}\right)^n \qquad \text{for } \tau > \tau_y \qquad (2.7)$$

$$\gamma = 0 \qquad \text{for } \tau < \tau_y$$

Based on the previous discussion, the shear thinning, pseudoplastic fluid used in this work will be modeled using the Herschel Bulkley model.

2.1.2 Impeller Types

Impellers are classified into two general types based on the flow patterns that they produce in the mixing vessel: axial flow impellers and radial flow impellers (Paul *et al.*, 2004). An axial flow impeller discharges fluid along the impeller axis (parallel to the impeller shaft) while the radial flow impeller discharges fluid along the impeller radius (perpendicular to the vessel wall) and produce two circulating loops; one above and one below the impeller with mixing occurring between the two loops but not as much as within a single loop (Ranade *et al.*, 1992; Oldshue, 1983; Holland and Chapman, 1966).

Axial flow impellers (pitched blade turbine, propeller, hydrofoils) are suited for liquid blending and solids suspension, while radial flow impellers (rushton turbine, flat blade turbine, hollow blade turbine) are best for gas dispersion applications (Paul *et al.*, 2004).

2.1.3 Power Draw

Power draw or power consumption is defined as the energy transferred from the impeller to the fluid per unit time (Harnby *et al.*, 1997), and is usually a function of the flow regime, tank and impeller geometry and fluid rheology. It provides a measure of the power required for the operation of an impeller.

For Newtonian fluids, a fixed tank and impeller geometry, and a flat fluid surface with no vortices, the power draw is only a function of the Reynolds number (Curran *et al.*, 2000):

$$\frac{P}{d^5 N^3 \rho} = N_p = f\left(\frac{Nd^2\rho}{\mu}\right) \Rightarrow N_p = f(R_e) \tag{2.8}$$

P is the power consumption calculated from the torque produced by a rotating agitator and is given by:

$$P = 2\pi NM \tag{2.9}$$

where M and N are the torque and impeller rotational speed, respectively.

In the laminar flow regime, the power number is inversely proportional to the Reynolds number:

$$N_p = K_p / R_e \tag{2.10}$$

Where N_p is the power number, Re is the Reynolds number and K_p is a geometric factor related to power consumption for a mixing system (Delaplace *et al.*, 2000b). The log-log plot of N_p vs. Re represents the power curve for the mixing system. In the laminar regime ($Re < 10$), the slope of the power curve is -1 as may be deduced from Equation (2.10).

A power curve provides power data for a particular tank configuration at various impeller speeds, liquid viscosities and densities.

As mentioned previously, the viscosity of non-Newtonian fluids (and the Reynolds number) depends on the shear rate, which in turn depends on the impeller rotational speed.

Therefore, to generate a power curve for non-Newtonian fluids similar to that for Newtonian fluids, the Reynolds number must be defined in terms of an effective or apparent viscosity, μ_a

$$\mathrm{Re}_a = \frac{Nd^2\rho}{\mu_a} \tag{2.11}$$

Where μ_a is obtained by substituting the Herschel Bulkley rheological model for shear stress in the expression below:

$$\mu_a = \tau / \dot{\gamma}_{av} \tag{2.12}$$

The average shear rate $\dot{\gamma}_{av}$ is given by the classical equation developed by Metzner and Otto (1957) which relates the shear rate generated by the impeller in the mixing vessel to the impeller rotational speed:

$$\dot{\gamma}_{av} = k_s N \tag{2.13}$$

where k_s is a proportionality constant.

This linear relationship between the average shear rate and the impeller rotational speed is valid only in the laminar regime (Cheng and Carreau, 1994).

Therefore the apparent Reynolds number, Re_a, is written out in its full form (based on the Herschel Bulkley rheological model) as:

$$\mathrm{Re}_a = \frac{k_s N^2 d^2 \rho}{\left[\tau_y + m(k_s N)^n\right]} \tag{2.14}$$

With the above expression for Reynolds number, it is now possible to extend the power draw equation for Newtonian fluids to non-Newtonian fluids because the non-Newtonian power curve can be obtained by a plot of non-Newtonian power number data against apparent Reynolds number. All that is left is for the constant k_s to be determined for the mixing system. It is usually estimated by measuring K_p (which is independent of fluid properties, but dependent on geometrical parameters) for a Newtonian fluid and then back-calculating k_s using data obtained for non-Newtonian fluids (Curran *et al.*, 2000).

Much of the mixing literature is filled with controversy on the dependence of k_s on rheological properties of the fluid and the geometry of the mixing system. According to the equation proposed by Metzner and Otto (Equation (2.13)), k_s is a constant that depends only on the mixing system geometry. However, no agreement can be reached on whether or not k_s depends on the fluid rheology and on the strength of the dependence (Delaplace *et al*, 2000b). For example, Yap *et al.* (1979), Espinosa-Solares *et al.* (1997), Perse and Zumer (2004) state that k_s is a function of

the fluid rheological properties, while Curran *et al.* (2000) found that k_s depends only slightly on the fluid rheology.

Calderbank and Moo-Young (1959) found k_s to be 10 for a number of Bingham and shear thinning fluids with a flow behavior index between 0.05 and 0.6. Metzner *et al.* (1961) extended their work and found k_s to be 11.5 for flat bladed turbines, 13 for pitched blade turbines and 10 for marine propellers.

2.1.4 Mixing Time

Mixing time, t_m, is defined as the time measured from the instant of tracer addition to the time when a specified degree of homogeneity is reached. Usually, a tracer of the same density and viscosity as the bulk fluid is used to evaluate the mixing time. By means of a suitable detector/sensor, the tracer concentration is measured as a function of time at a particular point in the vessel. If the volume of tracer added is known, it becomes possible to calculate an equilibrium concentration, C_∞. The mixing time may then be defined more rigorously as the time required for the tracer concentration at the addition point to reach the equilibrium value. Obviously, the point of addition of the tracer as well as the way in which the tracer is added will influence the mixing time (Harnby *et al.*, 1997). For instance, adding the tracer close to the impeller, vessel wall or liquid surface will affect the mixing time.

In both the turbulent and laminar flow regimes, mixing time can be correlated by the following expression:

$$k_m = Nt_m \tag{2.15}$$

where k_m is referred to as the mixing number or homogenization number which is only a function of geometry (Novak and Rieger, 1975) for a properly designed mixer and m refers to the desired degree of mixedness.

For example, t_{99} is defined the time required for the concentration to reach and remain between $\pm 1\%$ of the final equilibrium value.

The mixing number has units of revolutions and it represents the number of revolutions required to achieve a desired degree of mixing (Tatterson, 1991; Delaplace *et al.*, 2000a).

A number of experimental techniques have been developed and employed for the measurement of mixing time:

- Conductivity method
- Thermal method
- Dye addition method
- Tracer method
- Schlieren method
- Chemical reaction method

More complex methods involve the use of magnetic tracers and radioisotopes (Hayes *et al.*, 1998).

An overview of some of the mixing time measurement methods that have been employed in previous research is presented.

Conductivity Method

This method involves monitoring the change in the electrical conductivity of the fluid after the injection of a conductive tracer. A small volume of an electrolyte solution with a density and

viscosity that is comparable to that of the bulk fluid is fed into the suction zone of the impeller (Hiby, 1981). The variation of conductivity with time is then recorded using a probe placed at a point of high flow velocity (usually the region close to the impeller) until there is no change in the conductivity measurements. This variation in conductivity with time can be converted to a concentration versus time scale using the proper calibration (Nere *et al.*, 2003).

Since the probe only measures the local conductivity, erroneous mixing times may be obtained using this technique particularly if the tank employs multiple impellers or if significant dead zones exist in the tank (Nere *et al.*, 2003; Ford *et al.*, 1972). Another disadvantage of this technique is that it cannot be employed at higher temperatures and in industrial reactors that process organic materials (Nere *et al.*, 2003). Also, the conductivity of the bulk fluid becomes higher after each experimental run, and so it would have to be renewed eventually (Ford *et al.*, 1972). Overestimation of the mixing time especially in the laminar regime is a concern in using the conductivity-probe method (Hiby, 1981).

The conductivity technique may be improved by taking measurements at multiple locations in the tank. Proper estimation of the mixing time is a function of a number of factors namely the location of the probe, size of the probe and number of probes.

Thermal Method

The thermal method uses temperature differences to quantify the degree of mixing. A portion of the bulk fluid is heated to some degrees above the rest of the fluid in the tank. Alternatively, a heat pulse may be generated by an electrical heating element. Fluctuations in temperature are then monitored at one or more points in the vessel using thermistors inserted into the bulk fluid. Energy transfer within the mixing vessel during the homogenization process is caused by

convective mixing and conduction. If the rate of mixing is to be quantified in any meaningful way, the rate of conduction must be small compared to the rate of mixing (Hayes *et al.*, 1998). Also, a high sensitivity temperature measuring instrument is also required to prevent the need for excessive thermal pulse into the fluid (Ford *et al.*, 1972).

The resolution of the thermal method increases with increasing temperature difference between the bulk fluid and the heat pulse, but large temperature differences will result in undesirably large viscosity differences between the two fluids.

In spite of these drawbacks, the thermal method allows for an unlimited number of experimental runs with the same fluid. In addition, no changes in the chemical composition of the bulk fluid occur with the application of the thermal method (Ford *et al.*, 1972).

The dye addition method

The dye addition method is the simplest technique available for mixing time measurements. A dye solution is prepared with some of the bulk fluid and added as a tracer. The mixing time is the time required for the dye to be uniformly distributed throughout the tank contents (Ford *et al.*, 1972; Nere *et al.*, 2003).

Dispersion of the dye may be observed visually, or it may be assessed via the discoloration of the uniformly colored solution. A sample removal method in which the samples are analyzed colorimetrically, chemically or optically, may also be utilized to determine the end point of mixing. However, sample removal disturbs the flow patterns and affects mixing efficiency (Ford *et al.*, 1972). Also, the dye addition technique remains a subjective method for measuring the mixing time since the exact point at which homogeneity is achieved is difficult to establish.

The Schlieren method

This method operates on the principle that optical inhomogeneities, i.e., gradients in refractive indices or Schlieren are present in an inhomogeneous fluid and absent in a homogenous fluid. The time taken for the disappearance of the last optical inhomogeneity is defined as the mixing time (Ford *et al.*, 1972). The method by which the optical inhomogeneities are generated varies. A sample of fluid with a density significantly different from that of the bulk fluid may be introduced. When a light is passed through the resulting mixture, the density gradients produce Schlieren patterns (Hayes *et al.*, 1998). The disadvantage of using this method to generate Schlieren patterns is the extent to which the density gradients themselves enhance the mixing process. Alternatively, two fluids which initially form two superimposed layers may be used to generate the optical inhomogeneities. These optical inhomogeneities arise due to the viscous dissipation of energy when a sphere is rotated in a single viscoelastic fluid.

The disadvantage with the Schlieren method is the lack of knowledge about the time necessary to establish a stationary flow pattern (Ford *et al.*, 1972).

The Chemical Reaction method

The chemical reaction method is a technique that involves the bulk fluid either changing or losing its color due to a chemical reaction with the injected fluid. The reaction could be an acid-base neutralization reaction in which the base and acid are mixed in with the bulk fluid, followed by the addition of the indicator. The extent of the reaction and hence mixing is observed by monitoring the change in the color of the indicator, which differs depending on the type of indicator employed.

A redox reaction may also be used instead of the neutralization reaction and it offers an advantage over the neutralization reaction method in that the color change produced is more distinct (Ford *et al.*, 1972).

With the chemical reaction method, there is always the concern that the reactants may affect the rheological properties of the bulk fluid (Hayes *et al.*, 1998). Also, the effectiveness of this method is dependent on the extent to which the initial reactant is mixed in with the bulk fluid; the impeller may be unable to accomplish the mixing necessary for accurate detection of the mixing time particularly when stagnant regions are present in the tank (Ford *et al.*, 1972).

Liquid-crystal thermography technique

This technique provides mixing time measurements based on the color change of thermochromic liquid crystals when they are subjected to different temperatures. Liquid crystals exhibit a rapid and reversible response to temperature changes over a wide range of temperatures. This means that liquid crystals must be calibrated at the start of the experiment so as to assign particular colors to temperatures over the response range of the liquid crystals (Lee and Yianneskis, 1997).

Radioactive liquid tracer technique

This technique which can be used to measure the mixing time both in pilot scale and large-scale batch mixing systems involves injecting the radioactive tracer along with one of the components of the mixture and monitoring the concentration of the tracer continuously using radiation tracers placed at one or multiple locations in the system. Alternatively, samples may be taken from a single location at regular intervals or large samples from different locations may also be obtained. The average concentration of a group of samples is obtained, from which the standard

deviation is calculated. A plot of standard deviation vs. time can be obtained, and adequate mixing is deemed to have been achieved when the standard deviation becomes constant (Pant *et al.*, 2001)

Electrical Resistance Tomography

Electrical Resistance Tomography (ERT) is a method for the measurement of mixing that is becoming increasing popular in the mixing field. ERT involves the measurement of mixing using an array of resistance tomography sensors. This method can be applied for the measurement of mixing time by following the conductivity changes in space and time after the injection of a pulse of high conductivity fluid tracer (Wang *et al.*, 2000). The procedure for measuring the mixing time in the ERT method involves applying different current patterns to the flow field via electrodes attached on the boundary and the voltages between the electrodes on the boundary are measured. Based on the current-voltage relation, the electrical conductivity distribution of the fluid is estimated and is expressed as pixel images that provide instantaneous information on a concentration distribution in a flow domain at a given location (Kim *et al.*, 2006). In ERT, the mixing time is taken to be the time for the concentration distribution at a plane to reach or nearly reach a uniform distribution after the addition of the secondary fluid (tracer).

However, in spite of the diversity of techniques that have been developed for its measurement, the mixing time is still considered ambiguous and arbitrary. This is because the various techniques available for mixing time measurements, each having an inherently different way of identifying the end point together with the difficulty in selecting a measuring point makes it

difficult to agree on absolute mixing times for any mixing system. Provided there are no significant stagnant zones in the vessel, the measuring point is not of great concern (Chavan *et al.*, 1975).

Another parameter that can be used to determine the homogeneity of a mixing system is the circulation time, t_c, which is considered less arbitrary than the mixing time because it is independent of the tracer addition location and the number of probes.

The circulation time is defined as the time required for a neutrally buoyant particle or blob of tracer contained within the mixing system to complete one circuit of the tank, i.e., to return close to its starting position. If measurement methods involving the use of probe(s) are used for homogenization measurements, then the circulation time is measured as the distance between two successive peaks on the response curve.

Typically, mixing times are two to four times larger than circulation times due to the time required for the relatively quiescent regions of the tank to pass through the impeller and become mixed (Tatterson, 1991).

2.2 *Mixing Time in Non-Newtonian fluids*

A number of researchers have experimentally measured mixing times in non-Newtonian fluids. To show the wide variety of mixing time measuring methods that have been employed particularly for mixing time determinations in non-Newtonian fluids, a summary of their research is provided including the mixing time measuring technique employed and important results are presented below.

Nienow and Elson (1988) measured mixing times in a corn syrup (Newtonian fluid) and 0.8% carboxymethylcellulose (CMC) solution, a non-Newtonian fluid, to characterize the mixing efficiency of a number of impellers at equal power consumptions. They used the visual discolorization of starch/iodine solution to obtain mixing time results and observed higher mixing times with the CMC solutions.

Moo-Young *et al.* (1972) carried out experiments in both Newtonian and non-Newtonian fluids to examine the relationship between mixing time and power consumption and used the results to rank different impellers with regard to the efficiency with which they utilized power. Using aqueous solutions of sodium CMC and an acid-base decolorization method, they observed higher mixing times compared with Newtonian fluids in the laminar regime; specifically, the mixing times for pseudoplastics decreased more rapidly with decreasing Reynolds number than for Newtonian fluids.

Menisher *et al.* (2000) compared the mixing performance of two impellers in a bioreactor by comparing the mixing time at equal power consumptions. They took the mixing time as the time for the disappearance of the pink color of a basic solution of phenolphthalein on neutralization with excess acid.

Carreau *et al.* (1976) studied the effect of fluid elasticity and helical ribbon impeller geometry on the mixing effectiveness as measured by mixing time. Using the discolorization of starch/iodine solution by sodium thiosulphate to obtain mixing time results, they observed that mixing time increased with increasing non-Newtonian behavior due to the existence of stagnant zones in the mixing vessel. Chavan *et al.* (1975) also used the same measuring method to obtain mixing time

results and observed constant mixing times for Newtonian and inelastic shear thinning liquids in the laminar regime (Re < 10).

2.3 *Cavern formation and Mixing time*

Provided there are no stagnant regions in the mixing tank, the most efficient mixer is the one that gives the smallest mixing time for the same power input. This is because the suitability of a mixer for a particular mixing operation depends on its ability to circulate the entire tank contents to avoid the formation of stagnant regions in the mixing tank (Mavros, 2001). Stagnant/solid-like regions in the mixing vessel are commonly encountered in mixing non-Newtonian fluids particularly those possessing a yield stress, at low Reynolds numbers (Ascanio *et al.*, 2003). Formation of these stagnant zones gives rise to a well mixed region surrounding the impeller called a cavern.

It is for this reason that the design of efficient mixing systems for yield-stress fluids is considered a difficult task (Bertrand *et al.*, 1996) since it depends on an accurate mixing time estimate which is a function of the cavern size, the latter which can only be obtained when the phenomena of cavern growth is understood.

Considerable work has been devoted to predicting the formation and growth of caverns in mixing vessels and on this basis, models have been proposed for predicting the cavern size.

Wichterle and Wein (1989) determined the size of the cavern generated in extremely pseudoplastic and plastic suspensions by moving the impeller towards the liquid surface or tank wall and observing the appearance of the dye which had been added to the cavern. From their results and a simple model, they derived the following equation for obtained the cavern diameter, D_c:

$$\mathrm{Re} = \frac{\rho N^{2-n} D^2}{K} = \left(\frac{D_c}{eD}\right)^2 \qquad (2.16)$$

Where ***e*** is an experimentally determined constant that depends on the impeller type.

Solomon *et al.* (1981) developed a physical model based on a torque balance for estimating the cavern diameter, D_c . In developing this model, the following assumptions were made: the cavern shape was assumed to be spherical, a motion at the cavern boundary was assumed to be predominantly tangential and the stress imparted by the impeller at the cavern boundary was equal to the fluid yield stress. Based on these assumptions and by balancing the torque on the cavern walls to that on the impeller shaft, the following equation was developed:

$$\left(\frac{D_c}{D}\right)^3 = \left(\frac{4N_p}{\pi^3}\right)\left(\frac{\rho N^2 D^2}{\tau_y}\right) \tag{2.17}$$

Elson *et al.* (1986) modified the model developed by Solomon *et al.* by assuming that the cavern shape can be described by a right circular cylinder with height, H_c centered upon the impeller:

$$(D_c/D)^3 = \left[1\Big/\pi^2\left(\frac{1}{3}+\frac{H_c}{D_c}\right)\right]N_p\left(\frac{\rho N^2 D^2}{\tau_y}\right) \tag{2.18}$$

Equation (2.18) was proposed for the case where the cavern has not grown up the side wall of the vessel.

The ratio of height to diameter of the cavern, also known as the aspect ratio, varies with impeller type and has been found to range from 0.4 for radial flow rushton turbines to 0.75 for axial flow marine propellers (Elson, 1990; Galindo and Nienow, 1992).

After the cavern has grown up to the side wall, the rate of increase of the cavern height H_c, with impeller rotational speed is expressed as follows (Galindo and Nienow, 1992; Amanullah *et al.*, 1998):

$$\frac{H_c}{D_c} \quad \alpha \quad N^p \tag{2.19}$$

The exponent p is a function of impeller type (Galindo and Nienow, 1992; Galindo *et al.*, 1996). Values of p ranging from 0.76 for the marine propeller to 0.88 for the Rushton turbines have been found (Elson, 1990b).

More recently, Amanullah *et al.* (1998) developed an axial force model for evaluating the cavern diameter. This model was developed by taking the total momentum imparted on the fluid as the sum of both the tangential and axial force components. Assuming a spherically shaped cavern and replacing the average shear stress at the impeller boundary with the yield stress, the following expression for calculating cavern diameter was obtained:

$$\left(\frac{D_c}{D}\right)^2 = \left(\frac{1}{3}\right)\left(\frac{4N_p}{\pi^2}\right)\left(\frac{\rho N^2 D^2}{\tau_y}\right) \tag{2.20}$$

In addition, to assess the mixing performance of different impellers in terms of the size of cavern that they generate, the volume of cavern produced per unit of power input can be calculated and compared for each impeller. Since the cavern size is assumed to be cylindrical, the volume of cavern, V_c, is given by $V_c = \pi(D_c/2)^2 H_c$.

3 Computational Fluid Dynamics

3.1 *Theory*

CFD is the science of predicting fluid flow, heat transfer, mass transfer, chemical reactions and related phenomena by solving the mathematical equations that govern these phenomena using a numerical algorithm (Ford, 2004). Computational fluid dynamics provides relevant data required for conceptual studies of new designs, detailed product. The mathematical equations that govern fluid flow take the form of transport or conservation equations. These equations namely the continuity equations and the Navier Stokes equations describe the changes in the fluid that occur over time due to convection, diffusion, and sources or sinks of the conserved or transported quantity.

The continuity and Navier Stokes equations are statements of conservation of mass and momentum in each of the three component directions respectively. The continuity and Navier Stokes momentum equations and are written out as follows:

$$\frac{\partial \rho}{\partial t} + div(\rho u) = 0 \tag{3.1}$$

$$\frac{\partial}{\partial t}(\rho u) + div(\rho u u) = div(\mu \quad grad \quad u) - \frac{\partial P}{\partial x} + S_{Mx} \tag{3.2a}$$

$$\frac{\partial}{\partial t}(\rho u) + div(\rho u v) = div(\mu \quad grad \quad v) - \frac{\partial P}{\partial y} + S_{My} \tag{3.2b}$$

$$\frac{\partial}{\partial t}(\rho u) + div(\rho u w) = div(\mu \quad grad \quad w) - \frac{\partial P}{\partial z} + S_{Mz} \tag{3.2c}$$

where μ is the viscosity, u, v and w are velocity components in the x, y and z directions, P is the pressure, $div(\mu \quad grad \quad u)$, $div(\mu \quad grad \quad v)$ and $div(\mu \quad grad \quad w)$ are the diffusive flux of the transported species in the x, y and z directions respectively. The same definition would apply to the diffusive flux of the transported species in the y and z directions.

Equations (3.1) and (3.2a-c) describe the continuous movement of fluid in space and time. Numerical solution of these equations requires discretization of the fluid domain and governing equations.

The concept of discretization can be explained by introducing a general variable, ϕ as the dependent variable. In general, this variable is a function of the three space coordinates and time ($\phi = \phi(x, y, z, t)$). A numerical method seeks to determine the values of the dependent variable at a finite number of locations or grid points in the fluid domain. To accomplish this, a set of algebraic equations involving the unknown values of the dependent variable at the grid points and an algorithm for solving these set of algebraic equations are required. These algebraic equations are derived from the differential equations governing ϕ by dividing the fluid domain into subdomains. An assumed profile of ϕ over each subdomain makes the derivation of the algebraic equations from the differential equations possible.

Therefore, both the fluid domain and the differential equations governing ϕ are discretized.

Numerical simulation of the flow field is simplified considerably by noting that the equations governing fluid flow are similar enough that they can be represented by a single equation in terms of the general variable, ϕ introduced earlier:

$$\frac{\partial(\rho\phi)}{\partial t} + div(\rho\phi u) = div(\Gamma \quad grad \quad \phi) + S_\phi \tag{3.3}$$

ϕ could either be a velocity component (Navier Stokes equations), or tracer concentration or 1 in the case of the continuity equation (Jaworski and Dudczak, 1998; Patankar, 1980). The first term on the right hand side is the diffusive flux of ϕ (Γ is the diffusion coefficient which would be μ in the case of the momentum equation), the second term on the left hand side is the convection term. The rate of change term and the source term (representing all other contributions including the pressure gradient) are the first term on the left side and the second term on the right hand side of Equation (3.3) respectively.

Three different methods form the basis for approximating the derivatives that appear in the differential equation by simple functions and obtaining the discretized equations from Equation (3.3) (Versteeg and Malalasekera, 1995). They are the finite element, finite difference and finite volume methods.

The CFD software used in this work, Fluent, uses a finite volume based technique to discretize the differential equations; therefore, this method will be described in more detail.

3.1.1 Finite Volume Method

The first step in the finite volume method is to divide the fluid domain into discrete control volumes with each control volume surrounding a grid or nodal point. This step is also referred to as grid generation. Grid generation is accomplished using a grid or mesh containing elements of many shapes and sizes. If the flow domain is two dimensional (i.e., function of two space

coordinates), the elements are usually quadilaterals or triangles. For a three dimensional domain, the elements could be tetrahedra, prisms, pyramids or hexahedra (Paul *et al.*, 2004)

The differential equations are then integrated over each control volume and the unknown terms in the resulting integral equation are substituted by finite-difference type approximations. This step transforms the integral equations into a set of algebraic equations. The algebraic equations are then solved iteratively to obtain the profile of ϕ in the flow domain.

For illustrative purposes, if the one dimensional steady state flow involving convection and diffusion is considered (without any sources), and integration is carried out over the control volume surrounding the node P as shown in Figure 3.1:

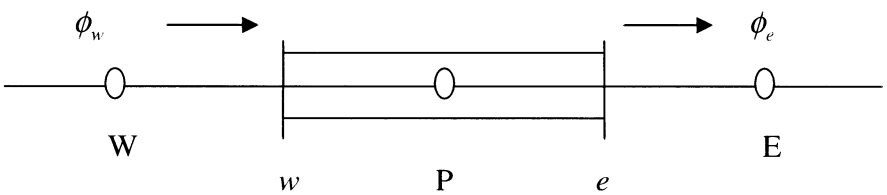

Figure 3.1 Depiction of a control volume around node P; Neighboring nodes are designated W and E

the following integral equation results:

$$(\rho u\phi)_e - (\rho u\phi)_w = \left(\Gamma \frac{d\phi}{dx}\right)_e - \left(\Gamma \frac{d\phi}{dx}\right)_w \tag{3.4}$$

Where *e* and *w* are the control volume faces.

It is usually convenient to define two variables, F and **D** to represent the convective mass flux per unit area and the diffusion conductance at the cell faces:

$$F = \rho u \qquad \text{and} \qquad \mathbf{D} = \frac{\Gamma}{\partial x} \tag{3.5}$$

Equation (3.4) can now be rewritten as:

$$F_e\phi_e - F_w\phi_w = D_e(\phi_E - \phi_P) - D_w(\phi_P - \phi_W) \tag{3.6}$$

A number of methods or discretization schemes exist for approximating the diffusive and convective terms at the control volume faces in Equation (3.4). They include central differencing, upwind differencing scheme, the hybrid differencing scheme, the power law scheme and higher order differencing schemes such as the Quadratic Upwind differencing scheme (QUICK). A brief summary of each of these schemes is presented to highlight their features and provide some background that would be necessary to decide on the numerical scheme to implement in the CFD simulations.

Central Differencing Scheme

This scheme uses linear approximations to calculate the convective and diffusive fluxes at the control volume faces, *e* and *w* (see Figure 3.1), i.e.:

$$\phi_e = \frac{\phi_P - \phi_E}{2} \tag{3.7}$$

$$\phi_w = \frac{\phi_W - \phi_P}{2}$$

The same procedure is followed to evaluate the diffusive fluxes:

$$d\phi_e = \phi_E - \phi_P \tag{3.8}$$

$$d\phi_W = \phi_P - \phi_W$$

These approximations are then substituted back into the integral equation (Equation (3.4)) to give the discretized or algebraic equation

The algebraic equation usually has the following general form:

$$a_p \phi_p = \sum a_{nb} \phi_{nb} + b \tag{3.9}$$

where ϕ_p and ϕ_{nb} are the dependent variables at the grid point of interest and the neighbor grid points respectively and b is the linearized source term. The expressions for the linearized coefficients a_p and a_{nb} vary depending on the discretization scheme employed.

However, for situations involving combined convection and diffusion, the central differencing scheme has been found to deviate substantially from the exact solution to the differential equation. Even though it is commonly held that when the number of computational cells used in a numerical simulation is large (approaching infinite), the numerical results are exactly the same as the true solution of the transport equation regardless of the discretization scheme used, the reality is that an infinite number of cells can never be used in a numerical problem (because it would make the computation time unacceptably long), so that the results can only be physically accurate when the discretization scheme has the following three fundamental properties: conservativeness, boundedness and transportiveness.

Conservativeness means that the flux of ϕ leaving a control volume face must be equal to the flux of ϕ entering an adjacent control volume through the same face. This criterion will ensure the conservation of ϕ for the whole solution domain.

Boundedness will ensure that when the resulting algebraic equations are solved iteratively using a suitable solution technique, a converged solution will be obtained. A discretization scheme that obeys this criterion will satisfy the following characteristic, known as the Scarborough criterion:

$$\frac{\sum |a_{nb}|}{|a_p'|} \begin{cases} \leq 1 \ at \ all \ nodes \\ < 1 \ at \ one \ node \ at \ least \end{cases} \tag{3.10}$$

Another requirement for boundedness is that all coefficients must have the same sign (usually positive).

Transportiveness means that changes in the Peclet number ($P_e = \frac{\rho u L}{\Gamma}$: measure of the relative strengths of convection and diffusion) should be accurately reflected in the directionality of influencing (based on the flow direction) by the conditions at one node on the conditions at another node.

In view of these properties, the central differencing scheme fulfills the conservativeness criterion and partially fulfills the boundedness criterion (except for the possibility that some of the coefficients may be negative depending on whether convection dominates over diffusion) and fails the transportiveness criterion at high Peclect numbers.

Therefore, it became necessary to introduce other discretization schemes with favorable properties.

Upwind Differencing Scheme

This scheme attempts to acquire the transportiveness property by stipulating that taking into account the flow direction, the convected value of ϕ at a control volume face is equal to the value at the upstream node.

Thus, the upwind scheme possesses the transportiveness, boundedness and conservativeness properties. However, this scheme gives misleading results at large values of the Peclet number because it overestimates diffusion (false diffusion) at large Pe numbers (Patankar, 1980), and for lower Peclet numbers, it is not as accurate as the central difference scheme (Ranade *et al.*, 1989).

Hybrid Differencing Scheme

The hybrid scheme as the name implies is a combination of two schemes; the central differencing and the upwind schemes. This scheme evaluates the convective flux through each control volume face based on the Peclet number at that control volume face. For Peclet numbers less than 2 (the value of the Peclet number at which the central differencing scheme fails the transportiveness criterion), the central differencing scheme is used for the approximations and at Pe numbers greater than 2, the upwind differencing scheme is used.

Power law Scheme

The power law scheme is a better alternative to the hybrid scheme. It sets the diffusion equal to zero when the Peclet number exceeds the value of 10. For Pe values between zero and 10, the convective flux is approximated using a polynomial expression.

Higher order differencing schemes

With the exception of the central differencing scheme, the accuracy of the hybrid and upwind schemes is first order in terms of the Taylor series truncation error. Therefore, even though these schemes possess the transportiveness property and are very stable, they are prone to numerical diffusion errors. These errors can be minimized by using higher order differencing schemes such as the QUICK scheme.

The QUICK scheme has a third order accuracy in terms of the Taylor series truncation error. The value of ϕ at the control volume face is calculated using a quadratic function passing through three points: two bracketing nodes (one on each side of the face) and an upstream node. The QUICK scheme is more accurate than the central differencing, upwind or hybrid schemes, but can give undershoots and overshoots compared to the exact solution to the differential equations.

3.1.2 Calculation of the Flow Field

As mentioned earlier, discretization yields a finite set of coupled algebraic equations that need to be solved iteratively to give a distribution of ϕ at nodal points (Versteeg and Malalasekera, 1995). However, there is still some difficulty with the calculation of the velocity field. The momentum equations for the velocity components still contain an unknown pressure gradient that forms a part of the source term. As such, the discretized momentum equations can only be

solved when the pressure field is specified in some manner. The only specification for the pressure field that is available is an indirect one: when the correct pressure field is substituted into the momentum equations, the resulting velocity field will satisfy the continuity equation.

As a result, the calculation of the flow field has been achieved through the development of algorithm known as SIMPLE (Semi-Implicit Method for Pressure-Linked Equations). In a nutshell, the SIMPLE algorithm starts by guessing a pressure field and substituting the guessed pressure field into the momentum equations which are then solved to obtain guessed velocity components. As per the indirect specification of the correct pressure field, the guessed pressure field is improved using the continuity equation as a pressure correction equation. The corrected pressure is in turn used to correct the guessed velocity field (via a velocity correction formula). This procedure (with the corrected pressure as the new guessed pressure) is repeated until the resulting velocity field satisfies the continuity equation.

Other algorithms have been proposed to improve the SIMPLE algorithm since this algorithm neglects the effect of neighbor-point velocity corrections which results in a pressure correction equation that does not do a good job of correcting the velocities.

The SIMPLER (SIMPLE-Revised) algorithm is an improved version of the SIMPLE algorithm that uses the discretized continuity equation to derive a discretized pressure equation based on pseudovelocities that are composed of the neighbor point velocities and contains no pressure. The SIMPLER algorithm also improves the rate of convergence of the SIMPLE algorithm.

The SIMPLEC (SIMPLE-Consistent) algorithm further improves the SIMPLE algorithm by manipulating the momentum equations such that the velocity correction equations omit terms that are less significant than those omitted by SIMPLE. However, it follows the same sequence of steps as in the SIMPLE procedure.

The PISO (Pressure Implicit with Splitting of Operators) algorithm is an extension of the SIMPLE algorithm with a further corrector step to enhance it.

3.1.4 Solution of the Algebraic Equations

The process of discretizing the transport equations yields a system of linear algebraic equations which need to be solved to obtain a profile of the transported quantity in the flow domain. There are two families of solution techniques for linear algebraic equations: direct methods and indirect (iterative) methods. Iterative methods are generally considered to be more economical than direct methods for solving large system of equations because the latter requires the storage of all the coefficients in the set of equations in the computer memory, whereas, iterative methods require the storage of only the nonzero coefficients in the computer memory. Also, direct methods are slow to converge when the system of equations is large. Therefore, they are not considered suitable for general CFD procedures. Iterative methods involve the repeated application of a simple algorithm until a solution that is close to the correct solution of the algebraic equations is obtained (convergence). A number of iterative methods exist of solving linear algebraic equations:

Gauss-Siedel point by point method: This method is regarded as the simplest of all iterative methods. It involves the calculation of the values of the dependent variable by visiting each grid point in a certain order. As each grid point is visited, the corresponding value of the dependent variable is altered as follows:

$$\phi_p = \frac{\sum a_{nb}\phi_{nb}^{*} + b}{a_p} \tag{3.11}$$

where the discretization equation is given by equation (3.6). ϕ_p is the value of the dependent variable at the visited grid point that we wish to calculate and ϕ_{nb}^{*} is the neighbor point value present in the computer storage. When all the grid points have been visited in this way, one iteration has been completed.

Line by Line Method: This method is a combination of the Gauss Siedel point by point method and the TDMA (TriDiagonal-Matrix Algorithm) method for one-dimensional situations. For three dimensional problems, the TDMA method is applied line by line on a selected plane and then repeated for another plane. The essence of this method can be understood by considering a particular line and the discretization equations for the grid point along the chosen line. These equations contain the values of the dependent variable from neighboring lines in the same direction. Assuming that the values of the dependent variable at the grid points are known from their latest values, they can be substituted into the discretization equations which would make these equations look like one dimensional equations. The method of TDMA for one-dimensional equations can then be applied to solve the equations along the chosen line.

3.2 *CFD in Stirred Tanks*

Numerical simulation of stirred vessels is complicated because of the inherent unsteady flow structure. The presence of baffles in the stirred tank further complicates the simulation of the flow field in the mixing vessel since the relative motion between the stationary baffles and the rotating impeller blades has to be incorporated to order to completely simulate the flow field

(Brucato *et al*, 1998; Perng and Murthy, 1993; Deglon and Meyer, 2006; Sommerfeld and Decker, 2004). The simplest approach has been to treat the flow field in the vessel as stationary with experimentally determined impeller boundary conditions specified as inputs to the outer cylindrical surface of the region swept by the impeller (Sommerfeld and Decker, 2004; Ranade, 1997; Javed *et al.*, 2006). Alternatively, the action of the impeller is represented as body forces using distributed sources of momentum (Luo *et al.*, 1993). However, these approaches are inherently limited since their applicability depends on the availability of experimental data so that they cannot be used to screen alternative mixer configurations (Ranade and Dommeti, 1997). In addition, they fail to take into account the details of the flow between the impeller blades, which may be necessary for a realistic simulation of the hydrodynamics in mixing vessels (Ranade, 1997).

Attempts have been made to capture the details of the flow between the impeller blades by simulating the full time varying flow within and outside the impeller region using a combination of moving and deforming grids. The two impeller modeling methods developed for this purpose are the *Multiple Frame of Reference (MRF) method* and the *sliding mesh method.*

The *MRF method* involves resolving the impeller geometry by a numerical grid and calculating the cylindrical region around the impeller in a rotating frame of reference while the rest of the vessel is calculated in the stationary frame of reference by resolving the vessel geometry and baffles. The simulations in each of the stationary and rotating regions are conducted under steady state assumptions in their respective frames of reference. A steady transfer of information takes place at a predefined interface between the two frames (Oshinowo *et al.*, 2002). The MRF method is recommended for situations involving relatively weak impeller-baffle interactions

since the solution with the impeller in one position relative to the blades will be the same as the solution obtained for a different position (Paul *et al.*, 2004).

The sliding mesh approach developed by Luo *et al.* (1993) is a time-dependent solution in which the flow domain is divided into two cylindrical, non-overlapping sub-domains, each gridded separately. The grid surrounding the impeller moves according to the impeller speed with respect to the stationary domain (containing the baffles) fixed in the laboratory frame of reference. The two domains are implicitly coupled at the interface via a sliding mesh algorithm (Montante *et al.*, 2001; Brucato *et al.*, 1998). Transient simulations are conducted at each time step for each relative position of the stirrer and baffles (Montante *et al.*, 2001). Using this approach, the impeller motion is realistically modeled because the grid surrounding the impeller rotates giving rise to a time-accurate simulation of impeller-baffle interactions. This model represents the most rigorous solution method for stirred tank simulations (Paul *et al.*, 2004; Brucato *et al.*, 1998). However, results obtained using the MRF model have been found to be comparable to that obtained using the sliding mesh impeller model so that the latter is preferred to reduce computational expenses (Deglon and Meyer, 2006).

Another impeller modeling method is the *computational snapshot approach* developed by Ranade and van den Akker, 1994). This method is considered an intermediate to both the MRF and sliding mesh methods since it attempts to simulate the flow details between the impeller blades without solving the full time-dependent flow equations (Ranade and Dommeti, 1996). Instead, simulation of the impeller motion is carried out by keeping the impeller blades fixed at a particular position with respect to the baffles which is analogous to taking a snapshot of the rotating impeller (Ranade, 1997; Ranade and Dommeti, 1996). This approach was developed on

the basis that for most engineering applications, knowledge of the full flow field which becomes cyclically repeating after a few impeller rotations may not be necessary (Ranade and Dommeti, 1996).

In addition to the impeller rotation model, CFD modeling of stirred tanks requires the selection of an appropriate grid resolution and discretization scheme (Deglon and Meyer, 2006).

3.2.1 Grid Resolution

There is a consensus that in general, the larger the number of cells used in a CFD simulation, the higher the accuracy of the predictions. More specifically, optimal meshes are defined as non-uniform, i.e., finer in areas where large variations occur and coarser in regions with smaller gradients (Versteeg and Malalasekera, 1995).

A number of authors have attempted to improve the accuracy of the numerical predictions by using refined meshes. Some of the important findings are summarized below.

Ranade (1997) used a large number of computational cells (more than double that used in recent studies) to simulate the flow generated by the Rushton turbine in the laminar regime and observed that the power numbers in the turbulent regime were underpredicted by 20%. One of the reasons for the observed underprediction was thought to be as a result of inadequate grid resolution. As well, his grid was unable to capture the full details of the trailing vortices behind the impeller blades, a result he obtained in an earlier study (Ranade and Dommeti, 1996) and which he attributed to the use of relatively coarse grids. He concluded that further grid refinement was necessary to obtain better predictions in the turbulent regime.

Deglon and Meyer (2006) studied the effect of grid resolution on CFD predictions of the flow field, power number and mean velocity and observed that as the grid resolution is increased, the power number predictions (as compared to experimental measurements) also improve by about 20% between the coarsest and finest grids used. They also concluded from their studies that the predicted velocity profiles were improved by using finer grids although the dependence of the velocity predictions on the grid resolution were not observed to be as strong as that for the power number.

Bujalski *et al.* (2002) employed a finer mesh in the areas of high velocity gradients in the mixing tank (to give a total of 115,444 cells) and obtained smaller homogenization numbers (compared with results obtained using a structured mesh with 71344 computational cells) which were closer to the experimental measurements. There was also a two-fold reduction in the difference between the experimental and predicted power numbers with grid refinement.

Kukukova *et al.* (2005) studied the influence of grid density on the simulated results and concluded that the best results (in comparison with experimental measurements) were obtained when the grid was refined in the impeller region with a structured grid elsewhere in the mixing tank where gradients were not expected to be large.

Errors due to inadequate grid resolution can be eliminated by conducting grid independence studies. Grid independence involves successive grid refinement of an initially coarse grid until no changes in key results are observed (Versteeg and Malalasekera, 1995; Deglon and Meyer, 2006). For example, Shekhar and Jayanti (2003) performed simulations on an initial grid

consisting of 298,368 cells and then performed additional simulations on a grid consisting of 440,832 cells (32% cell increase) and observed insignificant deviations in the results obtained from each of these grids. Therefore, they utilized the smaller grid size for the rest of their research to reduce computational requirements.

3.2.2 Discretization Scheme

Deglon and Meyer (2006) studied the effect of grid discretization on power consumption and mean velocity field predictions and observed that higher order discretization schemes provided better power number predictions with the QUICK discretization scheme providing the best power number predictions (10% lower than experimental values) compared with first order upwind discretization scheme.

Aubin *et al.* (2004) studied the effect of the discretization scheme on the power consumption and circulation times and observed that both the first order upwind discretization scheme and the QUICK scheme under predict the power number. For the circulation time, there was little effect of the discretization scheme on the results, even though the QUICK scheme gave the best value of the circulation time.

Brucato *et al* (1998) carried out comparisons between the first order upwind and QUICK discretization schemes and concluded that on the finest grids, the numerical predictions are not vastly different for both of these schemes.

3.3 *CFD measurements of Mixing Time in Stirred Tanks*

The application of CFD to the measurement of mixing times in stirred tanks is a growing field. Some of the work conducted by some researchers in the mixing area is presented below.

Sahu *et al.* (1999) used a zonal modeling technique to predict the flow field generated by five axial flow impellers. The predicted flow field was then used to estimate the mixing time for these impellers by solving conservation equation for the tracer. The mixing time was taken as the time taken for the tracer to reach within 99% of the completely mixed tracer concentration. They observed that the modeled mixing times compared well with the experimental mixing times to within 5-10% and they went further to state that perfect agreement may be assumed since experimentally measured values of mixing time have an inherent standard deviation of 5-10%.

Montante and Magelli (2004) sought to investigate the capability of CFD tools to correctly forecast the homogenization process and mixing time results. Modeling a multiple Rushton impeller system in the commercial CFD code, CFX-4, they studied the influence of impeller spacing and turbulent Schmidt number on the mixing time and concluded that overall, CFD is able to correctly predict the homogenization dynamics, mixing time as well as the effect of impeller number and spacing on mixing performance.

Montante *et al.* (2005) utilized two commercially available CFD codes, CFX and Fluent to study the homogenization process and obtain mixing time results. In addition to investigating the capability of these codes to produce accurate results, they also sought to develop a consistent computational procedure that could be confidently applied to both Newtonian and non-Newtonian pseudoplastic liquids. Using the Sliding Grid method in CFX-4, and the multiple

reference frame method in Fluent 6 to model the mixing of multiple down pumping 45° pitched blade turbines in a baffled stirred tank, they observed that CFD provides a good picture of the homogenization process, but the actual mixing time results were overestimated by 11-40% (depending on the measuring position) when compared with experimental results.

Bujalski *et al.* (2002) assessed the CFD predictions of mixing time by comparing the numerical results with experimental data. In an earlier work, they had used the Sliding mesh method in the Fluent CFD code (version 4.4.7) to obtain mixing time predictions for a stirred tank equipped with two Rushton turbines, and observed that the predictions were 2 to 3 times longer than experimental values. Therefore, using a refined mesh, employing the MRF method and using a newer version of the Fluent code, better agreement of the dimensionless mixing time predictions with experimental values were obtained.

These authors also investigated the effect of the radial position of the tracer addition point on simulated mixing time results. Using the commercial CFD software, CFX 4.3 to predict the flow field and mixing times and the sliding mesh method, they found that CFD simulations over-predicted the mixing times by a factor of approximately 2. The tracer addition point was found to have a strong effect on the simulated mixing time results, an observation that was inconsistent with experimental findings. In general, a tracer addition point that was closer to the sliding mesh boundary gave shorter simulated mixing times (Bujalski *et al.*, 2002). Osman and Varley (1999) also obtained mixing times from CFD that were approximately twice as long as the experimental mixing times.

Javed *et al.* (2006) attempted to analyze the discrepancies between experimental and simulated mixing results by simulating both the mixing measurements and hydrodynamics and comparing

the predicted results with experimental mixing time measurements. Using the Fluent CFD code to model the stirred tank containing water and equipped with a 6-bladed Rushton turbine they observed good agreement between predicted and measured tracer concentration profiles. The local and global mixing times for homogenization levels of 95% and 99% were found to be 16% shorter than the corresponding experimental values.

Objectives

From the literature review, it is clear that the mixing performance of impellers in highly viscous shear thinning fluids possessing a yield stress needs to be investigated as little research as been devoted to the numerical simulation of homogenization in stirred tanks containing non-Newtonian fluids. A study of the effect of mixing system configuration, fluid properties and power consumption on the mixing time represent necessary steps towards optimization of the mixing system.

Therefore, the objective of this work is to study the effect of the following parameters on the mixing time of a tracer injected into aqueous solutions of xanthan gum:

- Power Consumption
- Impeller clearance from tank bottom
- Impeller type
- Yield stress
- Impeller speed

CFD has become a useful tool in the study of mixing systems. It will be utilized in conjunction with experiments to provide a complete understanding of the mixing process and aid mixing system design. Since CFD modeling of yield stress fluid mixing is limited, this work should provide useful data which can be used to assess the capability of CFD tools to predict the homogenization process (and the resulting mixing time) of such complex fluids.

4. Experimental

4.1 *Experimental Setup*

The experimental setup (Figure 4.1) used in this work consists of a transparent acrylic cylindrical tank of outer diameter, **T** = 40 cm and height equal to 60 cm. The flat-bottomed tank was fitted with four equally spaced flat baffles each with a width, *w*, equal to 10% of the tank diameter and height equal to the tank height. The baffles destroy undesirable vortices created due to the swirl of the fluid in the mixing tank and help promote good mixing. The fluid height, **H** was maintained constant at a height equal to the tank outer diameter, **T**.

Three axial flow impellers were utilized in the experiments: 4-bladed 45° Pitched Blade Turbine, the Marine Propeller and the Lightnin A320 impeller, each having a diameter, **D** of 15.5 cm. This diameter is defined as the diameter of the circle that encloses the projection of the impeller onto a plane.

The impellers were mounted on a centrally located 2.54 cm diameter shaft and driven by a 2 hp motor mounted on the shaft (Neptune Chemical Pump Co., Lansdale, PA). The clearance of the impeller (distance from the midpoint of the impeller to the vessel bottom) was varied from 13.5 cm to 20 cm

Torque measurements were obtained using a torquemeter (Hoskin Scientific Limited, Burlington, ON) operating in the range 0-20 Nm and recorded by the data acquisition system. The impeller rotational speeds were measured using a hand-held digital Tachometer.

Mixing time experiments were conducted using a Model 226 conductivity probe (Rosemount® Analytical, Irvine, CA) placed 6cm below the fluid surface, midway between the shaft and vessel wall. The variation of conductivity with time was also recorded using the data acquisition system.

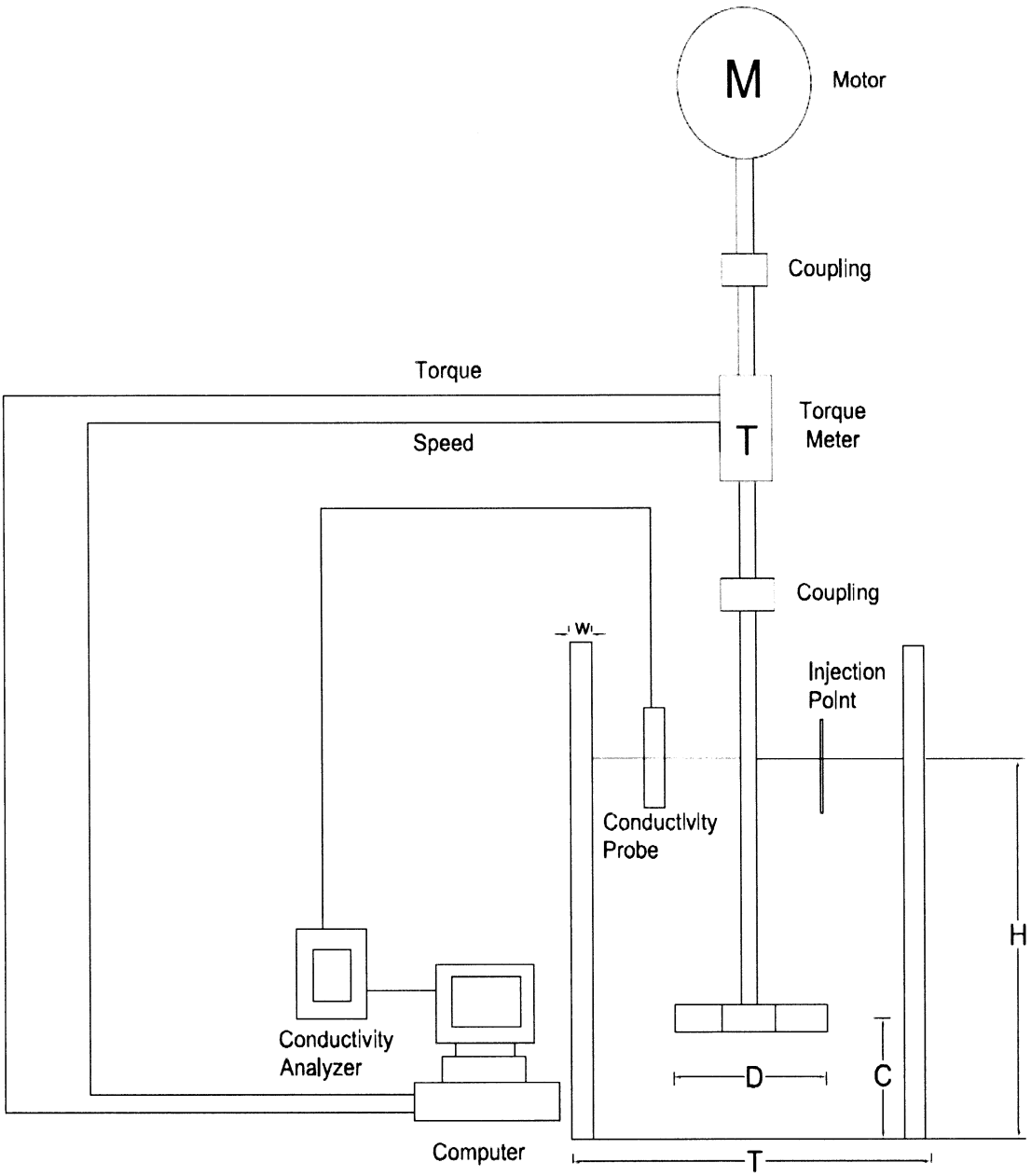

Figure 4.1 Schematic of Experimental Set up

4.2 *Materials*

Xanthan Gum Powder was used for the preparation of three aqueous xanthan gum solutions of concentrations 0.5 wt%, 1 wt% and 1.5 wt%. The xanthan gum powder was obtained from Archer Daniels Midland Company (Decatur, IL). Table salt was used for the preparation of the tracer solution used in the mixing time experiments.

4.2.1 Xanthan Gum

Introduction and Structure

Xanthan gum is a high molecular weight extracellular polysaccharide produced by the submerged fermentation of bacteria of genus Xanthomonas, usually *Xanthomonas campestris*. The unique rheological properties of xanthan gum solutions namely the high viscosity it imparts to aqueous solutions and the stability of the apparent viscosity of the resulting solutions over wide ranges of temperature, pH and ionic strength (Garcia-Ochoa and Casas, 1994) have been exploited in food, petrochemical and pharamaceutical applications and oil recovery (Galindo and Nienow, 1993; Whitcomb and Macosko, 1978, Amanullah *et al*, 1998).

A xanthan gum molecule has a backbone similar to that of cellulose with trisaccharide side chains attached to alternate sugar residues on the main chain (Katzbauer, 1998; Garcia-Ochoa and Casas, 1994). Its molecular weight is usually reported as $2\times10^{6}\,Da$ (the Dalton (Da) is a measure of molecular weight or mass; one hydrogen atom has a mass of $1.66\times10^{-24}\,g$ or 1 Da).

The secondary structure (i.e., backbone conformation) of xanthan gum is reported to consist of a five-fold helical structure.

The high viscosities of xanthan gum aqueous solutions result from the interaction between the molecules in solutions. In aqueous solutions, xanthan gum undergoes a conformational transition

from a disordered chain conformation (coil shape) at elevated temperatures and low ionic strength to an ordered shape (double stranded/dimeric or helix) at higher salt concentrations (Garcia-Ochoa and Casas, 1994; Casas *et al.*, 2000).

Rheology

Aqueous solutions of xanthan gum are shear thinning (Funahashi *et al.*, 1987; Hannote *et al.*, 1991; Katzbauer, 1998) and exhibit a yield stress (Moore *et al.*, 1995). The rheology of xanthan gum solutions has been modeled using the power law, Casson and the Herschel-Bulkley rheological models, where the Casson model is generally used to fit shear-stress vs. shear rate data at low shear rates (Amanullah, 1998; Elson *et al.*, 1986; Torrestiana *et al.*, 1991). Solomon *et al.* (1981) found that the rheological data for xanthan gum were well fitted with the Herschel Bulkley equation over the whole shear rate range ($0.01s^{-1}$ to $1000s^{-1}$).

For the measurement of yield stresses when the power law model was used, Galindo and Nienow (1992, 1993) and Hannote *et al.* (1991) used a stress relaxation technique proposed by the latter.

4.3 *Impeller Specifications*

4.3.1 Pitched Blade Turbine

The pitched blade turbine used in this work has four 45 degree angle blades, which is the most common pitched blade turbine blade angle, and an outer diameter of 15.5 cm. The impeller was rotated to give a downward direction of pumping, which is the typical pumping direction employed with pitched blade turbines. These impellers can be made up pumping only by reversing the direction of rotation or changing the blade angle (Dickey, 2001).

4.3.2 Marine Propeller

For this work, a marine propeller with three blades and an outer diameter of 15.5cm was used. The impeller pitch was 1.5. Pitch is defined as the theoretical distance traveled by the blades in a single rotation of the propeller (Dickey, 2001).

4.3.3 Lightnin A320

The A320 impeller (Lightnin) with three blades and an outer diameter of 15.5cm was used in this work. The A320 is an axial flow impeller that has been recommended for higher viscosity applications requiring high flow in the transitional regime.

Photos of the PBT impeller, marine propeller and A320 impeller are shown in Figure 4.2.

Table 4.1 summarizes the specifications of these three impellers in terms of the power number (N_p) and flow number, N_Q ($N_Q = \frac{Q_{impeller}}{ND^3}$; where $Q_{impeller}$ is the impeller pumping capacity (Paul *et al.*, 2004))

Table 4.1: PBT, Marine Propeller and A320 Impeller Specifications

Impeller Type	*Np*	N_Q
PBT	0.66	0.42
Marine Propeller	1.16	0.47
A320	0.63	0.64

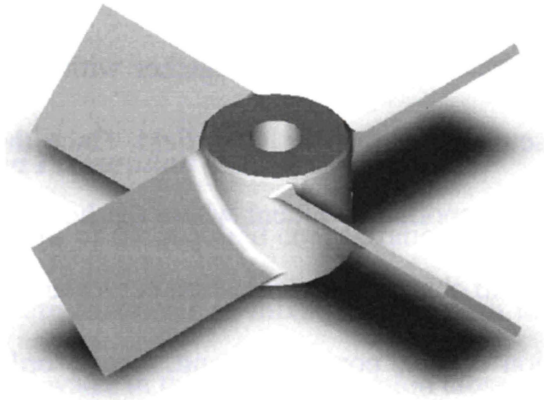

Pitched Blade Turbine

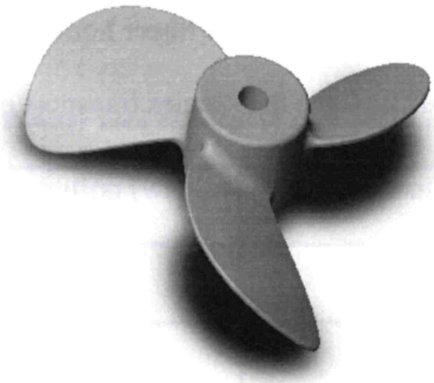

Marine Propeller

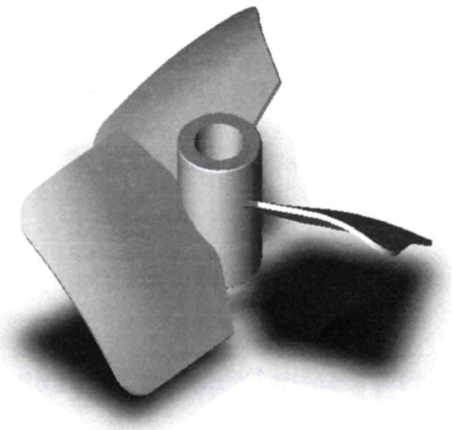

A320 Impeller

Figure 4.2: PBT, marine propeller and A320 Impeller used to study mixing in yield stress fluids

4.4 *CFD Model*

The preprocessor software Mixsim version 2.1 together with Fluent (version 6.3) was used to model the experimental setup and solve the flow field. Once the flow field was numerically calculated, the model was transported to Fluent where the homogenization of an inert tracer in the flow field was simulated to obtain homogenization curves and numerical mixing time results. The MRF impeller rotation model, power law and second order discretization schemes for momentum and pressure respectively, the SIMPLEC algorithm for pressure-velocity coupling and the Gauss Siedel point by point method (see pp. 29-36 for more information) were used for all the numerical calculations of the flow field. For tracer homogenization simulations, the power law discretization scheme was used to solve the species transport equation.

5. Procedure

5.1 Experimental

5.1.1 Xanthan Gum Solution Preparation

To prepare xanthan gum solutions of the required concentration, the mixing tank was filled with tap water to a height **H** = 40 cm (diameter of mixing tank). With the stirrer on, xanthan gum powder was added slowly to the water in the tank in the region close to the impeller. The mass of xanthan gum powder used depends on the desired xanthan gum solution concentration as shown in Table 5.1 below:

Table 5.1 Mass of Xanthan Gum Powder used to prepare each batch of the 0.5 wt%, 1.0 wt% and 1.5 wt% solutions

Xanthan Gum Solution Concentration (wt %)	Mass of Xanthan Gum Powder (g)
0.5	218.28
1.0	435.32
1.5	656.28

The resulting solution was stirred continuously for two hours to achieve a homogeneous xanthan gum solution. To investigate the effect of yield stress and clearance on the mixing time, the PBT impeller was used.

The density of the resulting solution was measured using a picnometer.

5.1.2 Rheological Measurements

The rheology of the test fluids was measured using a Bohlin CVO Rheometer (Malvern Instruments Limited, UK) in the shear rate range 0.04 s^{-1} - 230 s^{-1}.

The shear stress versus shear rate data obtained using the rheometer (see Figure 5.1) were fit to the Herschel Bulkley rheological equation for shear stress (Equation (2.7) to obtain model parameters for the 0.5 wt%, 1 wt% and 1.5 wt% xanthan gum solutions used in this work (Table 5.2). This fitting of the rheological data was facilitated by the curve fitting tool in the data acquisition software of the rheometer which allowed for the data to be automatically fit once the desired rheological model had been selected.

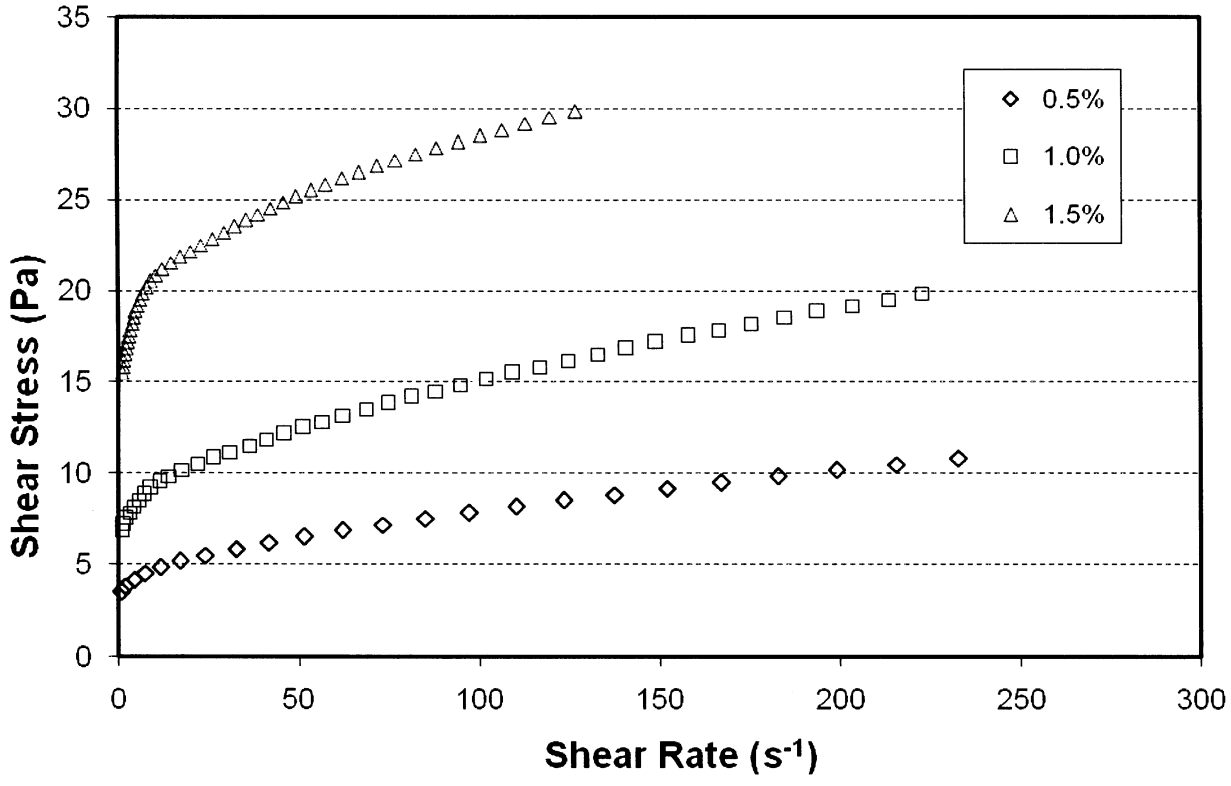

Figure 5.1: Shear stress versus shear rate for 0.5 wt%, 1.0 wt% and 1.5 wt% xanthan gum solutions measured using a Bohlin rheometer

Table 5.2: Rheological Parameters obtained from fitting rheological data (Figure 5.1) to Equation (2.7)

Concentration (wt %)	τ_y [Pa]	K [Pa.s^n]	n [-]	ρ [kg/m^3]
0.5	1.789	3	0.11	997.36
1.0	5.254	8	0.12	991.80
1.5	7.455	14	0.14	989.76

5.1.3 Power Consumption measurements

Power consumption for each impeller type and xanthan gum solution concentration was calculated from torque measurements obtained at each impeller rotational speed. From the measured torque values, M_m, a residual torque value due to the shaft guiding system, M_r was subtracted to obtain corrected torque measurements, M_c. The residual torque was measured by running the mixing system in air for every measurement.

$$M_c = M_m - M_r \tag{5.1}$$

The Power consumption was then calculated according to Equation (2.9) using M_c.

5.1.4 Mixing time measurements

Mixing time experiments were conducted by injecting a tracer prepared by dissolving 30g of NaCl in 60ml of xanthan gum solution.

At time t = 0, with the stirrer on and the Labview data acquisition system turned on, the tracer was injected into the bulk xanthan gum solution. The mixing progress was monitored by means of the conductivity-time graphs generated automatically by the program. Once no change in the conductivity of the solution with time was observed, data collection was discontinued. The

mixing time was determined as the time taken for the conductivity to reach within ± 2% of the final steady state conductivity value (Figure 5.2).

To introduce the least disturbance to the flow field, the probe was kept in a slant position in between two baffles (approximately 45 degrees to the horizontal) and at least two inches away from the inner vessel wall as specified by the probe manufacturers to eliminate wall effects. Mixing time measurements were conducted for 0.5%, 1% and 1.5% xanthan gum solutions. They were also conducted at impeller clearances C1=H/3, C2=2H/5, C3=H/2 and for the pitched blade turbine, marine propeller and Lightnin A320. Each measurement was repeated three times from which the mean and standard deviation were calculated.

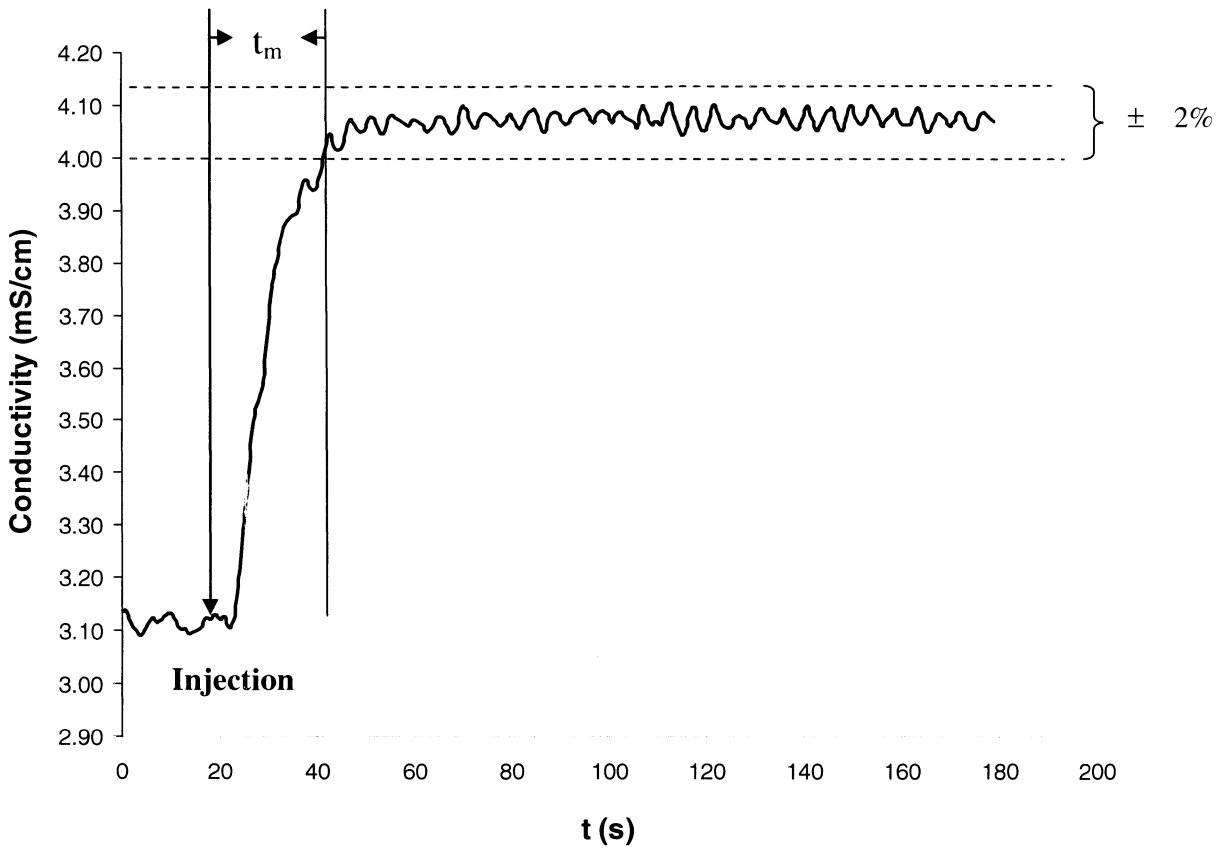

Figure 5.2 Experimental Determination of Mixing Time for PBT rotating at N = 450rpm mixing 1% xanthan gum solution at C3 = 20cm

5.2 Numerical

5.2.1 Model Set up and Flow field calculation

The dimensions of the mixing tank, shaft and impeller was defined in Mixsim 2.1. The flow regime was specified as laminar, and rheological parameters of the solution (Table 2) were specified in the Herschel Bulkley model in Mixsim 2.1. In Mixsim 2.1, when the Herschel Bulkley model is specified as the viscosity model, the fluid viscosity is calculated via the following equation (Fluent Inc., 2006):

$$\mu_a = \frac{\tau_y + K\left[\dot{\gamma}^n - \left(\tau_y / \mu_0\right)^n\right]}{\dot{\gamma}} \qquad (5.2)$$

where μ_0 is the yielding viscosity defined as the viscosity of the fluid before the yield stress has been exceeded (Fluent Inc., 2006). It was calculated for each xanthan gum solution by dividing the yield stress with the corresponding shear rate, $\dot{\gamma}_0$, i.e., $\mu_0 = \frac{\tau_y}{\dot{\gamma}_0}$ and is tabulated below:

Table 5.3: Calculated values of yielding viscosity for 0.5wt%, 1.0wt% and 1.5wt% xanthan gum solutions

Concentration (wt %)	μ_0 [Pa.s]
0.5	13.30
1.0	22.61
1.5	32.36

Profiles of the molecular viscosity as calculated in Mixsim (using Equation (5.2)) for each rotational speed of the marine propeller and pitched blade turbine impeller is shown below:

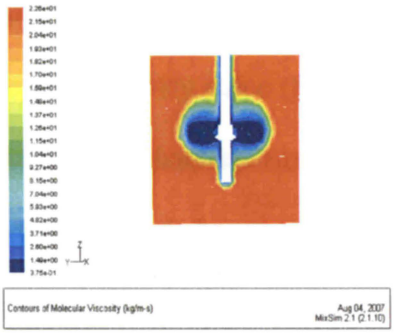

50rpm

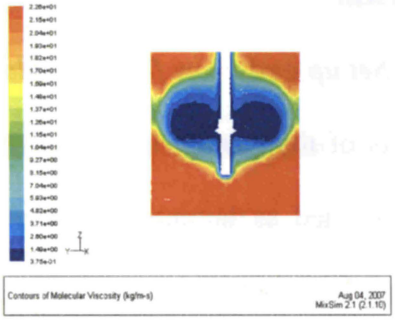

100rpm

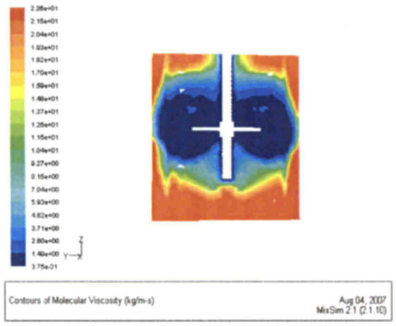

150rpm

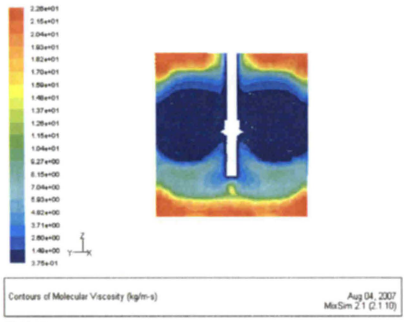

200rpm

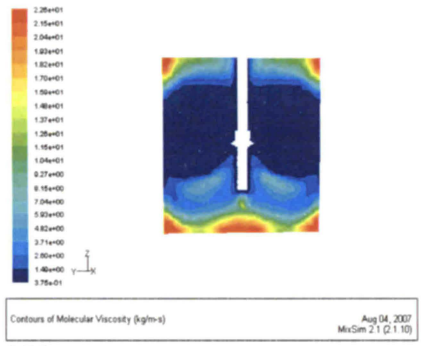

250rpm

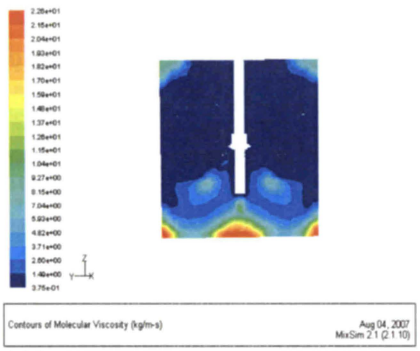

300rpm

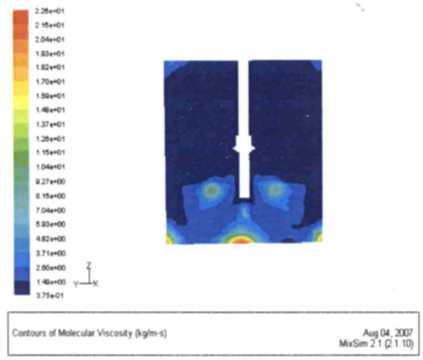

350rpm

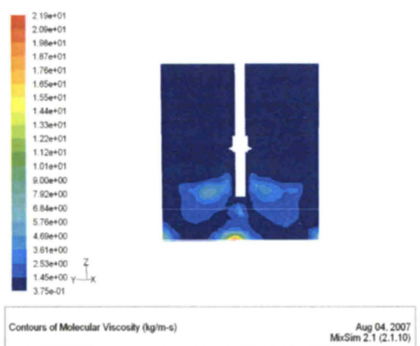

400rpm

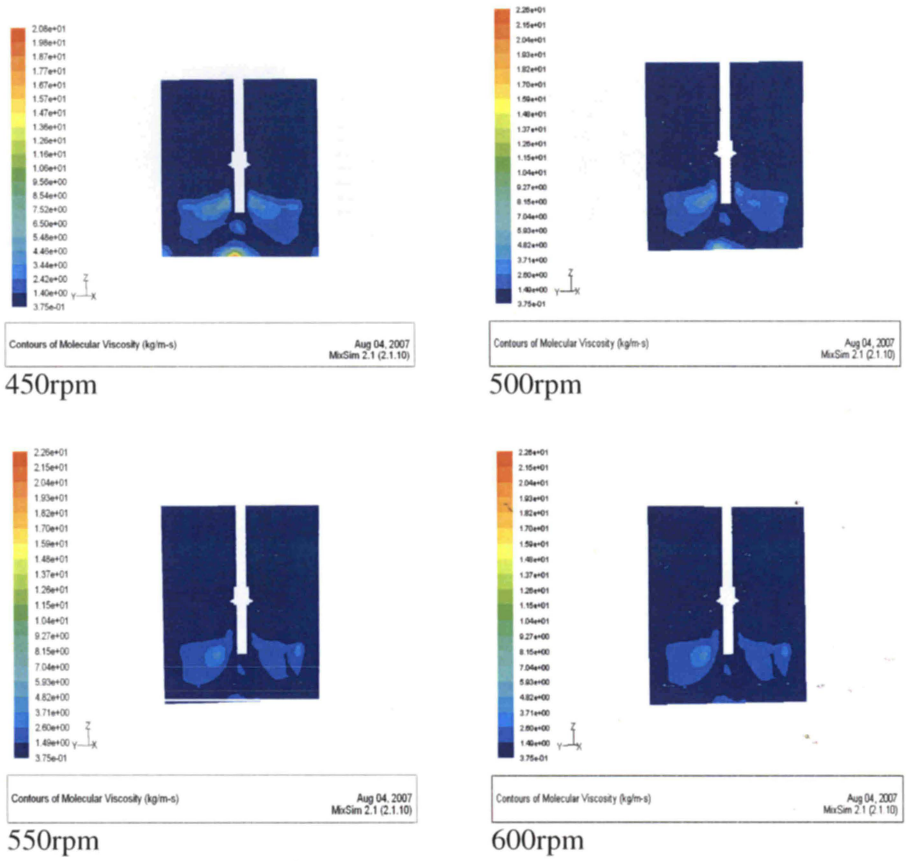

Figure 5.3 Profiles of Molecular viscosity calculated using the Hershel Bulkley rheological model for the Pitched Blade Turbine impeller mixing 1% xanthan gum at C3 = 20cm

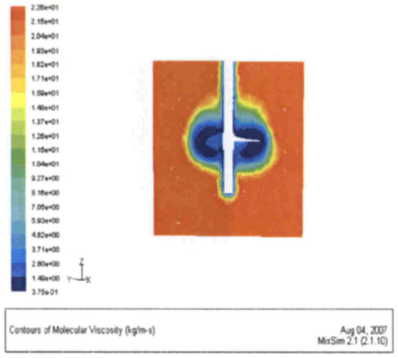

50rpm

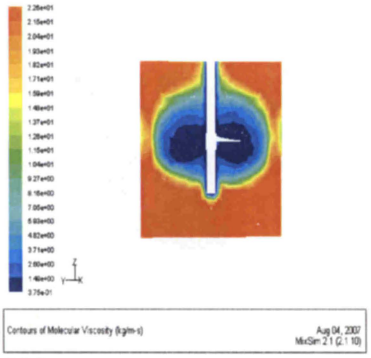

100rpm

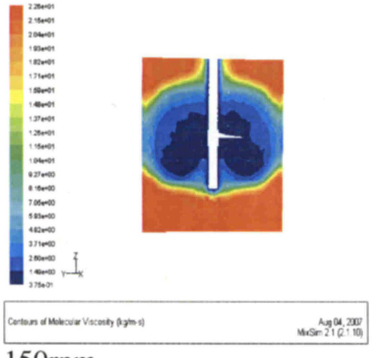

150rpm

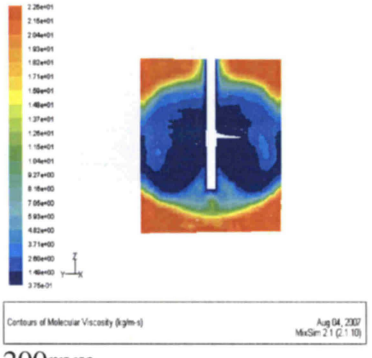

200rpm

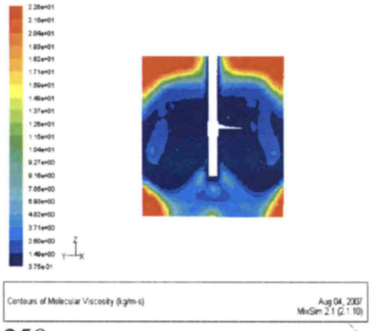

250rpm

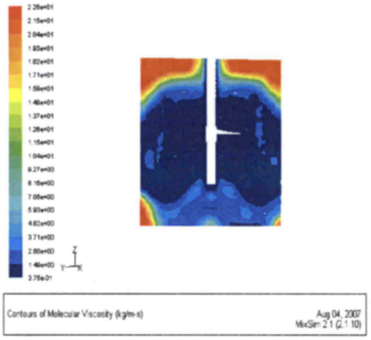

300rpm

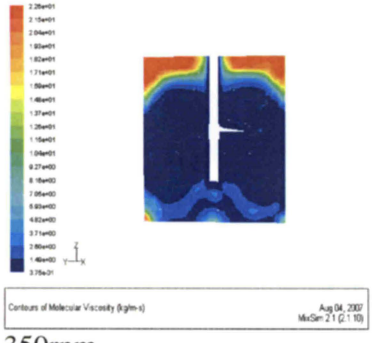

350rpm

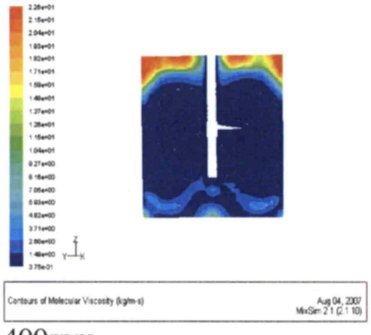

400rpm

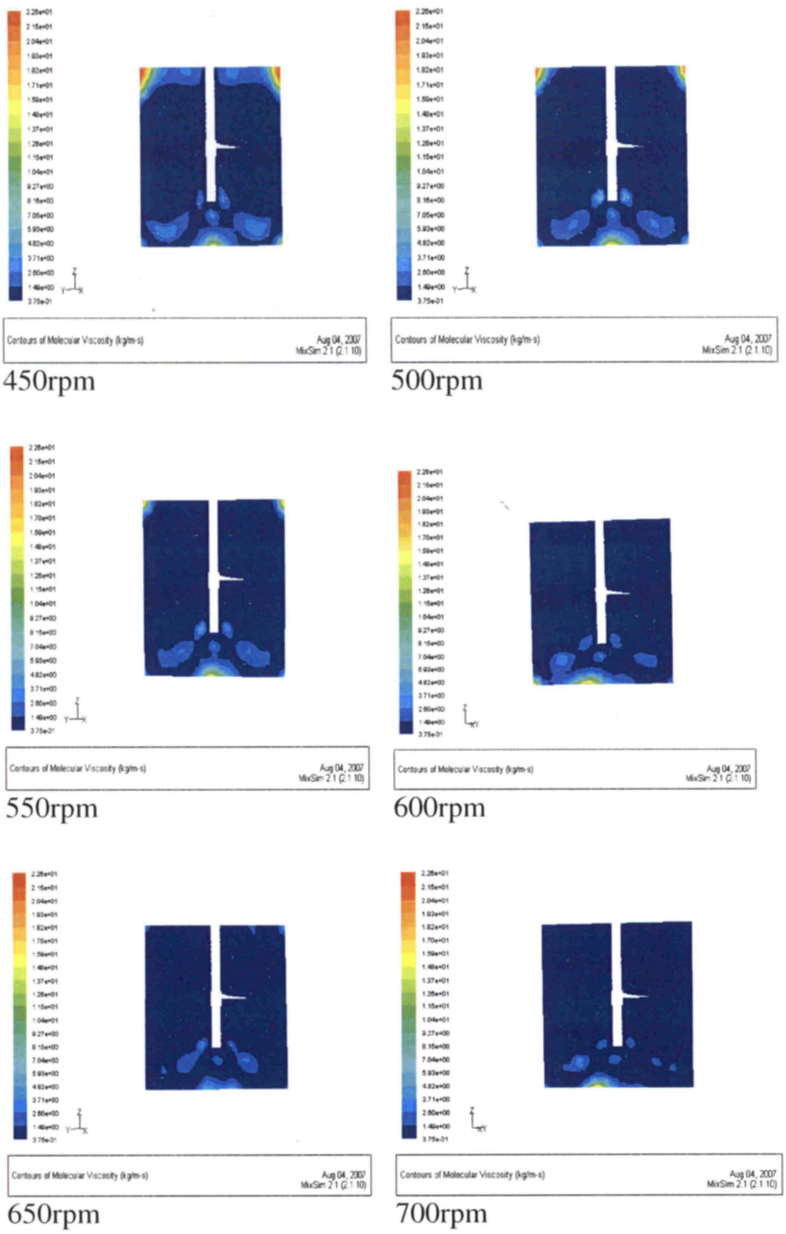

Figure 5.4 Profiles of Molecular viscosity calculated using the Herschel Bulkley rheological model for the Marine Propeller mixing 1% xanthan gum at C3 = 20cm

From Figures 5.3 and 5.4, it can be seen that at low impeller rotational speeds, the fluid viscosity is high except for the regions in the immediate vicinity of the impeller blades where the viscosity

is low. However, as the impeller rotational speed is increased, the fluid viscosity even close to the vessel walls is reduced.

The measured density was imputed into the software as a constant density. Once the model and fluid properties had been specified, automatic grid generation was initiated.

A decision on the number of cells to be employed in the grid generation step was made by carrying out grid independence studies. As described earlier, successive grid refinements were conducted, and the change in the axial velocity below the impeller (a region of large velocity gradients) in the radial direction was determined. This change in axial velocity was quantified using the Root Mean Square (RMS) deviation given by:

$$RMS = \frac{\left[\frac{1}{n}\sum_{1}^{n}(u_1 - u_2)^2\right]^{1/2}}{\left[\frac{1}{n}\sum_{1}^{n}u_2^{\,2}\right]^{1/2}} \qquad (5.3)$$

Where u_1 and u_2 are the axial velocities at the same radial position of the two grid sizes being compared and n refers to the total number of axial velocities obtained at each radial position.

Starting with a cell count of 139017 and almost doubling the number of cells to 262232, the root mean square RMS deviation of the axial velocity between the two grid sizes was about 2.2%.

The grid size was then doubled again to 509577 cells and the root mean square deviation of the axial velocity compared to the grid size of 262232 cells was 1.84%. Since the deviation was deemed to be insignificant, the medium grid size of 262232 was chosen to reduce computational requirements. The same procedure was repeated for simulations involving the marine propeller (267912 cells were used in this case).

Figure 5.5 shows the axial velocity profile obtained at the three successive grid refinements.

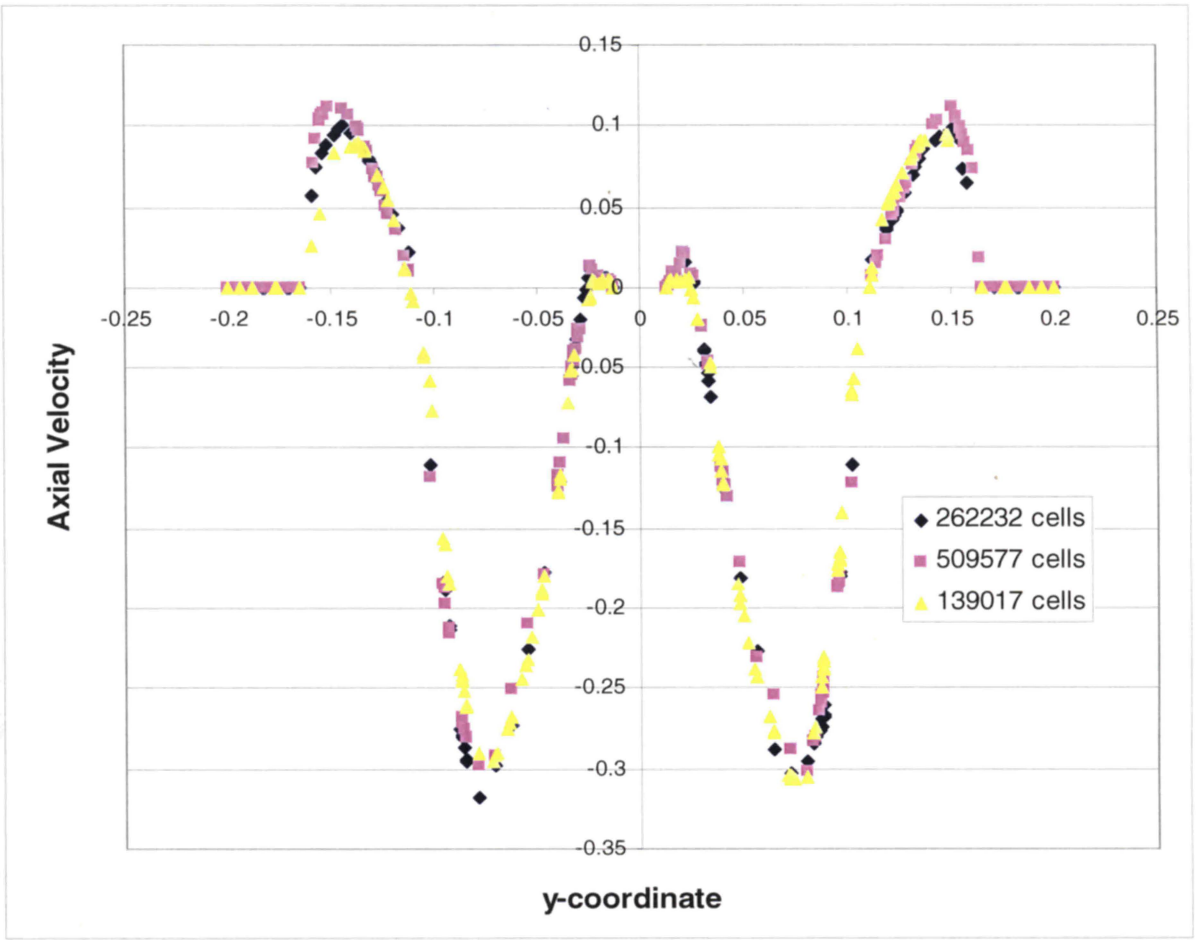

Figure 5.5 Results of Grid Independence Studies on Pitched Blade Turbine Impeller

The vessels and internals meshed with 262232 cells according to the results of the grid independence study is shown in Figure 5.6

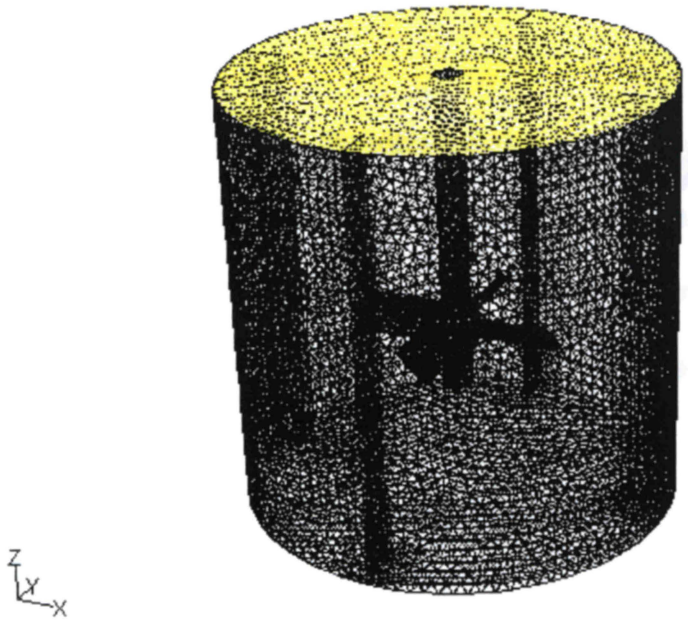

Figure 5.6: Typical Grid generated automatically by MixSim 2.1

Once a decision had been made on the grid size, the differential equations governing the flow field were discretized using the power law and second order discretization schemes for momentum and pressure respectively. The SIMPLEC solution algorithm was utilized to take into account the pressure-velocity coupling in solving the flow field. The flow field was considered to be solved (converged) when the residuals of the continuity equation fell below 10^{-3} and those of the momentum equation fell below 10^{-5} as depicted in Figure 5.7.

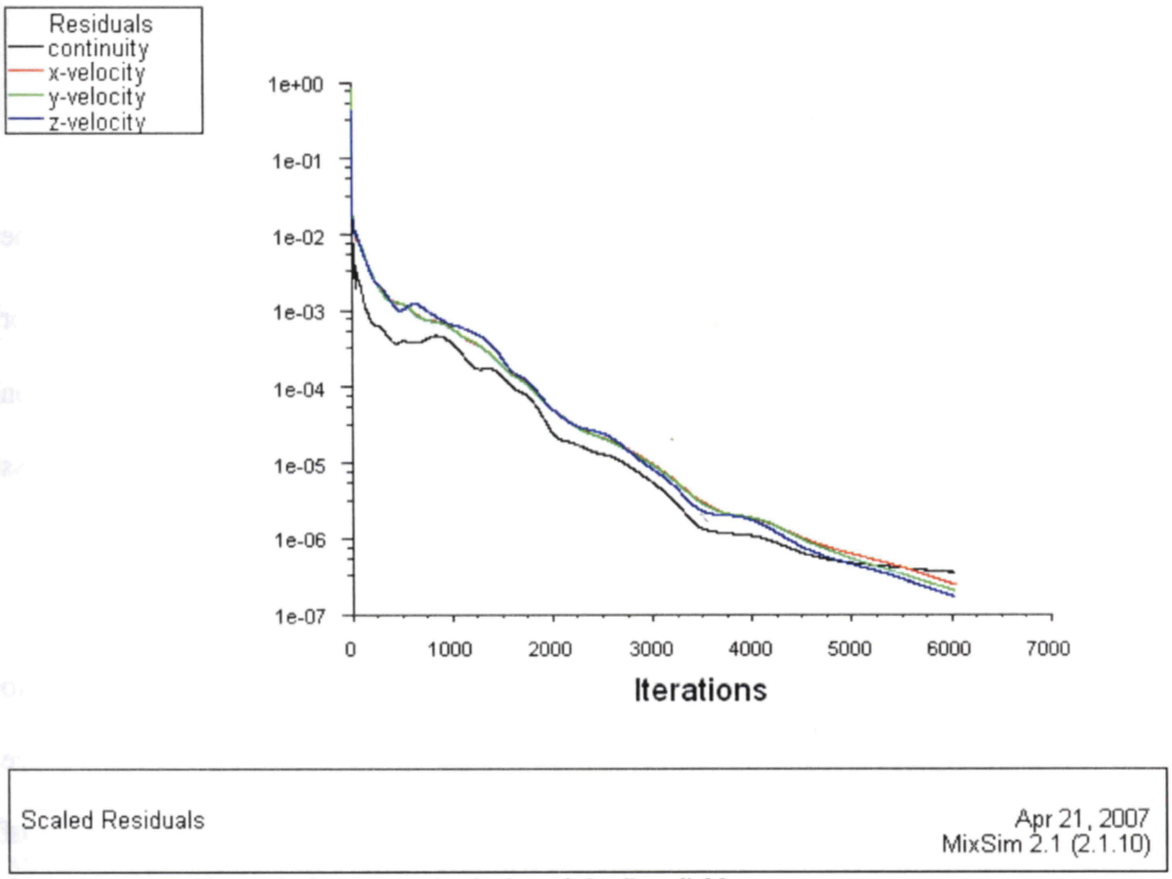

Figure 5.7: Plot of a typical converged solution of the flow field

A typical run required approximately 6000 iterations for complete convergence representing approximately 5hrs of CPU time.

The flow field was then transported to FLUENT for mixing time simulations.

5.2.2 Mixing Time Simulations

Mixing time simulations were conducted by simulating the unsteady state transport of a non reacting tracer in the numerically calculated flow field.

$$\frac{\partial}{\partial t}(\rho m_l) + div(\rho u m_l) = div(\Gamma_l \; grad \quad m_l) \tag{5.4}$$

where m_l is the mass fraction of the tracer species, u is the mean velocity vector and Γ_l is the molecular diffusivity. The molecular diffusivity was taken to be 10^{-9} m^2/s, a typical value for liquids even though this value was found to have a negligible effect on the tracer distribution possibly because the contribution of molecular diffusion to the overall tracer dispersion process is negligible (Montante *et al.*, 2005).

Once the model had been transported to Fluent and the unsteady state solver was specified to monitor the tracer species concentration as a function of time in the flow field. In accordance with the experimental procedure, the tracer species was defined with properties similar to that of the bulk material.

To add the defined tracer material to the flow field, a few cells were marked in the fluid domain and to these cells, tracer material was added (patched). To monitor the evolution of the tracer species, 7 monitoring positions (analogous to probes in the experiment) including one monitoring point at tracer addition point were defined (Figure 5.8).

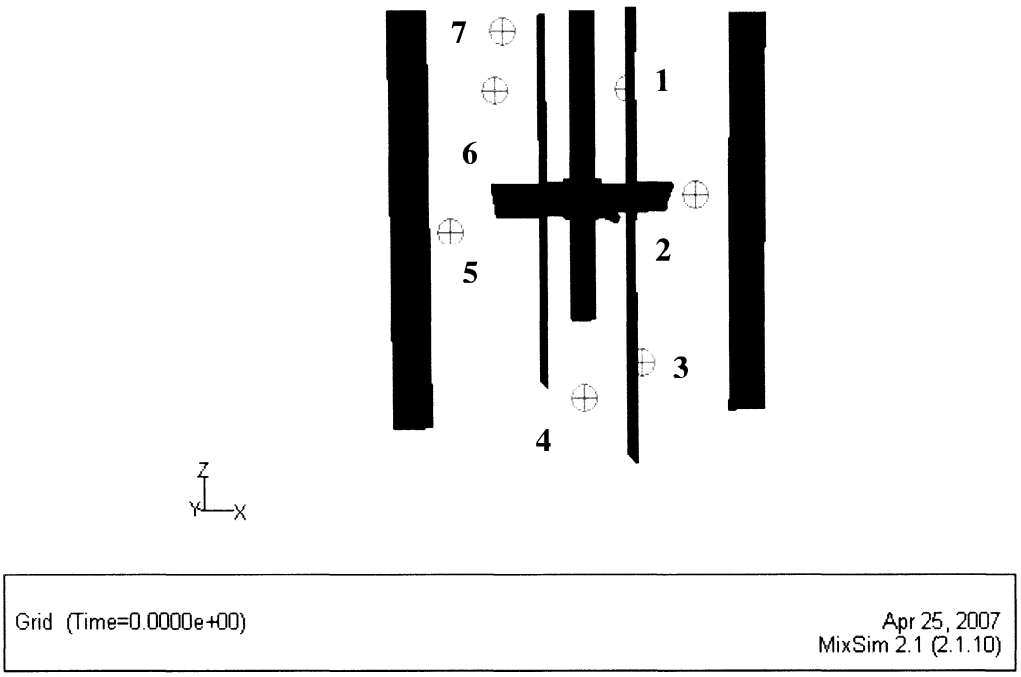

Figure 5.8: Monitoring points used to monitor the time evolution of tracer concentration. Monitoring point at locations (x,y,z): Location 1 (0.07, 0.08,0.30); Location 2 (-0.15, -0.10, 0.19); Location 3 (0.06, 0, 0.05); Location 4 (0, 0, 0.02); Location 5 (0.15, 0.1, 0.2); Location 6 (-0.07, 0.08, 0.30); Location 7 (-0.1, -0.1, 0.36)

Solution of the transport of tracer species in the flow field was carried out in a frozen flow field, i.e., the solver for momentum transfer was turned off. The mixing time simulations were run using a time step size of 0.1s for 4000 iterations and considered to be converged when the residuals fell below 10^{-7} and the plots of normalized tracer concentration profile at each of the monitoring points were generally flat. The mixing time was obtained by combining the normalized tracer distribution (normalized with the tracer concentration at equilibrium) at each of the monitoring points on a single graph and taken to be the time when the normalized tracer concentration at each of the monitoring locations simultaneously reached within 98% of the steady state value (Figure 5.9).

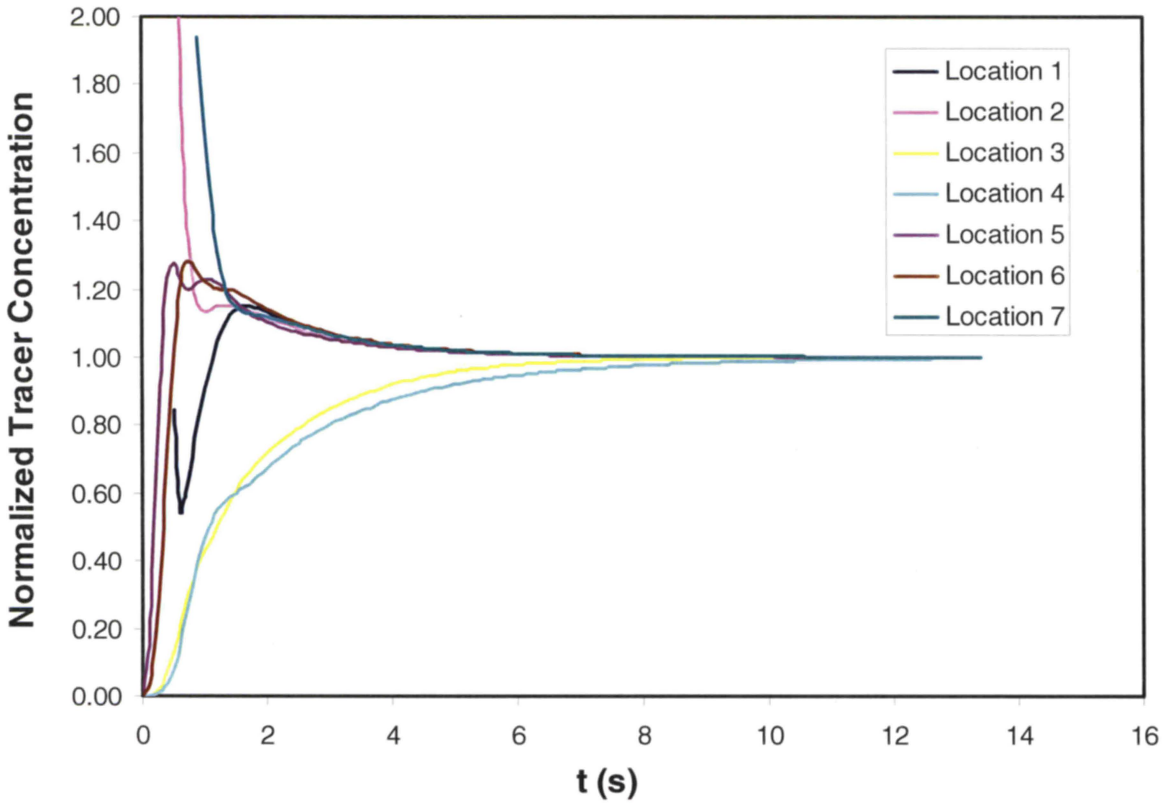

Figure 5.9: Normalized tracer concentration profiles at 7 monitoring points for mixing time evaluation showing PBT rotating at N= 500rpm mixing 1% xanthan gum solution at C3 = 20cm

6 Results and Discussion

6.1 Power Consumption Results

The power consumed by the pitched blade turbine in mixing 0.5 wt%, 1.5t% and 1.5wt% xanthan gum solutions was obtained experimentally and via CFD. For these results, the clearance of the impeller from the bottom of the tank was kept constant at C1 = 13.5cm. It was observed that regardless of the concentration of xanthan gum under consideration, the power consumption increased as the impeller rotational speed increased as depicted by Figures 6.1a-c. This result was also observed for CFD.

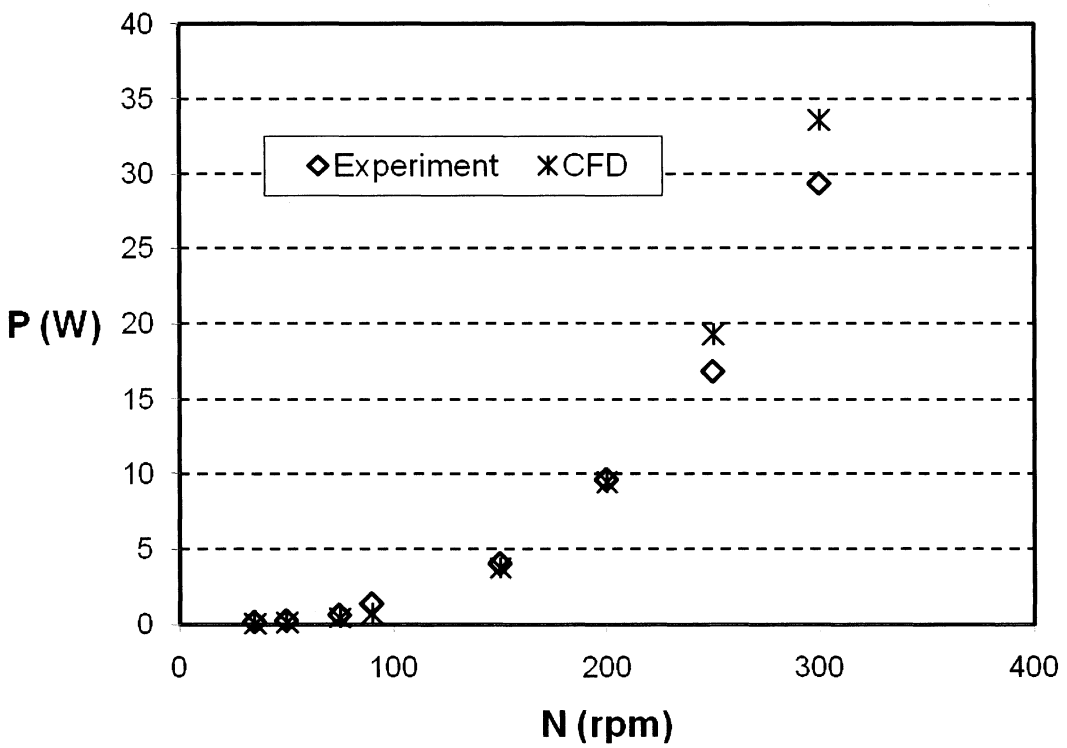

Figure 6.1a: Plot of Power Consumption vs. Impeller rotational speed for PBT mixing 0.5% xanthan gum at C1 = 13.5cm

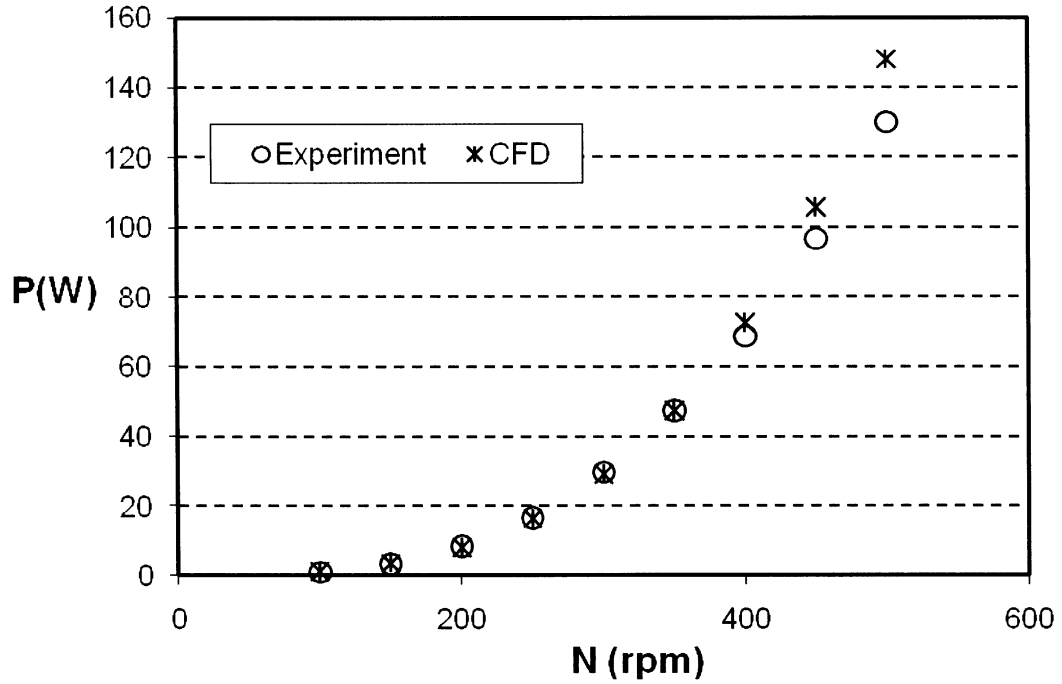

Figure 6.1b: Plot of Power Consumption vs. Impeller rotational speed for the PBT mixing 1.0% xanthan gum at C1 = 13.5cm

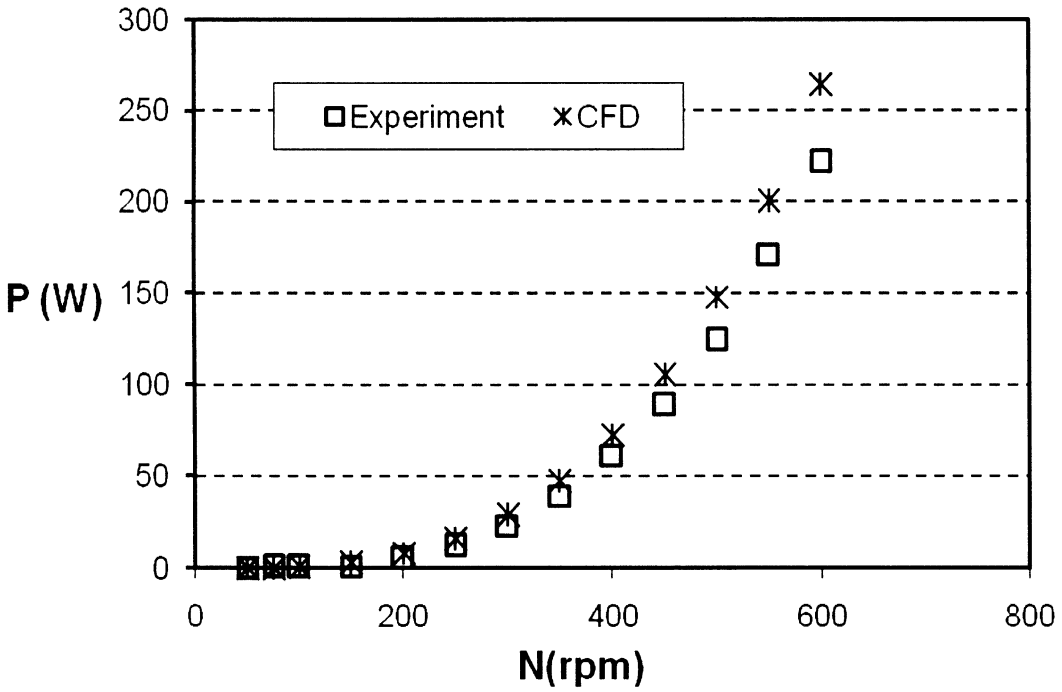

Figure 6.1c: Plot of Power Consumption vs. Impeller rotational speed for the PBT mixing 1.5% xanthan gum at C1 = 13.5cm

As may be seen from these curves, the numerical results are in good agreement with the experimental power consumption results.

There is a slight deviation at higher rotational speeds (for $Re_a > 400$) shown in Figure 6.2 which represents a plot of dimensionless power consumption (power number) versus Re_a.

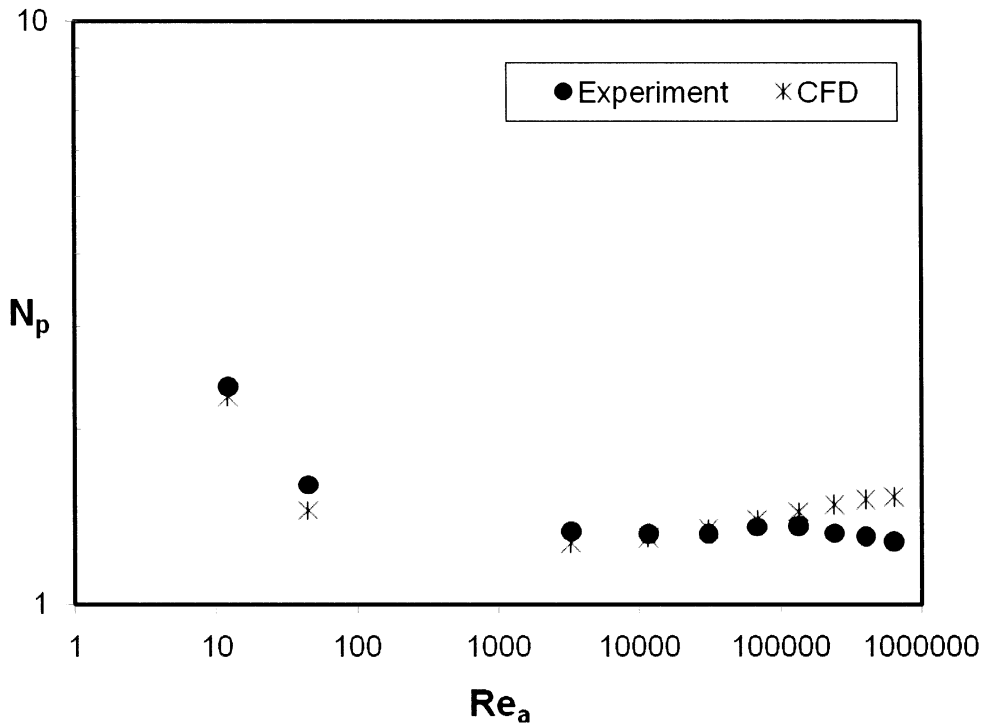

Figure 6.2: Power Curve for the PBT mixing 1.0% xanthan gum solution at C1 = 13.5cm showing the extent of the laminar flow regime

Figure 6.2 clearly shows that as the Re_a number is increased beyond that for the laminar flow regime, the deviation between the experimental and CFD results grow. It also shows that the laminar flow model is adequate for a portion of the transitional flow regime (up to $Re_a = 400$). However, the use of the laminar flow model for the transitional flow regime is a common practice in numerical modeling of stirred tanks (for e.g., Kelly and Gigas, 2003). In fact in the

documentation for the Fluent software package, the non Newtonian fluid flow was modeled as laminar even though the flow regime in the mixing tank was transitional (Fluent Inc., 2006) implying that the manufacturers of FLUENT endorse the use of the laminar flow model in the transitional regime.

The flow regime has implications on whether or not the Metzner and Otto equation can be used since it is only valid in the laminar regime. For the purpose of this work, since the flow field was modeled as laminar, the Metzner and Otto equation was used to correlate the power data.

The effect of PBT impeller clearance position on the mixing performance was also studied (Figures 6.1b, 6.3a-b). Again, the experimental and numerical results power consumption results were in good agreement except at higher impeller rotational speeds where the deviation becomes significant as noted previously.

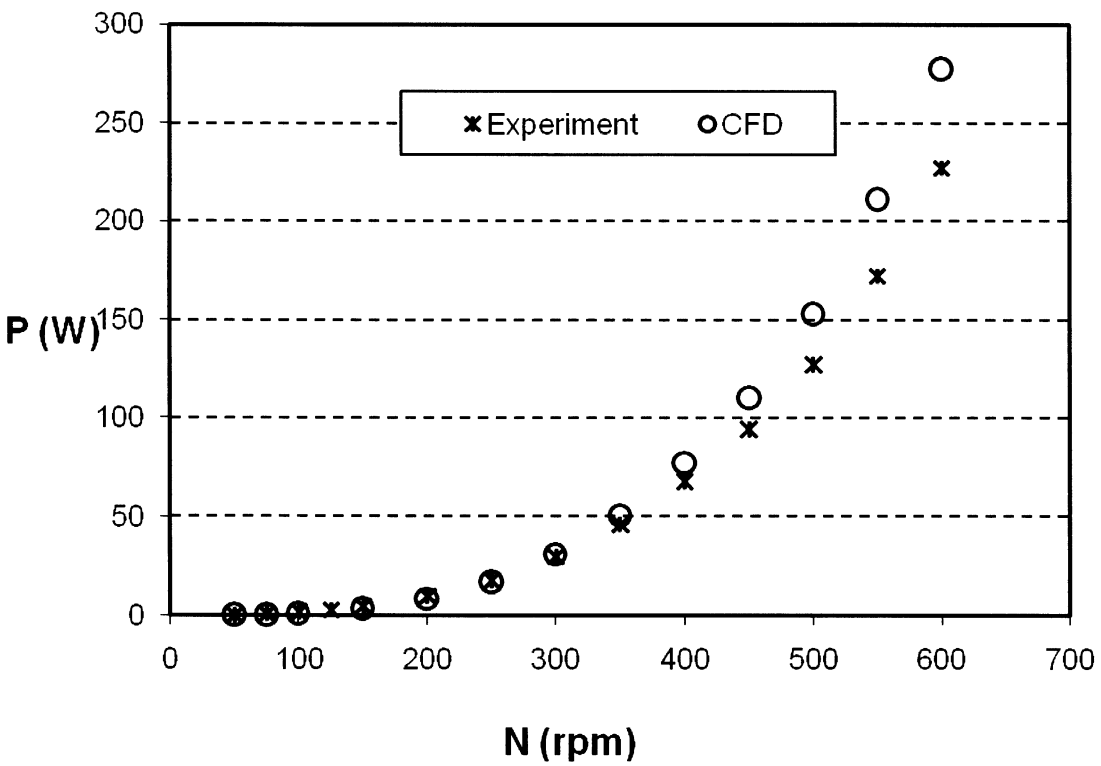

Figure 6.3a: Plot of Power Consumption vs. Impeller rotational speed for PBT mixing 1.0% xanthan gum solution at C2 = 16cm

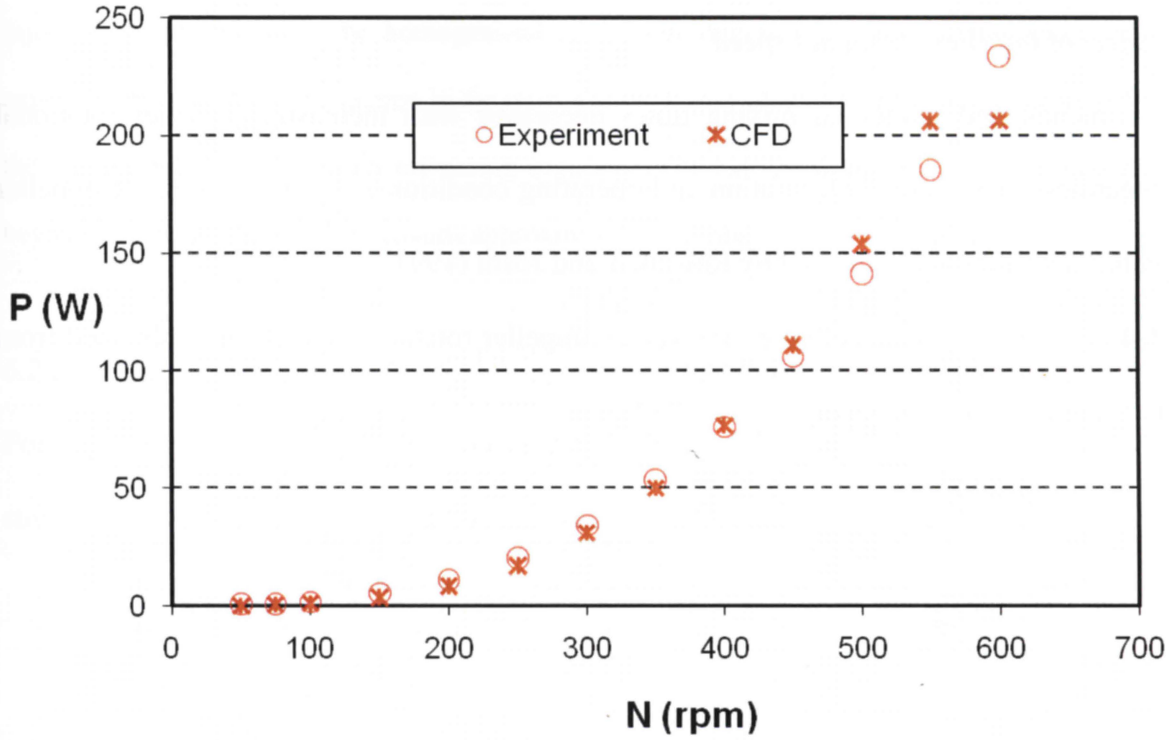

Figure 6.3b: Plot of Power Consumption vs. Impeller rotational speed for PBT mixing 1.0% xanthan gum solution at C3 = 20cm

Based on the comparison of experimental and numerical power consumption results, the numerical results are validated and the CFD tool can be considered to have exhibited the capability to successfully predict the mixing performance of the mixing system. Therefore, the numerical mixing time results can be presented with a reasonable degree of confidence and compared to experimental mixing times.

6.2 Mixing Time Results

6.2.1 Effect of Impeller rotational speed

The experimental and numerical mixing times decreased with increasing impeller rotational speed, regardless of system configuration and operating conditions. A similar effect of impeller speed on mixing times was observed by Rewatkar and Joshi (1991).

Figure 6.4 represents a typical mixing time versus impeller rotational speed curve obtained from the numerical predictions of mixing time.

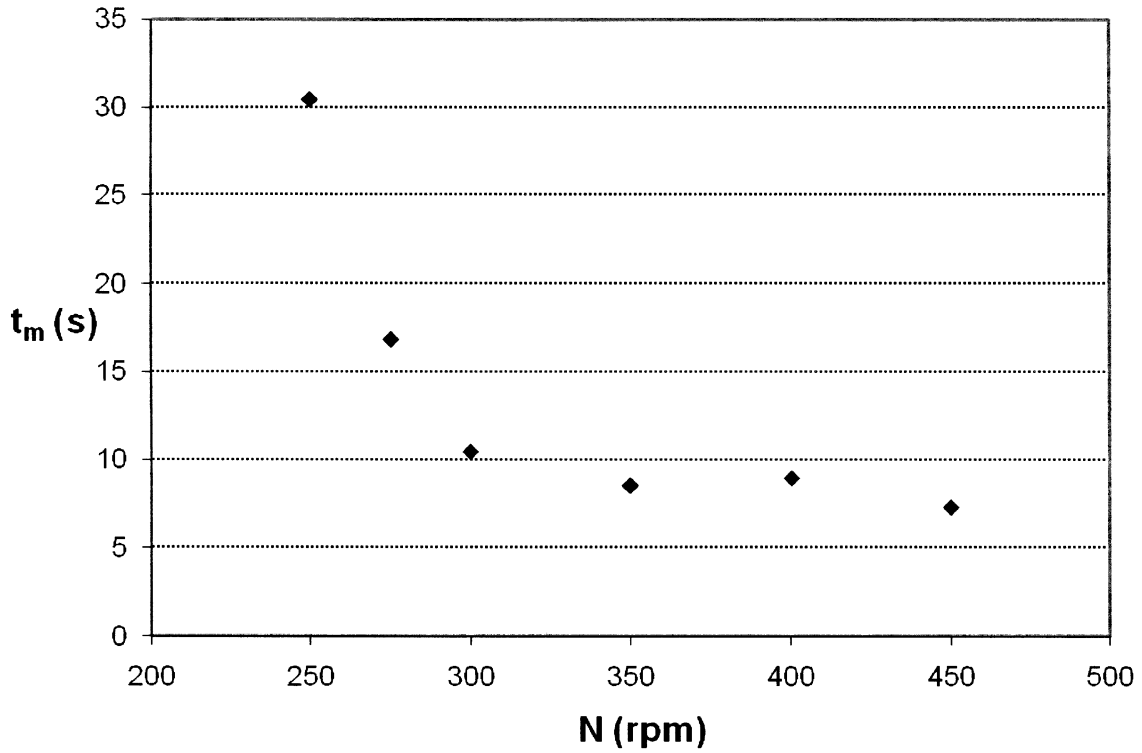

Figure 6.4: Typical curve obtained from CFD mixing time predictions showing the relationship between mixing time and impeller rotational speed. Represents case of PBT mixing 1.5% xanthan gum solution at C1 = 13.5cm

The experimental mixing time results were also found to decrease with increasing impeller rotational speed. The observed trend from both the experiments and CFD tool is in agreement with what is expected

intuitively, because as the impeller speed is increased, the Re number increases as well, causing a tracer injected into the vessel to be homogenized at a faster rate with the rest of the vessel contents. As expected, this causes in a reduction in the mixing time. It may also be deduced from Figure 6.4 that while the mixing time decreases with increasing impeller rotational speed, there is a certain maximum speed beyond which the mixing time remains approximately constant.

6.2.2 Effect of yield stress

For a given power input, as the concentration of xanthan gum was increased, the fluid yield stress increased causing an increase in the mixing time as shown in Figure 6.5

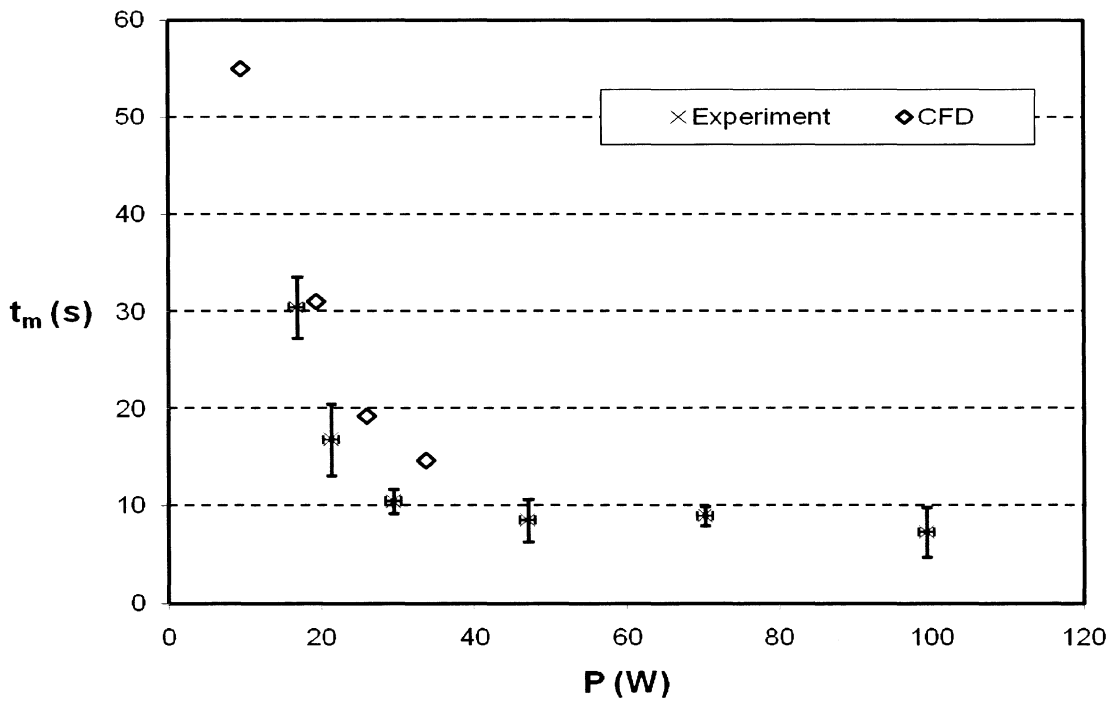

Figure 6.5a: Effect of yield stress on the mixing time for PBT mixing 0.5% xanthan gum solution at C1 = 13.5cm

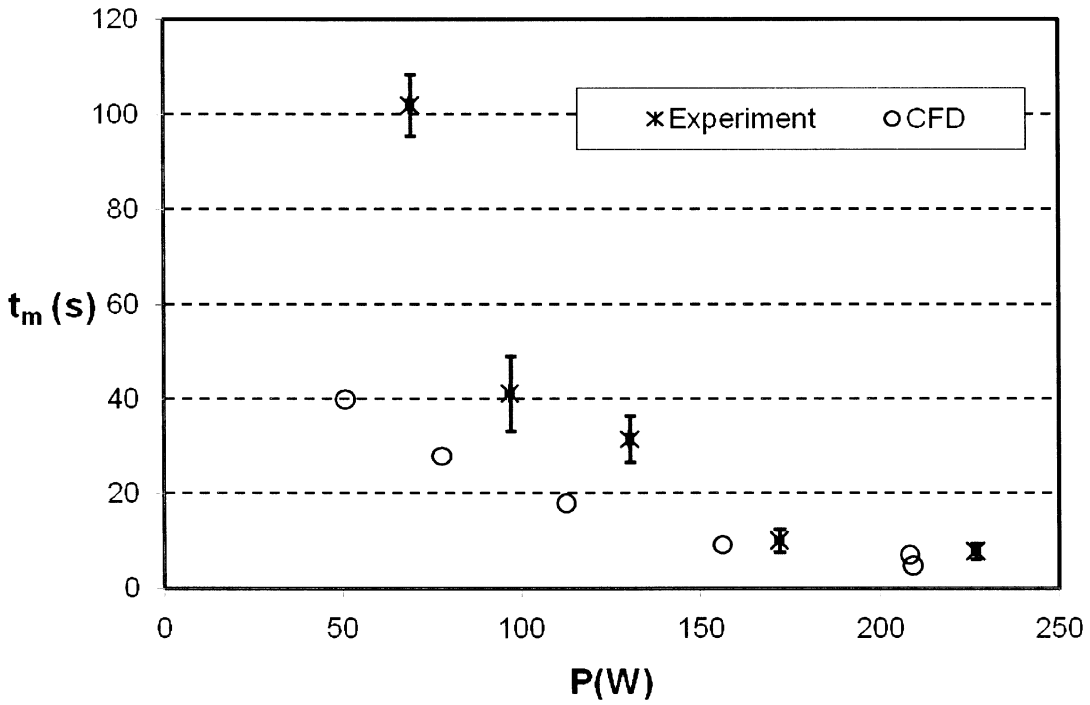

Figure 6.5b: Experimental and CFD study of effect of yield stress on the mixing time for PBT mixing 1.0% xanthan gum solution at C1 = 13.5cm

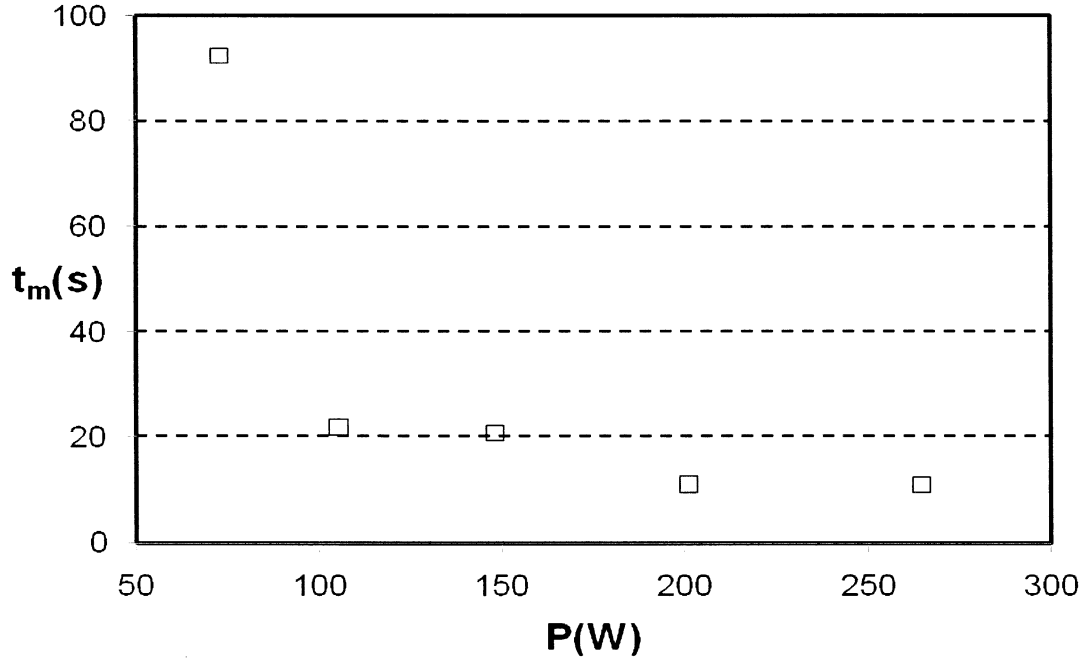

Figure 6.5c: CFD study of effect of yield stress on the mixing time for PBT mixing 1.5% xanthan gum solution at C1 = 13.5cm

A plausible explanation for this observation is that as the yield stress of the solutions increases for a given power input, low velocity conditions exist in a larger portion of the fluid in the tank resulting in an increase in the time required to reach homogeneity. This observation was found to hold true regardless of whether the experimental or numerical mixing times were considered as can also be deduced from Figures 6.5a-c.

6.2.3 Effect of Impeller clearance

The effect of impeller clearance from the vessel bottom was studied using the PBT impeller for the clearances ranging from 13.5cm to 20cm. The decision to study this range of clearances was made based on the knowledge that placing the impeller too low would result in most of the fluid remaining unmixed, while operating at an impeller clearances higher than half of the fluid height causes surface aeration even at low impeller rotational speeds. The impeller pumping capacity is reduced as result giving rise to longer mixing times as observed by Rewatkar and Joshi (1991).

Figures 6.6a-c show that as the clearance of the impeller was increased from 13.5cm to 20cm, the mixing time decreased. This result is identical to that obtained by Rewatkar and Joshi (1991); Patwardhan and Joshi (1999) and Houcine *et al.* (2000), who observed a reduction in the mixing time with increasing impeller clearance for the pitched blade downflow turbine. It should be noted that comparison with the results for the downflow turbine is valid because the pumping direction of the PBT used in simulation and experiments was the downward pumping direction. However, the numerical results do not predict the same effect of impeller clearance on the mixing times. According to the CFD results, the mixing time increases as the impeller clearance increases (Figures 6.6a-c).

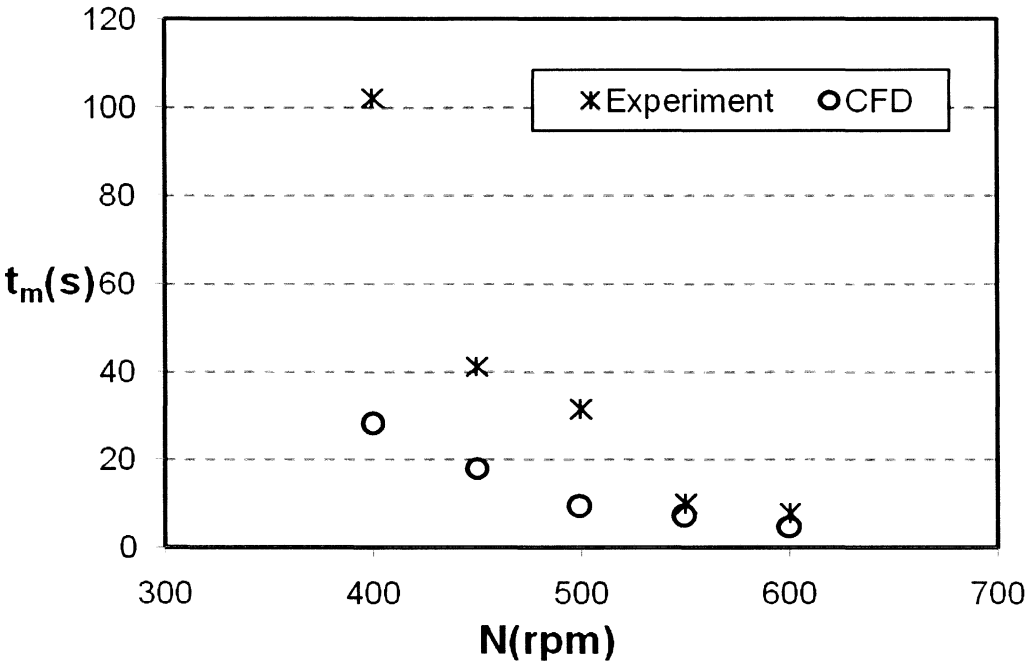

Figure 6.6a: Effect of clearance on the mixing time for PBT mixing 1.0% xanthan gum solution at C1 = 13.5cm

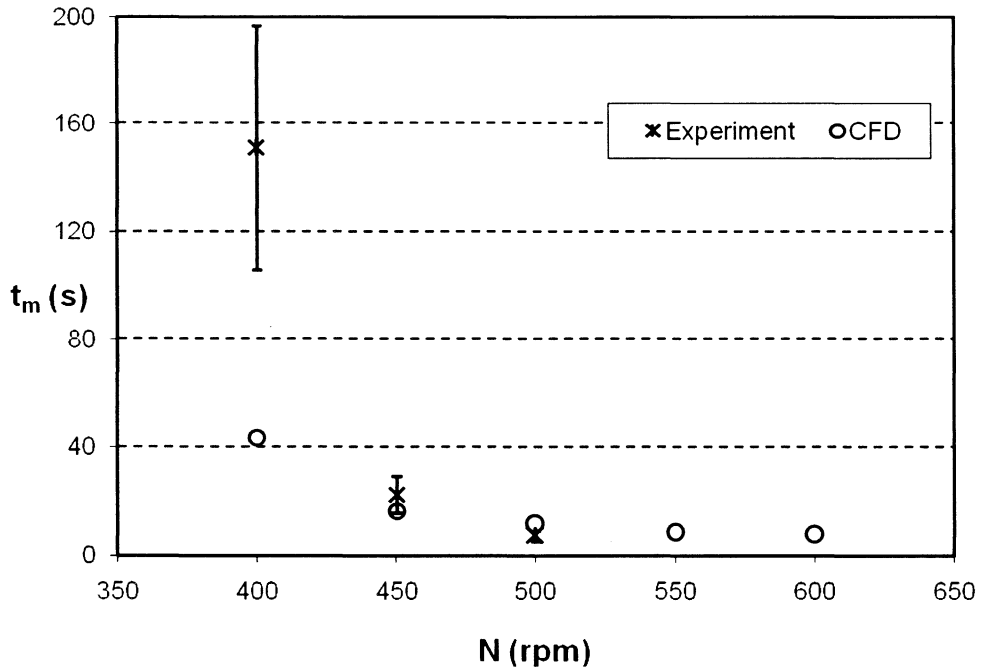

Figure 6.6b: Effect of clearance on the mixing time for PBT mixing 1.0% xanthan gum solution at C3 = 20cm

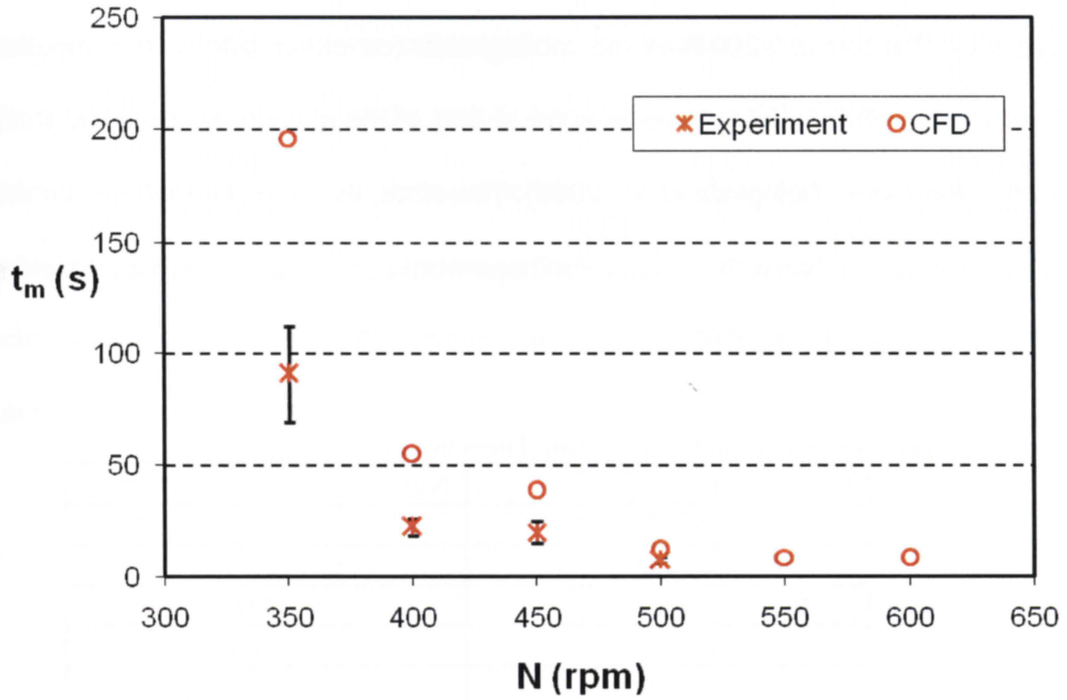

Figure 6.6c: Effect of clearance on the mixing time for PBT mixing 1.0% xanthan gum solution at C3 = 20cm

The source of the discrepancy between the numerical and experimental results of the effect of impeller clearance on the mixing time can be arrived at by observing that CFD either over predicts or under predicts the experimental mixing times (depending on the impeller clearance) especially at impeller rotational speeds below 500rpm.

The discrepancy between experimental and numerical mixing times has recently been the subject of much of the mixing literature (Table 6.1). According to these results, numerical mixing times that are 2-3 times the experimental value have been reported. The common reason cited for these deviations is that current CFD codes are unable to accurately predict the mass exchange between different circulation loops in the stirred tank (Montante *et al.*, 2005; Bujalski *et al.*, 2002b; Jaworski *et al.*, 2000). The correct prediction of this mass exchange is necessary for accurate

mixing time predictions. A relationship between the results obtained in literature and those of this work can be established by noting that the pitched blade turbine generates two circulation loops or compartments (Paul *et al.*, 2004) in the mixing tank (on either side of the impeller shaft). The controlling step of the mixing process is the ability of the impeller to distribute fluid between these circulation loops (Delaplace *et al.*, 2000). Therefore, the correct simulation of the distribution of tracer material between the circulation loops would give accurate mixing times, a requirement that is not achieved by the CFD code.

Table 6.1 Comparison of Experimental and Numerical Mixing Times in Literature

Author	Experimental t_m (s)		Numerical t_m (s)
Osman and Varley, 1999*	N (rpm) = 300		
	17.0		15.7
	26.5		43.0
	12.8		22.1
	25.6		38.8
	26.5		38.1
	37.3		50.3
	34.5		45.0
Jaworski *et al.*, 2000	N (rpm)	t_m (s)	
	75	32.56	97.2
	100	26.28	71.7
	150	16.88	52.6
Kukukova *et al.*, 2005	N (rpm) = 150		
	8.4		4.6
Bujalski *et al.*, 2002*	N (rpm) = 100		
	43.9		102.7
	43.8		102.7
	21.4		68.2
	46.6		99.7
	46.7		99.5
	48.9		105.7

*For the same impeller rotational speed, measurements were conducted at different regions in the mixing tank

6.2.4 *Effect of Impeller design*

A comparison of mixing performance of the PBT, marine propeller and A320 impellers is made on the basis of equal power consumption. In order to accomplish this, the clearance of the impeller from the bottom of the tank is kept constant at C3 = 20cm. The decision to study the mixing performance of the three impellers at this clearance was made based on the results obtained from the previous section where it was experimentally observed that increasing clearance gave lower mixing times, and that this experimental finding was in excellent agreement with the work of previous researchers.

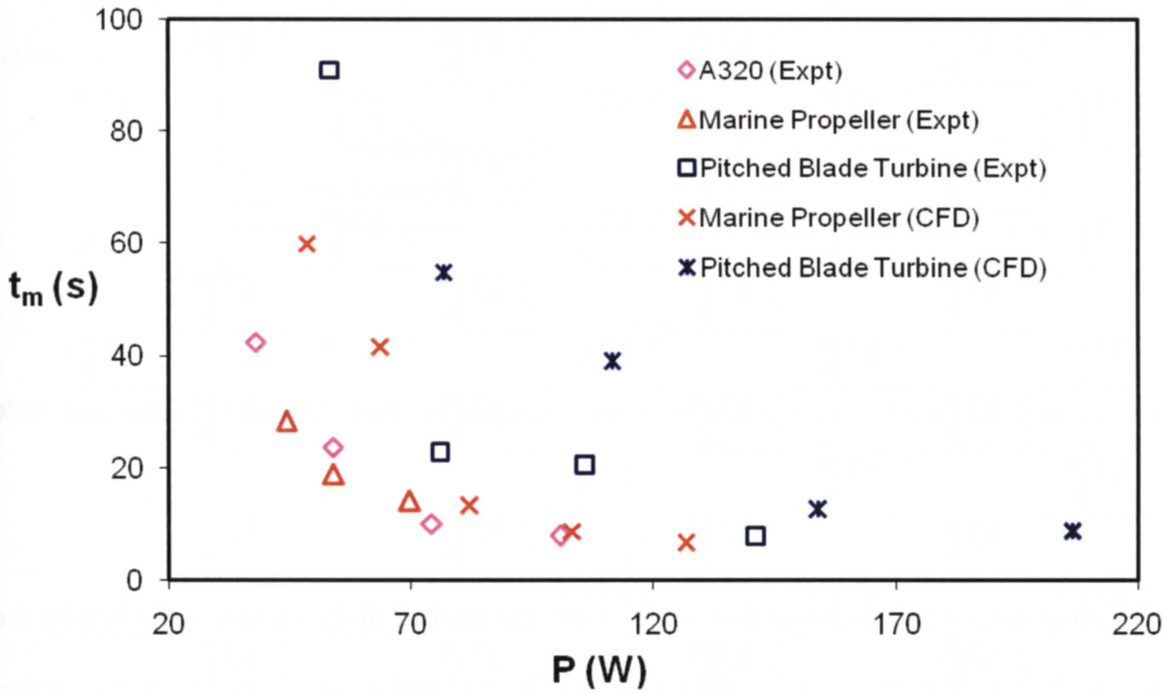

Figure 6.7: Comparison of the PBT, Marine Propeller and A320 Impeller mixing 1.0% xanthan gum at C3 = 20cm on the basis of equal power consumption

From Figure 6.7, it can be observed that for a given power input, the A320 impeller and the marine propeller achieve homogenization in the shortest time. This observation was also borne

out by the numerical results. The CFD results predict that the pitched blade turbine gives longer mixing times compared to the marine propeller at a specific power input.

In order to check the results presented in Figure 6.7, a plot of the mixing time number over the entire flow regime was generated (Figure 6.8).

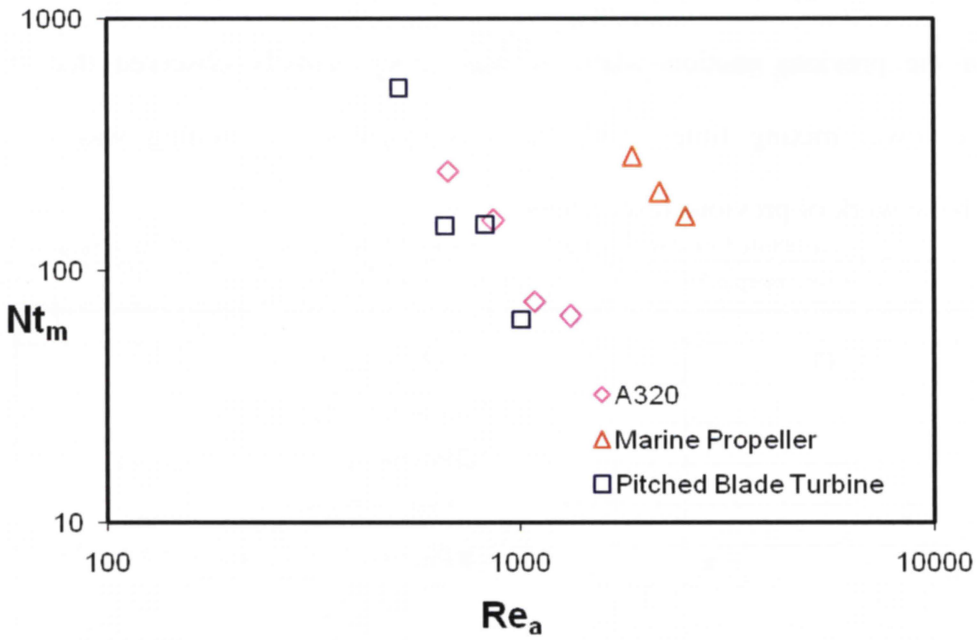

Figure 6.8: Mixing time number vs. apparent Reynolds Number for PBT, Marine Propeller and A320 Impeller mixing 1.0% xanthan gum at C3 = 20cm

It shows that the homogenization number is lowest for the pitched blade turbine, followed by the A320 impeller and then the Marine Propeller. From the definition of the homogenization number, it can be concluded that because the mixing time number for the PBT is the lowest of the three impellers, it requires less revolutions than the other impellers to achieve the desired degree of mixing, followed closely by the Lightnin A320 impeller. Therefore, the PBT impeller may be more efficient than the other impellers for mixing of yield stress fluids. The conclusions arrived at from Figure 6.7 are quite different from those from Figure 6.8, which seems to suggest

that a comparison of the impellers on the basis of equal power consumption alone may not be sufficient to determine the most efficient impeller.

6.3 Impeller Efficiency

In order to confirm the findings of the previous section, the homogenization efficiency of the three impellers was evaluated using the following criterion:

$$\frac{Pt_m^{\ 2}}{\mu_a D^3} = f''\left(\frac{D^2\rho}{\mu_a t_m}\right) \tag{6.1}$$

The dimensionless groups in Equation (6.1) were evaluated using the following dimensionless quantities:

$$\frac{Pt_m^{\ 2}}{\mu_a D^3} = N_p \,\mathrm{Re}_a (Nt_m)^2 \left(\frac{D}{T}\right)^3 \tag{6.2}$$

$$\left(\frac{D^2\rho}{\mu_a t_m}\right) = \mathrm{Re}_a (Nt_m)^{-1} \left(\frac{D}{T}\right)^2 \tag{6.3}$$

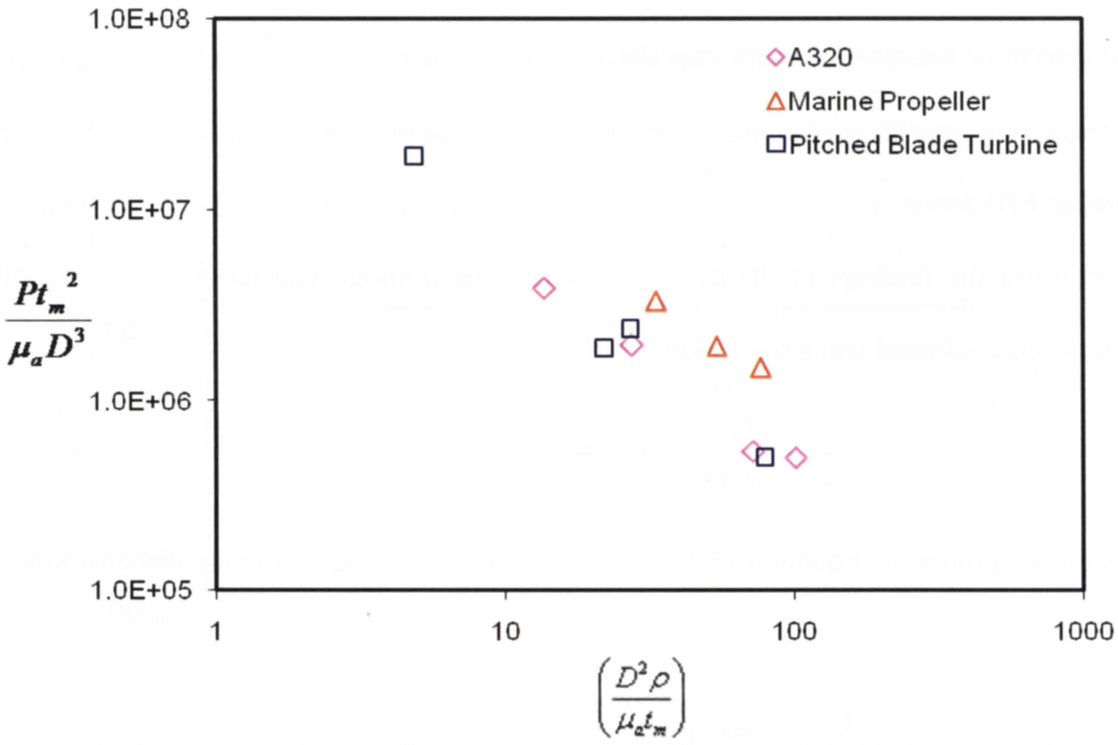

Figure 6.9: Plot of performance rating vs. mixing time number for PBT, Marine Propeller and A320 Impeller mixing 1.0% xanthan gum at C3 = 20cm

The expression on the left hand side of Equation (6.2) is proportional to energy divided by the volumetric performance of the mixing equipment, and is referred to as the performance rating (Tatterson, 1991), while the expression on the right hand side allows a decision to be made on which agitator exhibits the lowest specific power consumption in mixing a given fluid in a vessel of a given volume and required mixing intensity and is referred to as the mixing time Reynolds number (Novak and Rieger, 1975; Rieger *et al.*, 1986; Shiue and Wong, 1984).

From these results (Figure 6.9), it can be seen that the pitched blade turbine has the highest homogenization efficiency because it has the lowest performance rating over the entire flow regime. This result is in agreement with that of Shuie and Wong (1984) who found the pitched blade turbine to have a lower performance rating than the propeller.

6.4 Flow Characteristics

A comparison of the mixing performance of the pitched blade turbine and marine propeller in yield stress fluids was conducted by studying the cavern size and flow patterns predicted by CFD to see if the conclusions reached in the previous section can be arrived at by studying the flow characteristics.

6.4.1 Cavern Size

As mentioned in Introduction section, the mixing of yield stress fluids with a rotating impeller results in the formation of a zone of intense motion called a cavern surrounded by stagnant fluid. The dimensions of the cavern were obtained from velocity contour plots generated from the CFD software (see Figures 6.10a-b and 6.11a-b) by specifying the cavern boundary as the position at which the velocity was reduced to one percent of the impeller tip speed, v_{ts} :

$$v_{ts} = \pi ND \tag{6.4}$$

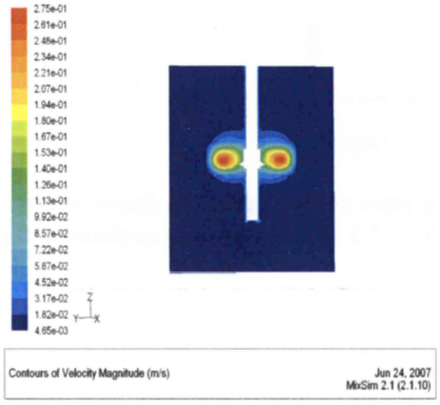

50 rpm

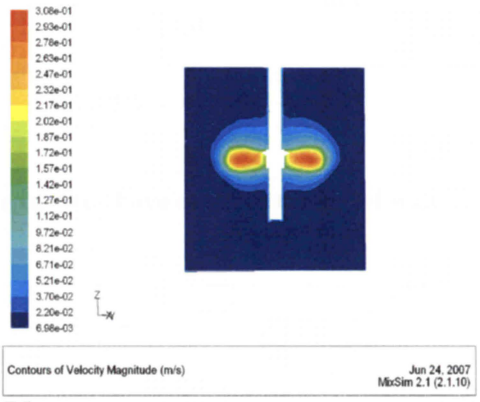

75rpm

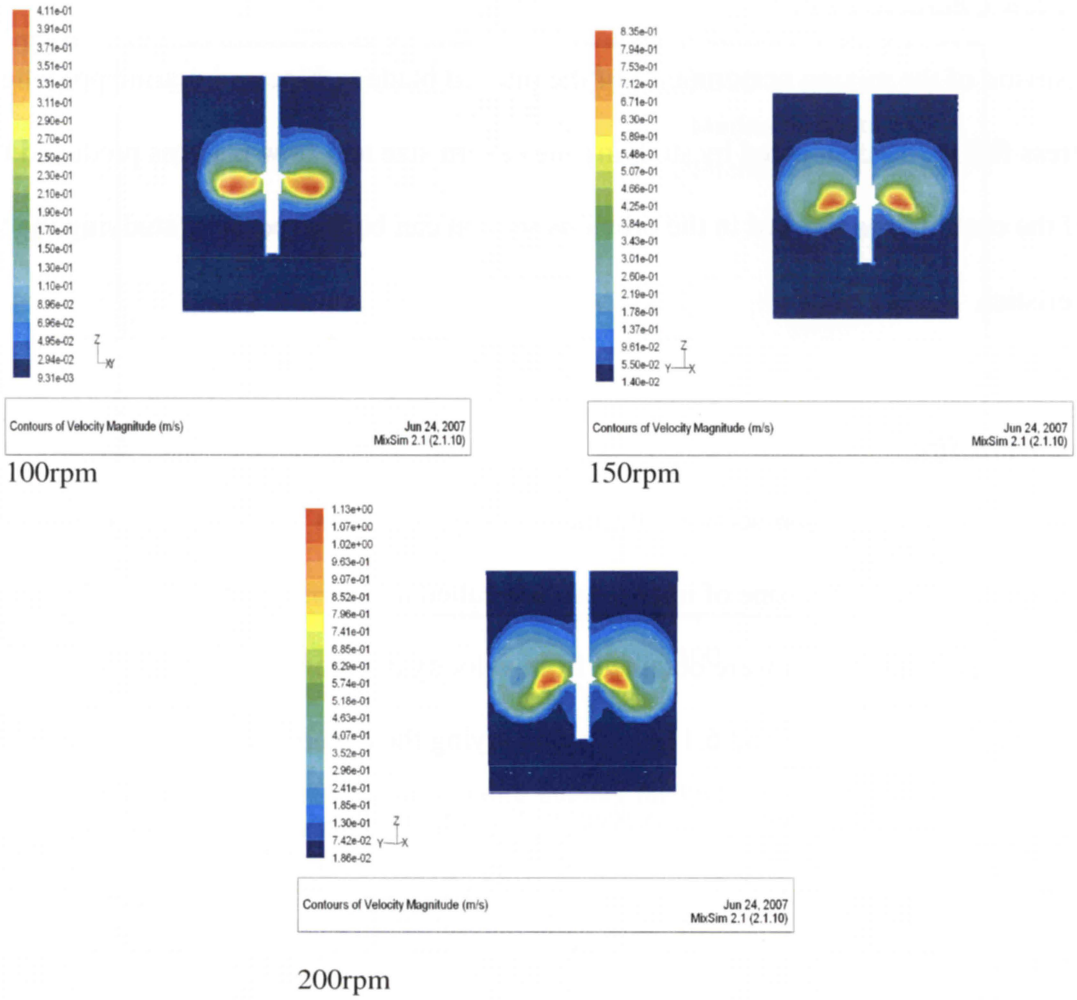

Figure 6.10a: Contours of well mixing caverns (before they reach the vessel wall) generated by PBT mixing 1.0% xanthan gum solution at C3 = 20cm

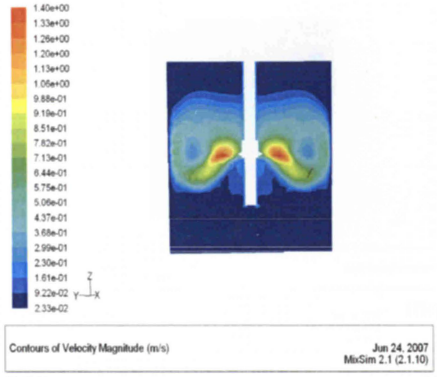

250rpm

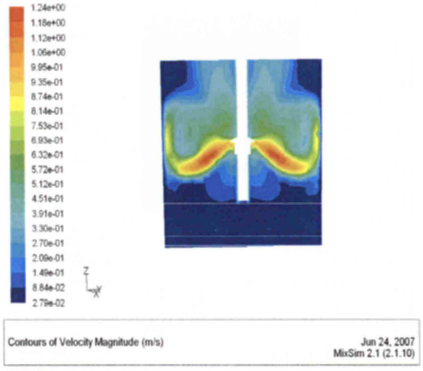

300rpm

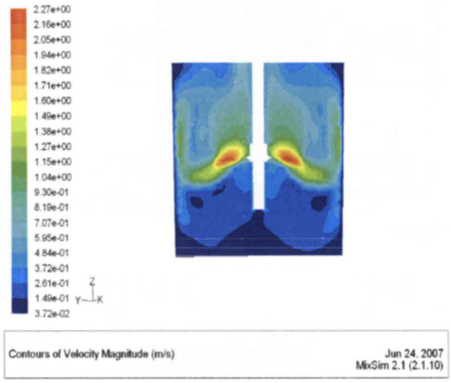

400rpm

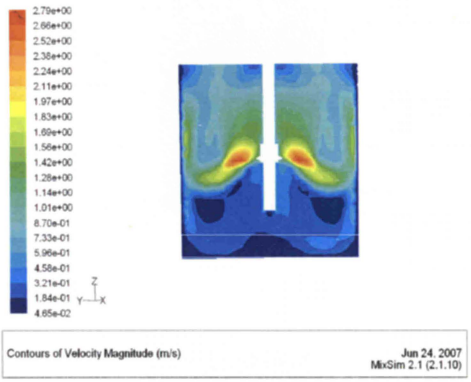

500rpm

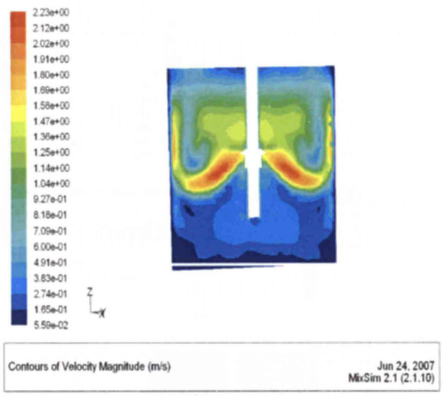

600rpm

Figure 6.10b: Growth of cavern height with speed (after the caverns have reached the vessel wall) for PBT mixing 1.0% xanthan gum solution at C3 = 20cm

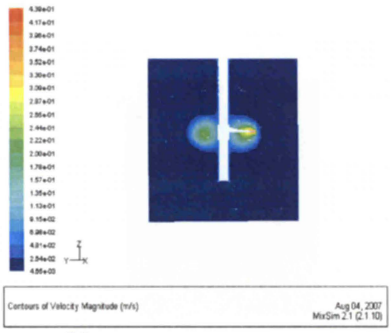

50rpm

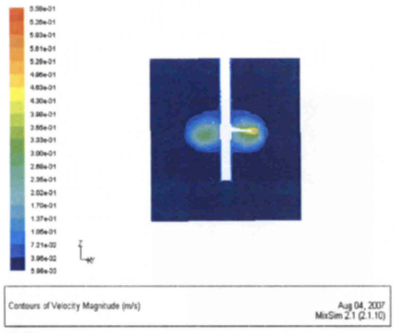

75rpm

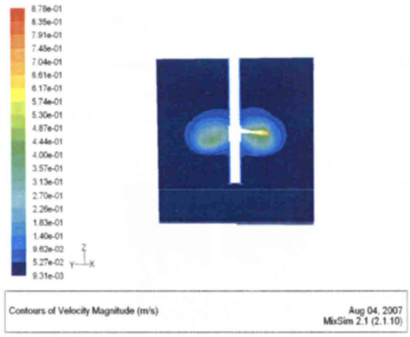

100rpm

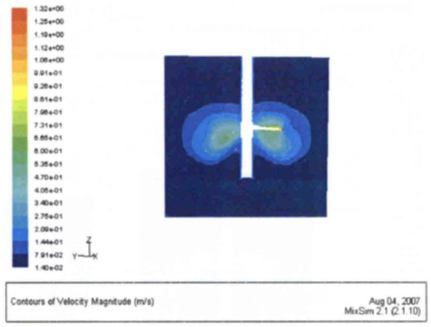

150rpm

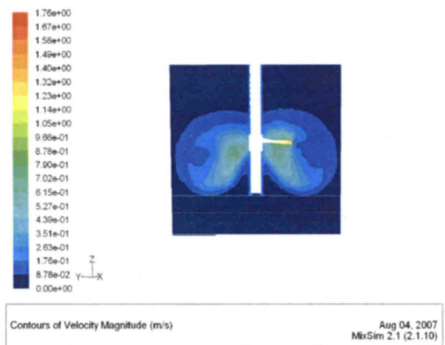

200rpm

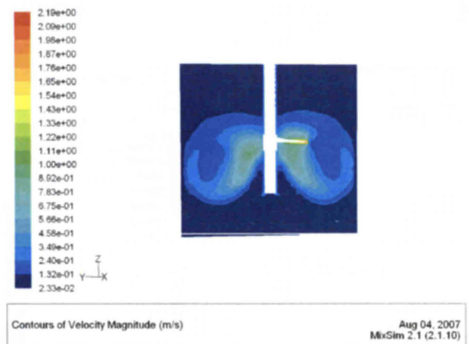

250rpm

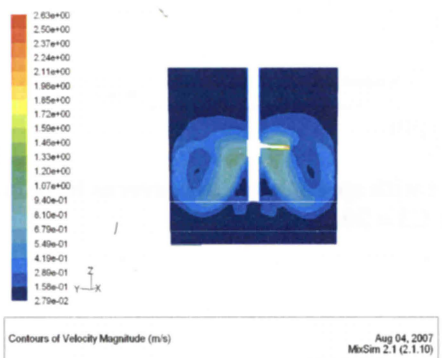

300rpm

Figure 6.11a: Contours of well mixing cavern (before the reach the vessel wall) generated by Marine Propeller mixing 1.0% xanthan gum at C3 = 20cm

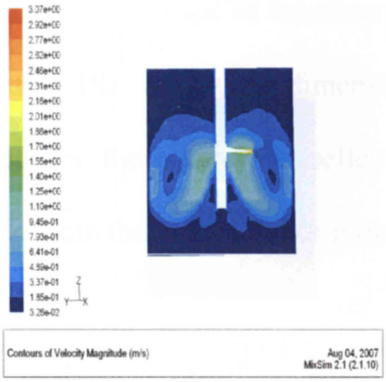

350rpm

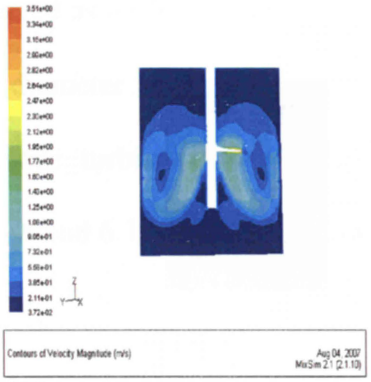

400rpm

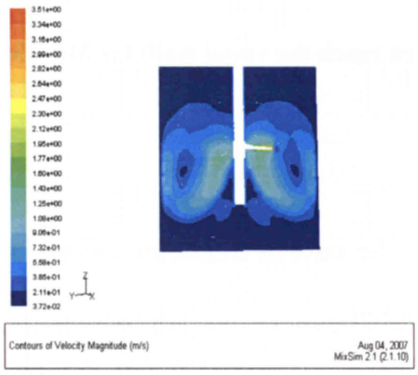

450rpm

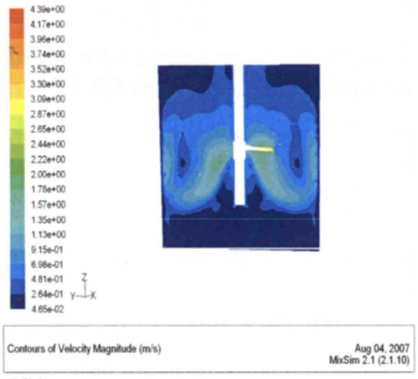

500rpm

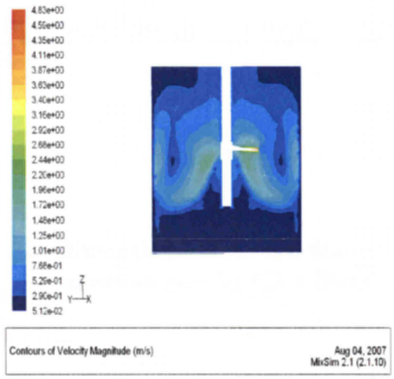

550rpm

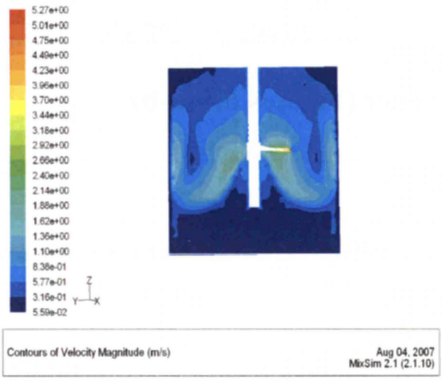

600rpm

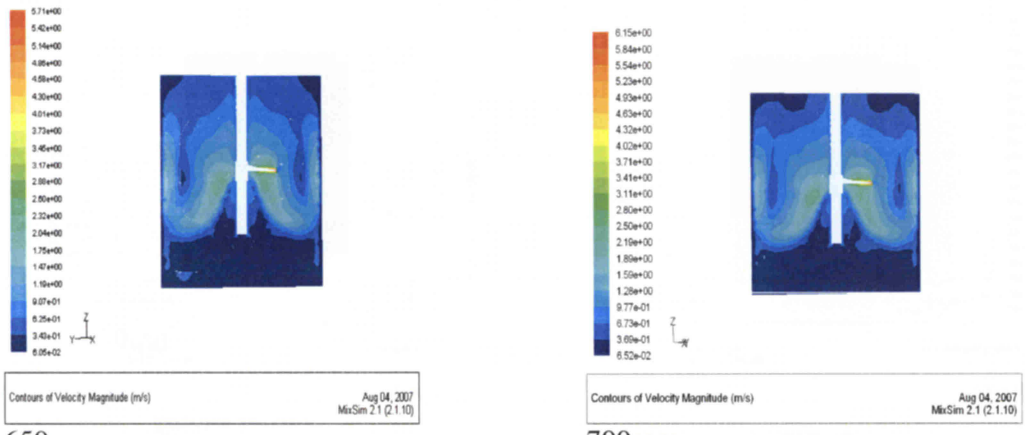

650 rpm 700rpm

Figure 6.11b: Growth of cavern height with speed (after the cavern reach the vessel wall) for Marine Propeller mixing 1.0% xanthan gum at C3 = 20cm

Figure 6.10a shows that as the impeller speed increased, the cavern diameter increases as well until the vessel wall is reached. If the speed is increased beyond that for which the cavern diameter becomes equal to the tank diameter, the height of the cavern grows with increasing impeller rotational speed, as depicted in Figure 6.10b. Similar results can be observed for the marine propeller (Figures 6.11a-b)

Assuming that the shape of the cavern could be modeled as a right circular cylinder according to Equation (2.18), a plot of dimensionless cavern diameter versus dimensionless stress was generated for the marine propeller and pitched blade turbine using the cavern dimensions measured from the CFD contour plots (Figures 6.10a-b and 6.11a-b) and is shown below:

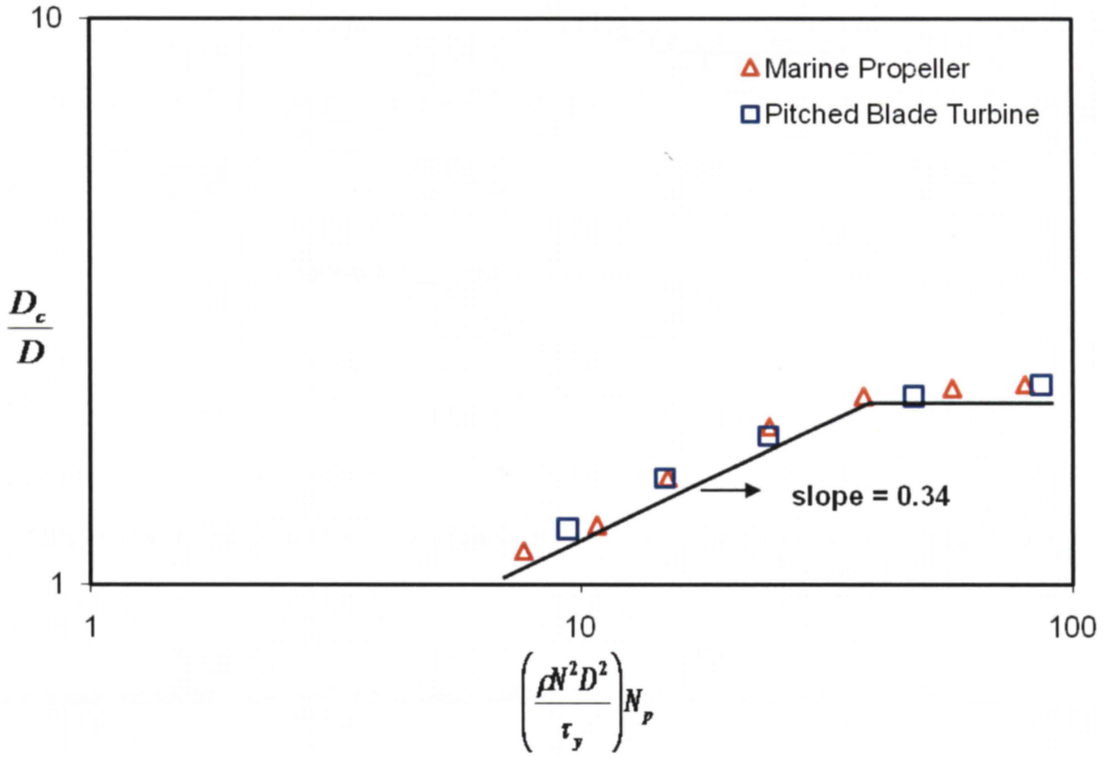

Figure 6.12: Dimensionless cavern diameter vs. dimensionless stress for the Marine Propeller and PBT mixing 1.0% xanthan gum at C3 = 20cm

As may be observed from Figure 6.12, the data for both the pitched blade turbine and the marine propeller can be approximately fit with a straight line of slope 0.34, which is very close to the value of $\frac{1}{3}$ predicted by equation (2.18). Therefore, the assumption of a right circular cylinder as the shape of the cavern seems to be a viable one for both impeller types.

Once the cavern has grown up to the vessel wall, its diameter is constant and equal to tank diameter. Therefore, the growth of the cavern height with impeller rotational speed was determined according to Equation (2.19) and is represented in Figure 6.13.

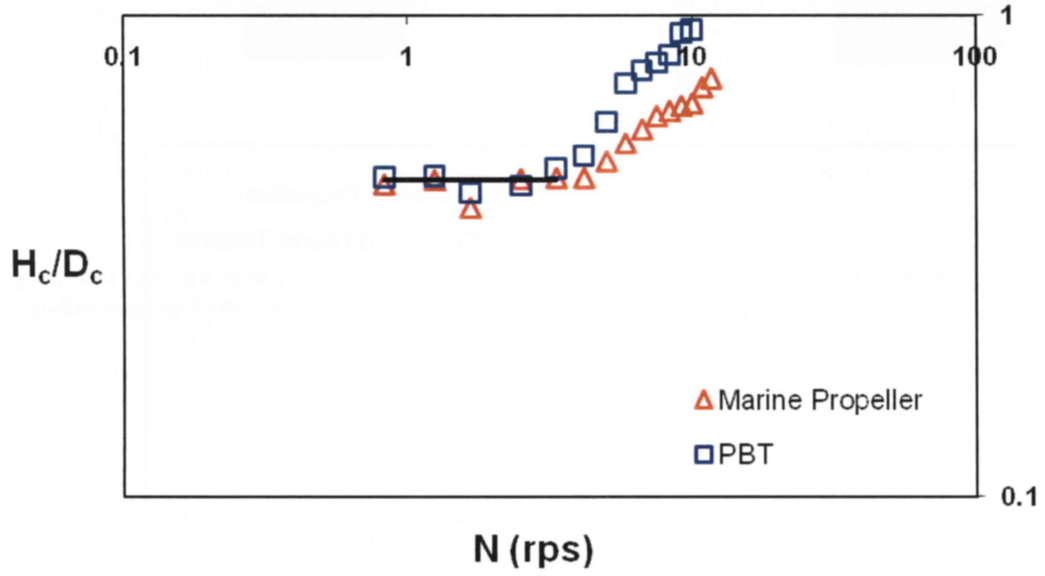

Figure 6.13: Cavern height to diameter ratio vs. Impeller rotational speed for Marine Propeller and PBT mixing 1.0% xanthan gum solution at C3 = 20cm

According to Figure 6.13, before the cavern reaches the wall, the ratio $\frac{H_c}{D_c}$ is an average value of 0.48 for both impeller types, which is within the range of the value of 0.55 ± 0.10 predicted by Elson (1998) and Solomon *et al.* (1981) for the pitched blade turbine but considerably less than the value of 0.75 ± 0.05 predicted by Elson (1990) for the marine propeller, which may be due to differences between the rheological properties of the fluid used in this work and that reported in the literature.

From Figure 6.13, it can also be seen that the growth of the well mixed region with impeller rotational speed is greater for the pitched blade turbine than with the marine propeller, which

could also be an indication of the mixing performance of these impellers. The exponent p was calculated as 0.67 and 0.54 for the pitched blade turbine and marine propeller respectively. Values of p ranging from 0.76 for marine propellers to 0.88 for Rushton turbines have been reported (Elson, 1990b). The p value of 0.54 obtained for the marine propeller is exactly the same value obtained by Galindo and Nienow (1993) for the Scaba 6SRGT impeller.

In addition, using the expression for cavern volume ($V_c = \pi(D_c/2)^2 H_c$), the marine propeller and the pitched blade turbine were compared to determine which of them gave the larger cavern volume per unit of power input, which is another indication of mixing performance.

According to Figure 6.16, at a power input greater than 50W, the pitched blade turbine generates larger caverns for a given power input. Below 50W, both impellers gave approximately the same cavern volume per unit of power input. Since the mixing performance of both impellers have mainly been investigated at power input levels greater than 50W, the pitched blade turbine may be considered to give larger caverns per unit of power input, and is therefore more desirable than the marine propeller for the homogenization of yield stress fluids.

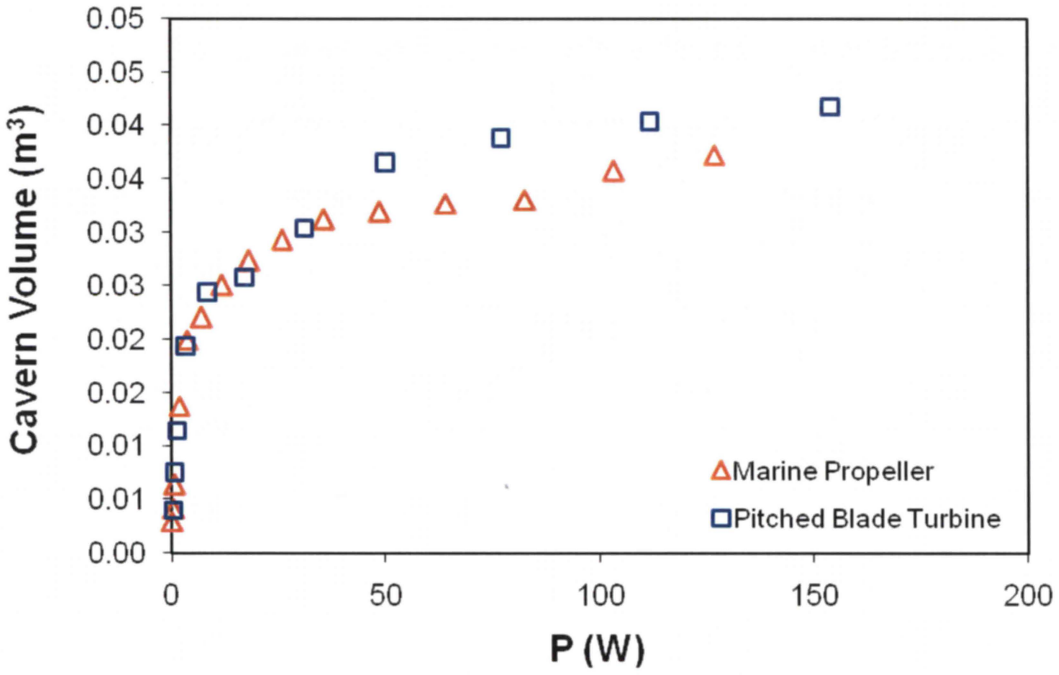

Figure 6.14: Comparison of the Cavern volume per unit Power Input for the Marine Propeller and PBT mixing 1.0% xanthan gum at C3 = 20cm

6.4.2 Flow Pattern

One of the advantages of the CFD tool is that it allows for the visualization of the flow patterns generated by each of the impellers for a given set of conditions. Figures 6.15 and 6.16 show the velocity vectors generated by the PBT and marine propeller in mixing 1% xanthan gum solution at C3 = 20cm:

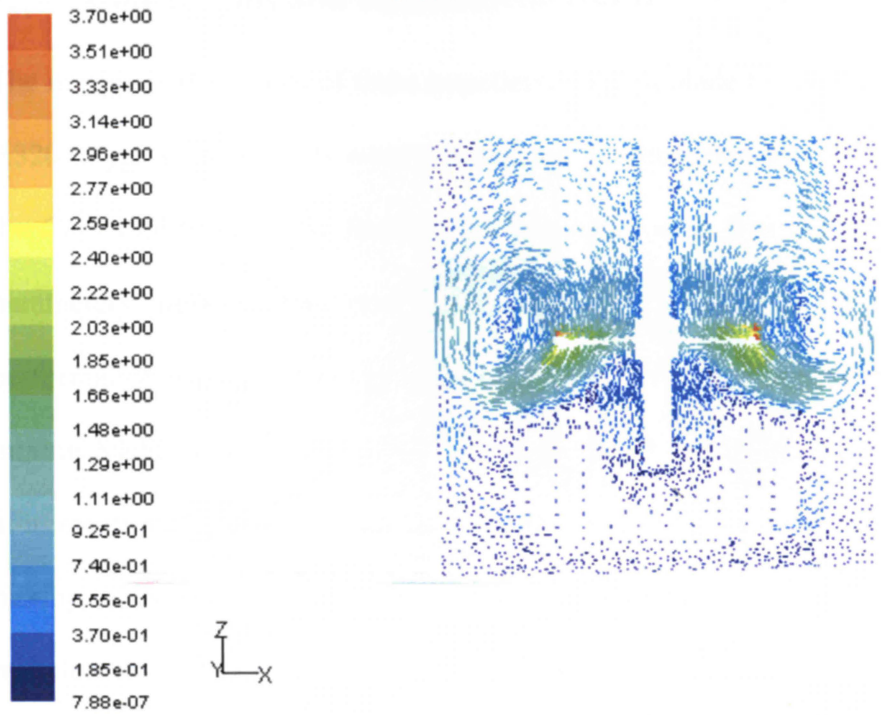

Figure 6.15: Velocity vectors generated by the PBT mixing 1.0% xanthan gum at C3 = 20cm

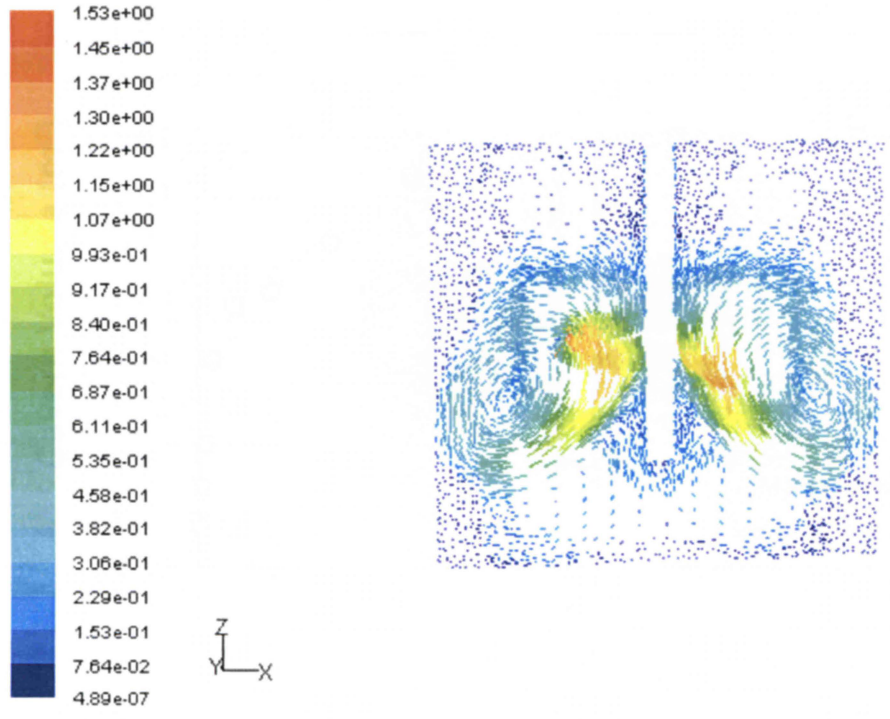

Figure 6.16: Velocity vectors generated by the Marine Propeller mixing 1.0% xanthan gum at C3 = 20cm

These figures show that both impellers pump the fluid downwards causing the fluid to flow towards the vessel bottom. On encountering the vessel bottom, the fluid flows back upwards along the shaft.

7. Conclusions and Recommendations

The mixing performance of three impellers: pitched blade turbine, marine propeller and Lightnin A320 in yield stress fluids were investigated. Experiments were conducted and the capability of the CFD tool to correctly forecast the mixing process was examined. The effects of different parameters: impeller rotational speed, impeller clearance and fluid rheology on the mixing performance was also studied in an attempt to evolve an optimum mixing system design for mixing yield stress fluids. The results indicated that CFD provides realistic trends of the aforementioned parameters on the mixing time. However, it was observed that the numerical mixing times were still deviant from the experimental mixing times. A thorough literature search revealed that CFD codes may not be adequately predicting the mass exchange between the circulation loops in the mixing tank. For axial flow impellers such as the pitched blade turbine, mixing a high viscosity fluid transforms the flow pattern from being generated as a single stage to the formation of two circulation loops on either side of the impeller shaft. Since adequate mixing time predictions are based on the correct simulation of the mass exchange between the circulation loops in the mixing tank the CFD codes cannot give accurate mixing time predictions if they do not satisfy this requirement.

In order to determine the impeller design best suited for the mixing of yield stress fluids, the mixing time number was plotted over the flow regime, and impeller efficiency studies were conducted using the performance rating. Furthermore, in the case of the marine propeller and pitched blade turbine, the characteristics of the flow and caverns generated by these impellers were studied since the impeller that is able to put majority of fluid in motion is desirable. Based

on these studies, it was found that of the three impellers, the pitched blade turbine was most superior in mixing performance.

Recommendations for future work include increasing the number of probes used for mixing time measurements in the experimental work, so that all portions of the tank are taken into account in measuring the mixing time.

Nomenclature

a_{nb} linearized coefficient for ϕ_{nb} in Equation (3.9)

a_p linearized coefficient for ϕ_p in Equation (3.9)

b linearized source term in Equation (3.9)

C impeller clearance (distance from vessel bottom to midpoint of the impeller), m

D impeller diameter, m

D diffusion conductance at the cell face

D_c cavern diameter, m

e east control volume face

e constant in Equation (2.16)

F convective mass flux per unit area at the cell face

K consistency index, $Pa.s^n$

H fluid height, m

H_c cavern height, m

k_s proportionality constant, dimensionless

K_p geometric constant, dimensionless

k_m mixing time number, dimensionless

m_l mass fraction of tracer species, dimensionless

n flow behavior index, dimensionless

nb neighboring nodes

N impeller rotational speed, s^{-1}

N_p Power Number, dimensionless

N_Q Flow Number, dimensionless

M_c Corrected Torque, Nm

M_m Measured Torque, Nm

M_r Residual Torque, Nm

p Exponent in Equation (2.18)

P Power Consumption, W

P_e Peclet Number, dimensionless

$Q_{impeller}$ Impeller pumping capacity, m^3/s

Re Reynolds number (Newtonian fluids), dimensionless

Re_a Apparent Reynolds number (non-Newtonian fluids), dimensionless

S_{Mx} x-momentum source in Equation (3.2a)

S_{My} y-momentum source in Equation (3.2b)

S_{Mz} z-momentum source in Equation (3.2c)

T Tank diameter, m

t_m mixing time, s

t_c circulation time, s

V_c volume of well mixed cavern, m^3

w west control volume face

w baffle width, m

Greek Symbols

ρ fluid density, kg/m^3

μ viscosity (Newtonian fluids), Pa.s

μ_a apparent viscosity (non-Newtonian fluids), Pa.s

μ_0 yielding viscosity, Pa.s

τ shear stress, Pa

τ_y yield stress, Pa

$\dot{\gamma}$ shear rate, s^{-1}

$\dot{\gamma}_{av}$ average shear rate, s^{-1}

ϕ general dependent variable introduced in Equation (3.3)

Γ_l molecular diffusivity, m^2/s

Abbreviations

CFD	Computational Fluid Dynamics
MRF	Multiple Reference Frame
PBT	Pitched Blade Turbine
PISO	Pressure Implicit with Splitting of Operators
RMS	Root Mean Square
SIMPLE	Semi-Implicit Method for Pressure-Linked Equations
SIMPLER	SIMPLE-Revised
SIMPLEC	SIMPLE-Consistent

Bibliography

Aubin, J.; Fletcher, D.F. and Xuereb, C. "Modeling turbulent flow in stirred tanks with CFD: the influence of the modeling approach, turbulence model and numerical scheme"; Expt. Thermal Fluid Sci. **2004**, 28 (pp.431-445)

Abid, M.; Xuereb, C.; Bertrand, J. "Modeling of the 3D hydrodynamics of 2-blade impellers in stirred tanks filled with a highly viscous fluid"; Can. J. Chem. Eng. **1994**, 72 (pp. 184-193)

Ascanio, G.; Foucault, S.; Tanguy, P.A. "New Chaotic Approach For Mixing Shear-thinning Fluids in Stirred Tanks"; 4th ASME_JSME Joint Fluids Engineering Conference **2003**, 1 (pp.1231-1236)

Amanullah, A.; Serrano-Carreon, L.; Castro, B.; Galindo, E.; Nienow, A.W. "The Influence of Impeller Type in Pilot Scale Xanthan Fermentations"; Biotech Bioeng **1998**, 57 (pp. 95-108)

Bertrand, F.; Tanguy, P.A.; Brito – De La Fuente, E. "New perspective for the mixing of yield stress fluids with anchor impellers"; J. Chem. Eng. Japan **1996**, 29 (pp. 51-58)

Brucato, A.; Ciofalo, M.; Grisafi, F.; Micale, G. "Numerical prediction of flow fields in baffled stirred vessels: A comparison of alternative modeling approaches"; Chem. Eng. Sci. **1998,** 53 (pp.3653-3684)

Bujalski, J.M.; Jaworski, Z.; Bujalski, W.; Nienow, A.W. "The Influence of the Addition Positon of a Tracer on CFD Simulated Mixing Times in a Vessel Agitated by a Rushton Turbine"; Trans IChem E. **2002**, 80, Part A (pp. 824-831)

Bujalski, W.; Jaworski, Z.; Nienow, A.W. "CFD Study of Homogenization with dual Rushton Turbines – Comparison with Experimental Results Part II: The Multiple Reference Frame"; Trans IChem E **2002**, 80, Part A (pp. 97-104)

Calderbank , P.H.; Moo-Young, M.B. "The Prediction of Power Consumption in the agitation of non-Newtonian Fluids"; Trans. IC hem E. **1959**, 37 (pp. 26-33)

Carreau, P.J.; Patterson, I.; Yap, C.Y. "Mixing of viscoelastic fluids with helical ribbon agitators. I- Mixing time and flow patterns"; Can. J. Chem. Eng. **1976**, 54 (pp. 135-)

Casas, J.A.; Santos, V.E. and Garcia-Ochoa, F. "Xanthan gum production under several operational conditions: molecular structure and rheological properties"; Enzy. Microb. Technol. **2000**, 26 (pp. 282-291)

Cebeci, T.; Shao, J.P.; Kafyeke, F.; Laurendeau, E. Computational Fluid Dynamics for Engineers; Horizons Publishing Inc.: California, 2005

Chavan,V.V.; Ford, D.E.; Arumugam, M. "Influence of Fluid Rheology on Circulation, Mixing and Blending"; Can. J. Chem. Eng. **1975**, 53 (pp. 628-635)

Cheng, J.; Carreau, P.J. "Mixing in the Transition Flow Regime with Helical Ribbon Agitators"; Can. J. Chem. Eng. **1994**, 72 (pp. 418-429)

Chhabra, R.P., Richardson, J.F. Non-Newtonian Flow in the Process Industries; Butterworth-Heinemann: Boston, **1999**

Curran, S.J.; Hayes, R.E.; Afacan, A.; Williams, M.C. "Experimental Mixing Study of a Yield Stress Fluid in a Laminar Stirred Tank"; Ind. Eng. Chem. Res. **2000**, 39 (pp. 195-202)

Deglon, D.A.; Meyer, C.J. "CFD modeling of stirred tanks: Numerical considerations"; Min Eng. **2006**, 19, (pp.1059-1068)

Delaplace, G.; Leuliet, J.C.; Relandeau, V. "Circulation and mixing times for helical ribbon impellers. Review and Experiments"; Experiments in Fluids. Experiments in Fluids **2000a,** 28 (pp. 170-182)

Delaplace, G.; Leuliet, J-C.; Ronse, G. "Power Requirement when Mixing a Shear-Thickening Fluid with a Helical Ribbon Impeller Type"; Chem. Eng. Technol. **2000b**, 23 (pp. 329-336)

De la Villeon, J.; Bertrand, F.; Tanguy, P.A.; Labrie, R.; Bousquet, J. and Lebouvier, D. "Numerical Investigation of Mixing Efficiency of Helical Ribbons" AIChE J., 1998, 44 (pp.972-977)

Dickey, D.S. "AIChE Equipment Testing Procedures: Mixing Equipment (Impeller Type)" AIChE: New York, 2001

Elson, T.P.; Cheesman, D.J. and Nienow, A.W. "X-Ray Studies of Cavern Sizes and Mixing Performance with Fluids Possessing a Yield Stress"; Chem. Eng. Sci., **1986**, 41 (pp. 2555-2562)

Elson, T.P. "X-Ray Flow Visualization of Flow Patterns during the Mixing of Yield Stress, Newtonian and Dilatant Fluids"; Chem. Eng. Comm., **1990a**, 94 (pp.142-158)

Elson, T.P. "The growth of caverns formed around rotating impellers during the mixing of a yield stress fluid"; Chem. Eng. Commun., **1990b**, 96 (pp. 303-319)

Espinosa-Solares, T.; Brito-De La Fuente, E.; Tecante, A.; Tanguy, P.A. "Power consumption of a dual turbine-helical ribbon impeller mixer in ungassed conditions"; Chem. Eng. Sci., **1997**, 67 (pp. 215-219)

FLUENT Inc., Fluent 6.3 User's Guide Documentation. FLUENT Inc. **2006**

Ford, C. CFD Simulation of Mixing Dynamics in Agitated Pulp Stock Chests. M.A.Sc Thesis, University of British Columbia, Canada, **2004**

Ford, D.E.; Mashelkar, R.A.; Ulbrecht, J. "Mixing Times in Newtonian and non-Newtonian fluids"; Process Technology International, **1972**, 17 (pp. 803-807)

Funahashi, H.; Harada, H.; Taguchi, H. and Yoshida, T. "Circulation time distribution and volume of mixing regions in highly viscous Xanthan gum solution in a stirred tank"; J. Chem. Eng. Japan, **1987**, 3 (pp. 277-281)

Galindo, E.; Nienow, A.W. "Mixing of highly viscous simulated Xanthan fermentation broths with the Lightnin A-315 Impeller"; Biotechnol. Prog., **1992**, 8 (pp. 233-239)

Galindo, E.; Nienow, A.W. "Performance of the Scaba 6SRGT Agitator in Mixing of Simulated Xanthan Gum Broths"; Chem. Eng. Techonol., **1993**, 16 (pp. 102-108)

Galindo, E.; Arguello, M.A.; Velasco, D.; Albiter,V. and Martinez, A. "A Comparison of Cavern Development in Mixing a Yield Stress Fluid by Rushton and Intermig Impellers"; Chem. Eng. Technol. **1996**, 19 (pp. 315-323)

Garcia-Ochoa, F. and Casas, J.A. "Apparent yield stress in xanthan gum solutions at low concentrations"; J. Chem. Eng., **1994**, 53 (pp. B41-B46)

Hannote, M.; Flores, F.; Torres, L. and Galindo, E. "Apparent yield stress estimation in xanthan gum solutions and fermentation broths using a low-cost viscometer"; The Chem. Eng. J., **1991**, 45 (pp. B49 – B56)

Harnby, N.; Edwards, M.F.; Nienow, A.W. Mixing in the Process Industries; Butterworth-Heinemann: Boston, **1997**.

Harvey, A. D.; Cassian, K.L. "Steady-state Modelling and Experimental Measurement of a Baffled Impeller Stirred Tank"; AIChE J, **1995**, 41 (pp. 2177-2186)

Hayes, R.E.; Afacan, A.; Boulanger, B.; Tanguy, P.A. "Experimental study of reactive mixing in a laminar flow batch reactor"; Trans IChemE, Part A **1998**, 76 (pp. 73 -81)

Hiby, J.W. "Definition and measurement of the degree of mixing in liquid mixtures"; Int. Chem. Eng, **1981**, 21 (pp. 197-204)

Hirata, Y.; Aoshima, Y. "Formation and Growth of Cavern in Yield Stress Fluids Agitated Under Baffled and Non-Baffled Conditions"; Trans IChemE, **1996**, 74 (pp. 438-444)

Holland, F.A. and Chapman, F.S. Liquid Mixing and Processing in Stirred Tanks; Reinhold Publishing Corporation: New York, **1966**

Houcine, I.; Plasari, E.; David, R. "Effects of the stirred tank's design on power consumption and mixing time in liquid phase"; Chem. Eng. Technol., **2000**, 23 (pp.605-613)

Javed, K.H.; Mahmud, T.; Zhu, J.M. "Numerical simulation of turbulent batch mixing in a vessel agitated by a Rushton turbine"; Chemical Engineering and Processing, **2006**, 45 (pp. 99-112)

Jaworkski, Z. and Dudczak, J. "CFD modeling of turbulent macromixing in stirred tanks. Effect of the probe size and number on mixing indices"; Computers Chem. Eng., **1998**, 22 (pp. S293-S298)

Jaworski, Z.; Bujalski, W.; Otomo, N. and Nienow, A.W. "CFD Study of Homogenization with Dual Rushton Turbines – Comparison with Experimental Results"; Trans IChemE, **2000**, 78, (pp.327-333)

Katzbauer, B. "Properties and applications of xanthan gum"; Polymer Degradation and Stability, **1998**, 59 (pp.81-84)

Kelly, W. and Gigas, B. "Using CFD to predict the behavior of power law fluids near axial-flow impellers operating in the transitional flow regime"; Chem. Eng. Sci., **2003**, 58 (pp.2141-2152)

Kim, S.; Nkaya, A.N.; Dyakowski, T. "Measurement of mixing of two miscible liquids in a stirred vessel with electrical resistance tomography"; Int. Commun. Heat and Mass Transfer, **2006**, 33 (pp.1088-1095)

Lee, K.C.; Yianneskis, M. "A Liquid Crystal Thermographic Technique for the Measurement of Mixing Characteristics in Stirred Vessels"; Trans IChemE, **1997**, 75, Part A (pp. 746-754)

Luo, J.Y.; Gosman, A.D.; Issa, R.I.; Middleton, J.C.; Fitzgerald, M.K. "Full Flow Field Computation of Mixing in Baffled Stirred Vessels"; Trans IChemE., **1993,** 71, Part A (pp.342-344)

Mavros, P. "Flow Visualization in Stirred Vessels: A Review of Experimental Techniques"; Trans IChemE, **2001**, 79, Part A (pp.113-127)

Menisher, T.; Metghalchi, M.; Gutoff, E.B. "Mixing Studies in Bioreactors"; Bioprocess Engineering, **2000**, 22 (pp. 115-120)

Metzner, A.B.; Otto, R.E. "Agitation of Non-Newtonian Fluids"; AIChE J., **1957**, 3 (pp. 3-)

Metzner, A.B.; Feehs, R.H.; Ramos, H.L.; Otto, R.E. and Tuthill, J.D. "Agitation of viscous Newtonian and non-Newtonian fluids"; AIChE J., **1961**, 7 (pp. 3-9)

Montante, G.; Lee, K.C.; Brucato, A.; Yianneskis, M. "Numerial simulations of the dependency of flow pattern on impeller clearance in stirred vessels"; Chem. Eng. Sci., **2001**, 56 (pp. 3751-3770)

Montante, G; Magelli, F. "Liquid Homogenization characteristics in vessels stirred with multiple Rushton Turbines mounted at different spacing. CFD study and comparison with Experimental data"; Trans IChemE, Part A, Chemical Engineering Research and Design, **2004**, 82 (pp. 1179-1187)

Montante, G.; Mostek, M.; Jahoda, M.; Magelli, F. "CFD simulations and experimental validation of homogenization curves and mixing time in stirred Newtonian and pseudoplastic liquids"; Chem. Eng. Sci., **2005**, 60 (pp. 2427-2437)

Moore, I.P.T.; Cossor, G.; Baker, M.R. "Velocity Distributions in a Stirred Tank Containing a Yield Stress Fluid"; Chem. Eng. Sci., **1995**, 50 (pp.2467-2481)

Moo-Young, M.; Tichar, K.; Dullien, F.A.L. "The Blending Efficiencies of Some Impellers in Batch Mixing"; AIChE J., **1972**, 18 (pp. 178-182)

Nere, N.K.; Patwardhan, A.W.; Joshi, J.B. "Liquid-phase mixing in stirred vessels: turbulent flow regime" Ind. Eng. Chem. Res., **2003**, 42 (pp. 2661-2698)

Nienow, A.W.; Elson, T.P. "Aspects of Mixing in Rheologically Complex Fluids"; Chem. Eng. Res. Des., **1988**, 66 (pp. 5-15)

Novak, V., and Rieger, F. "Homogenization efficiency of helical ribbon and anchor agitators." ; J. Chem. Eng., **1975,** 9 (pp. 63-70)

Oldshue, J.Y. Fluid Mixing Technology; McGraw-Hill Book Company: New York, **1983**.

Oshinowo, L.; Bakker, A. and Marshall, E. "Computational Fluid Dynamics: Simulating Mixing Time"; Chem. Eng. World, **2002** (pp. 75-77)

Osman, J.J. and Varley, J. "The Use of Computational Fluid Dynamics (CFD) to Estimate Mixing Times in a Stirred Tank"; IChemE Symp. Series, **1999** (pp. 15-22)

Pant, H.J. "Radiotracer Applications in Chemical Process Industry"; Reviews in Chemical Engineering, **2001**, 17 (pp.165-252)

Patankar, S.V. Numerical Heat Transfer and Fluid Flow; Hemisphere: Washington, D.C., **1980**

Paul, E.L.; Atiemo-Obeng, V.A.; Kresta, S.M. Handbook of Industrial Mixing: Science and Practice; John Wiley & Sons, Inc.: Hoboken, N.J., **2004**

Perng, C.Y.; Murthy, J.Y. "A Moving-Deforming-Mesh Technique for Simulation of Flow in Mixing Tanks"; AIChE Symposium Series, **1993**, 89 (pp.37-41)

Perse, L.S. and Zumer, M. "Mixing and Viscosity Determinations with Helical Ribbon Impeller"; Chem. Biochem. Eng. Q., **2004**, 18 (pp. 363-371)

Ranade, V.V.; Joshi, J.B.; Marathe, A.G. "Flow Generated by Pitched Blade Turbines II: Simulation using $k-\varepsilon$ Model"; Chem. Eng. Comm., **1989**, 81 (pp. 225-248)

Ranade, V.V.; Mishra, V.P.; Saraph, V.S.; Deshpande, G.B. and Joshi, J.B. "Comparison of Axial Flow Impellers Using a Laser Doppler Anemometer"; Ind. Eng. Chem. Res., **1992**, 31 (pp.2370-2379)

Ranade, V.V. and Van den Akker, H.E.A. "A computational snap-shot of gas-liquid flow in baffled stirred vessels"; Chem. Eng. Sci., **1994**, 49, (pp. 5175-5192)

Ranade, V.V. and Dommeti, S.M.S. "Computational Snapshot of Flow Generated by Axial Impellers in Baffled Stirred Vessels"; Trans IChemE, **1996**, 74 (pp.476-484)

Ranade, V.V. "An efficient computational model for simulating flow in stirred vessels: a case of Rushton turbine"; Chem. Eng. Sci., **1997**, 52 (pp.4473-4484)

Sahu, A.K.; Kumar, P.; Patwardhan, A.W.; Joshi, J.B. "CFD modeling and mixing in stirred tanks"; Chem. Eng. Sci., **1999**, 54 (pp. 2285-2293)

Shekhar, S.M. and Jayanti, S. "Mixing of Pseudoplastic Fluids Using Helical Ribbon Impellers"; AIChE J., **2003**, 49 (pp. 2768-2772)

Shiue, S.J. and Wong, C.W. "Studies on Homogenization Efficiency of Various Agitators in Liquid Blending"; Can. J. Chem. Eng. **1984**, 62 (pp. 602-609)

Solomon, J.; Elson, T.P. and Nienow, A.W. and Pace, G.W. "Cavern Sizes in Agitated Fluids with a Yield Stress"; Chem. Eng. Commun., **1981**, 11 (pp. 143-164)

Sommerfeld, M.; Decker, S. "State of the Art and Future Trends in CFD Simulation of Stirred Vessel Hydrodynamics"; Chem. Eng. Technol., **2004**, 27 (pp. 215-224)

Tatterson, G.B. Fluid Mixing and Gas Dispersion in Agitated Tanks; McGraw-Hill Inc.: Toronto, **1991**

Torrestiana, B.; Galindo, E.; Xueming, Z. and Nienow, A.W. "In-Fermenter Power Measurement during a Xanthan Gum Fermentation compared with Non-Fermentative Studies"; Trans IChemE, **1991**, 69, Part C (pp.149-155)

Thyn, J.; Novy, M.; Mostek, M.; Zitny, R. and Jahoda, M. "CFD simulation of homogenization time measured by radiotracers"; Nukleonika, **2005**, 50 (pp. 9-16)

Versteeg, H.K.; Malalasekera, W. An Introduction To Computational Fluid Dynamics. The Finite Volume Method; Longman Group Ltd., Toronto, **1995**

Wang, M.; Dorward, A.; Vlaev, D. and Mann, R. "Measurements of gas-liquid mixing in a stirred vessel using electrical resistance tomography (ERT)"; Chem. Eng. J., **2000**, 77 (pp. 93-98)

Whitcomb, P.J.; Macosko, C.W. "Rheology of Xanthan Gum"; J. Rheol., **1978**, 22 (pp. 493-505)

Yap, C.Y.; Patterson, W.I. and Carreau, P.J. "Part III. Non-Newtonian Fluids"; AIChE J., **1979**, 25 (pp.516-521)

Zhu, H.; Kim, Y.D.; De Kee, D. "Non-Newtonian fluids with a yield stress"; J. Non-Newtonian Fluid Mech., **2005**, 129 (pp. 177-181)

Wichterle, K. and Wein, O. "Threshold of mixing of non-Newtonian fluids"; Int. Chem. Eng., **1989**, 21, (pp.116-120)

Xu, Y. and McGrath, G. "CFD Predictions of Stirred Tank Flows"; Trans IChemE, **1996**, 74, Part A (pp.471-475)

APPENDIX A

Table A.1: Torque data for Pitched Blade Turbine for 0.5% Xanthan gum and C1 = 13.5cm

Impeller speed (rpm)	Torque (Nm)		
	Experiment	CFD	% Deviation
20	-	0.01238	-
25	-	0.01354	-
35	0.04124	0.01735	57.9
50	0.04844	0.02973	38.6
75	0.07920	0.05733	27.6
90	-	0.08063	-
100	0.10375	0.10002	35.9
120	-	0.14776	-
150	0.25556	0.23928	6.4
175	-	0.33744	-
200	0.45847	0.45223	1.36
225	-	0.58716	-
250	0.64334	0.73796	14.7
275	0.74046	0.89883	21.4
300	0.93462	1.07045	14.5
350	1.28257	-	-
400	1.67826	-	-
450	2.10811	-	-

Table A.2: Torque data for Pitched Blade Turbine for 1.0% Xanthan gum and C1 = 13.5cm

Impeller speed (rpm)	Torque (Nm)		
	Experiment	CFD	% Deviation
25	-	0.03404	-
35	-	0.03730	-
50	0.04594	0.04418	3.8
75	-	0.06975	-
90	-	0.09496	-
100	0.12447	0.11301	9.2
150	0.23312	0.22363	4.1
200	0.41071	0.40561	1.2
225	-	0.52242	-
250	0.64217	0.65626	2.5
275	-	0.81033	-
300	0.94952	0.98244	3.5
350	1.29646	1.37753	6.3
400	1.64600	1.85058	12.4
450	2.0556	2.38487	16.0
500	2.48703	2.97876	19.8
550	2.98164	3.61474	21.2
600	3.60556	3.63120	0.71

Table A.3: Torque data for Pitched Blade Turbine for 1.5% Xanthan gum and C1 = 13.5cm

Impeller speed (rpm)	Torque (Nm)		
	Experiment	CFD	% Deviation
35	-	0.06045	-
50	-	0.06675	-
75	-	0.08653	-
90	-	0.10651	-
100	-	0.12497	-
150	0.07574	0.24369	221.7
200	0.25248	0.40181	59.1
250	0.46866	0.63158	34.8
300	0.74616	0.92914	25.3
350	1.07041	1.29499	21.0
400	1.46397	1.73812	18.7
450	1.88837	2.24438	18.8
500	2.37996	2.82817	18.6
550	2.97042	3.48925	17.5
600	3.52644	4.20962	19.4

Table A.4: Torque data for Pitched Blade Turbine for 1.0% Xanthan gum and C2 = 16cm

Impeller speed (rpm)	Torque (Nm)		
	Experiment	CFD	% Deviation
50	0.09875	0.04423	55.2
75	0.14408	0.06982	51.5
100	0.18746	0.11351	39.4
125	0.22883	-	-
150	0.30315	0.22406	26.1
200	0.47359	0.40761	13.9
250	0.68776	0.66236	3.7
300	0.95604	0.98632	3.2
350	1.25860	1.37711	9.4
400	1.62165	1.83666	13.2
450	2.0025	2.33970	16.8
500	2.43154	2.92067	20.1
550	2.98778	3.66411	22.6
600	3.61263	4.42379	22.4

Table A.5: Torque data for Pitched Blade Turbine for 1.0% Xanthan gum and C3 = 20cm

Impeller speed (rpm)	Torque (Nm)		
	Experiment	CFD	% Deviation
50	0.14858	0.04423	70.2
75	0.10390	0.06996	32.7
100	0.16133	0.11369	29.5
125	0.20159	-	-
150	0.26498	0.22433	15.3
200	0.42991	0.40793	5.1
250	0.65241	0.66136	1.4
300	0.93509	0.98771	5.6
350	1.28019	1.37261	7.2
400	1.61654	1.83776	13.7
450	2.02709	2.36862	16.8
500	2.45276	2.94322	20.0
550	2.94735	3.58414	21.6
600	3.7213	3.58428	3.7

Table A.6: Torque data for Marine Propeller for 1.0% Xanthan gum and C3 = 20cm

Impeller speed (rpm)	Torque (Nm)		
	Experiment	CFD	% Deviation
50	0.15239	0.03593	76.4
75	0.13414	0.05072	62.2
100	0.06123	0.07078	15.6
125	0.07156	-	-
150	0.09689	0.11395	17.6
200	0.12078	0.17691	46.5
250	0.18609	0.26746	43.7
300	0.26001	0.37607	44.6
350	0.31297	0.49655	58.7
400	0.41293	0.62038	50.2
450	0.48717	0.75676	55.3
500	0.57122	0.92998	62.8
550	0.66643	1.11313	67.0
600	0.70812	1.31300	85.4
650	0.79505	1.51936	91.1
700	0.95442	1.72949	81.2

Table A.7: Torque data for A320 impeller for 1.0% Xanthan gum and C3 = 20cm

Impeller speed (rpm)	Torque (Nm)	
	Experiment	CFD*
50	0.13703	
75	0.13167	
100	0.14682	
120	0.19570	
150	0.26727	
200	0.38116	
250	0.57070	
300	0.827580	
350	1.03906	
400	1.28934	
450	1.57809	
500	1.92852	
550	2.31658	
600	2.77829	

*A320 impeller not available in the Mixsim impeller library

The percentage deviation of the CFD results from the experimental measurements was calculated using the expression below:

$$\%Deviation = \frac{|M_{CFD} - M_{EXP}|}{M_{EXP}} \quad \text{(A.1)}$$

APPENDIX B

Table B.1: Mixing Time data for Pitched Blade Turbine for 0.5 wt% Xanthan gum and C1= 13.5cm

	Mixing Time (s)	
Impeller Speed (rpm)	Experiment	CFD
200	-	55.00
225	-	-
250	30.42 ± 3.14	31.00
275	16.80 ± 3.65	19.18
300	10.42 ± 1.23	14.60
350	8.50 ± 2.18	-
400	8.96 ± 0.95	-
450	7.27 ± 2.53	-

Table B.2: Mixing time data for Pitched Blade Turbine for 1.0% Xanthan gum and C1 = 13.5cm

	Mixing Time (s)	
Impeller Speed (rpm)	Experiment	CFD
350	-	40.0
400	102.08 ± 6.44	28.0
450	41.25 ± 7.94	18.0
500	31.50 ± 4.92	9.3
550	10.10 ± 2.35	7.1
600	7.83 ± 1.59	4.8

Table B.3: Mixing time data for Pitched Blade Turbine for 1.5% Xanthan gum and C1 = 13.5cm

	Mixing Time (s)
Impeller Speed (rpm)	CFD
400	92.5
450	21.6
500	20.7
550	10.8
600	11.0

Table B.4: Mixing time data for Pitched Blade Turbine for 1.0% Xanthan gum and C2 = 16cm

	Mixing Time (s)	
Impeller Speed (rpm)	Experiment	CFD
400	151.08 ± 45.38	43.4
450	22.50 ± 6.61	16.6
500	7.17 ± 2.02	11.6
550	-	8.5
600	-	7.7

Table B.5: Mixing time data for Pitched Blade Turbine for 1.0% Xanthan gum and C3 = 20cm

	Mixing Time (s)	
Impeller Speed (rpm)	Experiment	CFD
350	91.03 ± 21.60	196.0
400	22.68 ± 3.76	55.0
450	20.42 ± 4.73	39.0
500	7.71 ± 1.30	12.5
550	-	9.0
600	-	8.7

Table B.6: Mixing time data for Marine Propeller for 1.0% Xanthan gum and C3 = 20cm

	Mixing Time (s)	
Impeller Speed (rpm)	Experiment	CFD
500	-	60.0
550	-	41.5
600	28.33 ± 2.89	13.2
650	18.90 ± 1.90	8.8
700	14.12 ± 2.82	6.6

Table B.7: Mixing time data for A320 impeller for 1.0% Xanthan gum and C3 = 20cm

	Mixing Time (s)	
Impeller Speed (rpm)	Experiment	CFD*
350	42.50 ± 4.33	
400	23.75 ± 3.31	
450	10.08 ± 1.81	
500	7.92 ± 1.91	
550	-	
600	-	

*A320 impeller not available in the Mixsim impeller library